University of Stuttgart
5th Institute of Physics

Vorgelegt an der Universität Stuttgart

MASTER'S THESIS

Towards High n Circular Rydberg States in Ultracold Atomic Gases

Christian Hölzl

Supervisor: Dr. Florian Meinert
Examiner: Prof. Dr. Tilman Pfau
2nd Examiner: Prof. Dr. Martin Dressel

22. October 2019

Ehrenwörtliche Erklärung

Ich erkläre hiermit, dass ich die vorliegende Arbeit selbständig verfasst und nur unter Verwendung der angegebenen Quellen und Hilfsmittel angefertigt habe. Alle wörtlich und sinngemäß aus anderen Werken übernommene Aussagen sind als solche gekennzeichnet. Die vorliegende Arbeit war weder vollständig noch in Teilenn Gegenstand eines anderen Prüfungsverfahrens. Weiterhin stimmt das elektronische Exemplar mit der gedruckten Version überein.

Stuttgart, den 22. Oktober 2019

Christian Hölzl

Abstract

Circular Rydberg states are of increased interest for quantum simulation due to their long life times. In this thesis, the creation of circular Rydberg states in an ultracold atomic environment via an adiabatic rapid passage (ARP) circularization scheme is studied and preparatory measurements and calculations are carried out. A method to generate an electric radio frequency field, necessary for the circularization is implemented and characterized. Further, measurements were conducted to characterize the Rydberg F state which serves as an initial state for the ARP protocol. We find by applying state selective field ionization that the reliable preparation of Rydberg F states is strongly affected by the density of the atomic sample and misalignment of magnetic and electric field. Experimental evidence was found that the ARP is applicable to create circular Rydberg states at $n = 56$ in our setup. To study the ARP theoretically, a simulation was developed. We find that possible σ^- polarization components of the used radio frequency field greatly reduce the fidelity of method.

Contents

Zusammenfassung

In den vergangenen Jahren haben sich Rydbergatome zu einer vielversprechenden Plattform für Quantensimulationen entwickelt. Rydbergsysteme weisen eine hohe Skalierbarkeit vor allem für zwei und drei dimensionale Probleme auf. Jedoch ist die Kohärenzzeit der für durch Laseranregung zugänglichen Rydbergzustände deutlich geringer als in Systemen aus eingefangenen Ionen.

Der Einsatz von Rydbergzuständen mit hohem Bahndrehimpuls und besonders von Zuständen mit maximalem Bahndrehimpuls, den zirkularen Zuständen, ist ein aussichtsreiches Konzept um diese Einschränkung zu überwinden. Zirkulare Zustände haben die zum klassischen Bohrmodell ähnlichsten Elektronenwellenfunktionen und weisen durch ihre geringe Anzahl an Zerfallskanälen extrem lange Lebensdauern auf. Durch ihr großes magnetisches Moment sind sie außerdem interessant für hoch empfindliche Messungen von Magnetfeldern.

Zur Erzeugung dieser Zustände muss eine große Zahl an Drehimpulsquanten auf das Atom übertragen werden, was die direkte Anregung durch Laser erschwert, da jedes Photon nur ein Drehimpulsquant trägt. In den letzten Jahrzehnten wurden mehrere Methoden auf Basis von schnellen adiabatischen Transferen vorgeschlagen und mit hoher Güte experimentell umgesetzt. Der schnelle adiabatische Transfer, bei dem ein Zustand mit niedrigem Bahndrehimpuls durch ein Radiofrequenzfeld in den zirkularen Zustand adiabatisch überführt wird stellte sich als besonders robuste Methode heraus.

In dieser Arbeit wurde die Anwendung dieser Methode in einem ultrakalten Atomexperiment untersucht und vorbereitende Messungen und Rechnungen wurden durchgeführt. Zuerst wurde gezeigt, dass es an unserem Experiment möglich ist, ein Radiofrequenzfeld mit bis zu 200 MHz an der Position der Atome effizient zu erzeugen. Des weiteren wurde die Erzeugung eines Rydberg F Zustands, welcher als Anfangszustand für die Zirkularisierung dient, mithilfe von zustandsselektiver Feldionisation untersucht. Wir stellten fest, dass die hohe Dichte der Atomwolke und ein endlicher Winkel zwischen Magnet- und elektrischem Feld das Ionisationsverhalten und die Lebensdauer des Zustands deutlich beeinflusst.

Zur theoretischen Untersuchung des adiabatischen Transfers wurde im Rahmen dieser Arbeit eine Simulation entwickelt. Es stellte sich heraus, dass eine im Radiofrequenzfeld enthaltene σ^- Polarisation die Güte des Transfers stark senkt. Am Ende der Arbeit wurde die Messung einer experimentellen Umsetzung der Zirkularisation diskutiert. Wir fanden Evidenzen dafür, dass das Verfahren des schnellen adiabatischen Transfers an unserem experimentellen Aufbau zur Erzeugung von zirkularen Zuständen mit einer Hauptquantenzahlvon $n = 56$ erfolgreich eingesetzt werden kann.

Introduction

Rydberg atoms are highly excited atoms in a state of high principal quantum number $n \gg 10$. They are named after the late 19th century Swedish physicist `Johannes Rydberg`, who is well known for the first phenomenological description of the transition frequencies between two excited electronic states of an atom [59]. They exhibit extremely large electric dipole moments which leads to Rydberg blockade effects [43]. Since by this effect only one Rydberg atom can be excited in a given volume, this leads to an optical non-linearity on the single photon level which permits the implementation of quantum gates [75, 60] and makes Rydberg atoms an ideal candidate for quantum simulators [64, 74]. They are attractive for their high scalability compared to systems of trapped ions [35], especially for 2D and 3D systems [3]. However, while they have larger coherence times than solid-state based qubits [55], the laser accessible Rydberg states still have only relatively short life times (order of $100\,\mu$s for $n = 50$) compared to ground state systems.

The high angular momentum states and specifically circular Rydberg states (CRS), the states with the highest possible orbital momentum for a given n, are a promising candidate to overcome this limitation [48], since they have very limited decay channels to only the adjacent circular states due to dipole selection rules. These states where first termed “circular” by Hulet and Kleppner [32] as these are the states with the electron wavefunction closest to the classical, circular Bohr orbit. From the states of a given principal quantum number n, they inhibit the weakest Stark shift and the largest magnetic moment $m_l = n - 1$ making them not only interesting for their long lifetime, but also for high sensitivity magnetometry [14] and electrometry [19].

The creation of these states is not straight forward, since a large number of angular momentum quanta must be transferred to the atom and each laser photon does only carry a single one. The first experimental creation of circular Rydberg states was achieved by Hulet and Kleppner in 1983 [32] in an atomic beam of lithium atoms. Although the achieved principal quantum number of $n = 19$ was relatively low, the efficiency was close to $100\,\%$. The applied adiabatic rapid passage method which consists of the adiabatic transfer from a low-l state to the CRS by linearly ramping down the electric field while dressing the Stark states with a radio frequency field proved to be an efficient method for preparing CRS. It was successfully applied to create CRS in lithium [32, 40], potassium [9] and rubidium [49]. A variant of this method was proposed by Molander et al. [46] who use an optical excitation instead of ramping the electric field.

Another highly efficient method is based on the same adiabatic passage principal, but the Stark states are not dressed by a radio frequency field but by a magnetic field under an angle. This crossed fields method was first proposed by Delande and Gay [13] and successfully applied for principal quantum numbers ranging from $n = 20$ up to $n = 70$ with a fidelity of almost unity in hydrogen [42], lithium [29], helium [81] and rubidium [5]. Recently, the use of the ponderomotive potential of a trapping beam [7] and the use of high order Laguerre-Gauss beams [58] to dress the Stark levels in a similar way was proposed.

While very efficient, those methods are quite slow due to their requirement for adiabaticity. This also reduces the efficiency for increasing principal quantum numbers. Diabatic methods are generally more complex to realize due to the complicated energetic landscape of the involved Stark states. A very efficient and fast method was recently realized by Signoles et al. [66], based on the resonant coherent transfer between a low angular momentum state and the CRS by a radio frequency field. It was shown that through the use of quantum optimal control the fidelity of this method can be further improved [51]. A different approach to engineer high-l states, where the Rydberg electron is kicked by electric pulses with a repetition rate equal to the Keppler frequency was successfully realized for sodium with $n > 300$ [16]. However, this method creates a dispersive, Bohr-like wavepacket instead of a well defined single quantum state.

The long life time makes circular states also desirable for high precision spectroscopy [25, 54]. Another intriguing feature is the unique doughnut-shaped wavefunction, making it possible to generate a Faraday shield around the ionic core to study the interactions of a single ion in a Bose-Einstein condensate [37]. The latter was recently examined for a Rydberg S state [17] at the experimental setup where this thesis was conducted. The use of circular states could improve on the findings. However, an inner diameter of the doughnut shaped wavefunction larger than the diameter of the Bose-Einstein condensate to inhibit interactions between the Rydberg electron and the Bose-Einstein condensate would require a circular Rydberg state with a principal quantum number on the order of $n = 100$.

The above circularization methods where all carried out for principal quantum numbers below $n = 80$ or over $n = 300$, leaving a gap at the desired region. Further, the circularization of Rydberg states was not yet accomplished in an ultra cold atomic sample with a high fidelity [1], but were almost consistently conducted in atomic beam experiments. The preparation of circular Rydberg states in our ultra-cold Rubidium 87 experiment would therefore not only add a valuable method to our experimental toolbox, but would also pave the way for experiments fully exploiting the long life time, which is not possible in atomic beam experiments. Once trapped in an ultra-cold environment, CRS can be exploited for quantum simulations with excellent coherence times [48].

The goal of this thesis was therefore to investigate the possibilities of our ultra-cold Rydberg experiment to create circular Rydberg states at the example of the adiabatic rapid passage method and carry out preparatory calculations and measurements. The Rydberg F state is chosen as the initial state of the adiabatic rapid passage, since it is only weakly effected by the quantum defect but is still accessible by a three-photon laser excitation. Multiple challenges where discovered in preparing these states, originating from the high density of the atomic sample and not perfectly aligned magnetic fields. Besides that, a fast decay of the initial state was observed, which could not yet be contributed to a specific process and is not yet fully understood. To probe the fidelity of the excitation, a state selective field ionization scheme was applied. This allows for a distinction between the initial F state and the CRS and possibly intermediate states based on their different ionization threshold field. To investigate the stability and the response of the adiabatic passage method on non-optimal parameters, a simulation software was written, which can be used to investigate the limits of the adiabatic passage method for principal quantum numbers in the range of $n = 100$. This simulation can easily be extended to simulate not only the adiabatic rapid passage method but also other methods like the crossed fields method [13] which are based on adiabatic transfer.

Outline

In the first chapter of this thesis, the theoretical foundation to describe the adiabatic rapid passage circularization protocol and the involved methods is discussed. The main focus lies within the description of Rydberg atoms in external magnetic, dc and ac electric fields. The second chapter gives a brief overview of the experimental setup, focusing on the components important to the work of this thesis. The third chapter is structured into three main sections. The first one describes the calibration procedure of the radio frequency field involved in the adiabatic passage method. Followed by the investigation of the starting state of the procedure, the Rydberg F state, focusing mainly on the influence of a multitude of external factors onto its ionization behavior and lifetime. Further, a program was developed to simulate the adiabatic rapid passage as an open quantum system and the results from these simulations are discussed. In the end, experimental results of the ARP method are shown, where we find strong evidence that the protocol can be successfully implemented in our experimental setup.

Theoretical Foundation

In this chapter I will discuss the theoretical foundation, needed in the remaining chapters. First, a short overview of the properties of Rydberg atoms and their behavior in electric and magnetic fields will be given (Sec. 2.1, 2.2). Then the basics of circular Rydberg states and how to prepare them will be discussed (Sec. 2.4), followed by an introduction to the basics of Floquet theory, which we used to calibrate our radio frequency field (Sec. 2.5). Finally a short overview over the dynamics of open and closed quantum systems in the form of the von Neumann equation and the master equation in Lindblad form will be given.

2.1 Rydberg Atoms

In 1888 the Swedish physicist `Johannes Rydberg` developed a formula to describe the wavelengths of atomic transition spectral lines [59]. This so called Rydberg formula predicted the existence of an infinite number of discrete atomic states. Named in his honor, Rydberg atoms are atoms with a single electron excited to a high principal quantum number n. As this electron is most of the time at the classical turning points far from the ionic core, Rydberg atoms made from Alkali atoms can be described in an hydrogen-like manner [23]. For states with high orbital angular momentum l, the electron experiences the ionic core as a point like charge shielded by the remaining electrons. However for elliptical low-l states, the electron comes close to the core, resulting in a higher binding energy, because the electron penetrates the shielding electron cloud and encounters the higher charge of the unshielded core. These corrections can be taken into account by introducing the l-dependent quantum defect δ_l. This leads to a corrected binding energy of a Rydberg state

$$E = -\frac{R_\infty}{\mu(n-\delta_l)^2}, \tag{2.1}$$

where R_∞ denotes the Rydberg constant and

$$\frac{1}{\mu} = \frac{1}{m_e} + \frac{1}{m_{\mathrm{Rb}}}, \tag{2.2}$$

the reduced mass of the rubidium nucleus m_{Rb} and the electron m_e. By introducing the effective principal quantum number

$$n^\star = n - \delta_l, \tag{2.3}$$

the hydrogen atom theory is recovered. The quantum defects δ_l for the most relevant states are listed in Tab. 2.

Because many quantities scale with the principal quantum number n as can be seen in Tab 1, Rydberg atoms inhibit many interesting properties, all ahead the large polarizability and the long lifetimes.

2.2 Rydberg Atoms in External Fields

In this section the influence of electric and magnetic fields on the energetic structure of Rydberg atoms is investigated. The presented theory is based on reference [23] if not noted otherwise.

2.2.1 Zeeman and Paschen-Back Effect

The presence of external magnetic fields influences the level structure of atoms, which is especially important for high-l states, investigated in this thesis. The hyperfine splitting of Rydberg states is already very small against the Zeeman shift in very weak external magnetic fields and can therefore be safely neglected. In the limit of weak magnetic fields compared to the fine structure splitting, the fine structure interaction can be treated as perturbation and the total angular momentum quantum number, composed from the orbital angular momentum l and the electron spin s, $j = l + s$ stays conserved. In this case, the magnetic shift of a magnetic sub-level m_j is given by [21]

$$E_{\mathrm{ZE}} = g_J \mu_B B m_j \tag{2.4}$$

with the Landé factor

$$g_j = \frac{3}{2} + \frac{s(s+1) - l(l+1)}{2j(j+1)} \tag{2.5}$$

and the Bohr magneton μ_B.

If the magnetic field splitting dominates over the fine structure coupling, j is no longer a good quantum number. This regime is called the Paschen-Back regime, where the shift is given by, [21]

$$E_{\mathrm{PB}} = (g_l m_l + g_s m_s)\mu_B B. \tag{2.6}$$

In this equation, m_s and m_l are the magnetic quantum numbers of the spin s and the angular momentum l respectively. The Landé factors are given by $g_s \approx 2$ and $g_l \approx 1$.

The Rydberg states considered in this thesis lie between $n = 40$ and $n = 60$ and the magnetic fields are on the order of 10 G. In these scenarios, the low angular momentum states with $l < 3$ can be treated in the Zeeman regime. However, the fine structure splitting of the F states ($l = 3$) in question is on the order of $\Delta E_{\mathrm{FS}} = 1\,\mathrm{MHz}$ which is smaller than the magnetic field splittings, hence m_j is not a good quantum number anymore. In this case, the Paschen-Back regime must be considered. Dealing with both regimes raises the need for a uniform description which is also valid in the intermediate regime between the Zeeman and the Paschen-Back regime. This description is given by the Breit-Rabi formula [69]

$$E = -\frac{\Delta E_{\mathrm{FS}}}{2(2l+1)} + \mu_B B m_j \pm \frac{\Delta E_{\mathrm{FS}}}{2}\sqrt{1 + \frac{4 m_j x}{2l+1} + x^2} \tag{2.7}$$

with

$$x \equiv (g_s - 1)\frac{\mu_B B}{\Delta E_{\mathrm{FS}}}. \tag{2.8}$$

Table 1: Scaling behavior of some properties in Rydberg atoms with principal quantum number n [23].

Property	**Scaling**
Binding energy	n^{-2}
Orbital radius	n^2
Radiative lifetime	n^3
Polarizability	n^7

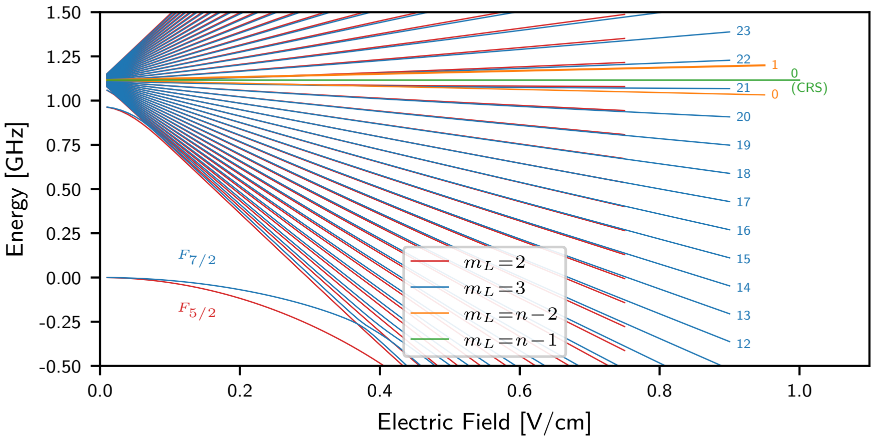

Figure 1: The Stark effect calculated for the example of the $n = 46$ Rydberg state for different m_L. The F state is split from the hydrogenic manifold due to the quantum defect. The numbers on the right show the n_1 quantum number of the states.

2.2.2 Stark Effect

Unlike the magnetic field interaction energy which does not scale directly with the principal quantum number n, the interaction with the electric field scales with the polarizability $\alpha \propto n^7$. Hence, electric fields have a strong influence on the energetic structure of Rydberg atoms. For a weak external electric field, the atomic levels are shifted. This shift is called the `Stark` effect. To calculate the altered energy levels we can employ a perturbative scheme. The interaction potential of the atom and the electric field $\boldsymbol{E}$ can be described by the interaction Hamiltonian

$$V = -\boldsymbol{E} \cdot \boldsymbol{p}, \tag{2.9}$$

where $\boldsymbol{p}$ is the electric dipole moment operator of the atom. The first order perturbation is then given by

$$E_1 = \langle n| V |n\rangle, \tag{2.10}$$

with the eigenstates $|n\rangle$ of the unperturbed H-like atom. For S-states ($l = 0$), this term vanishes because of the spherical symmetry whereby they do not inhabit an intrinsic dipole moment. By continuing the perturbation series to the second order, the quadratic Stark effect

$$E_2 = \frac{\alpha}{2} E^2 \tag{2.11}$$

can be obtained. This term does not vanish for S states and is caused by the mixing with other, nearby states with $l > 0$.

Under the influence of stronger electric fields, the angular momentum quantum number L is no longer preserved. To keep the problem separable, a parabolic basis can be applied. An eigenstate in the parabolic basis is described by the parabolic quantum numbers n_1 and n_2 which are connected by Clebsch-Gordon coefficients to the spherical basis set

$$|n, m_L, n_1, n_2\rangle = \sum_l |n, l, m\rangle \langle n, l, m|n, m_l, n_1, n_2\rangle. \tag{2.12}$$

They satisfy the condition

$$n = n_1 + n_2 + |m| + 1, \tag{2.13}$$

Table 2: Quantum defects for ^{87}Rb. The value for the F-state is from [28], the remaining from [39]

.

State	$S_{1/2}$	$P_{3/2}$	$D_{5/2}$	$F_{5/2}$	$F_{7/2}$
δ_0	3.131	2.642	1.346	0.01652	0.01654

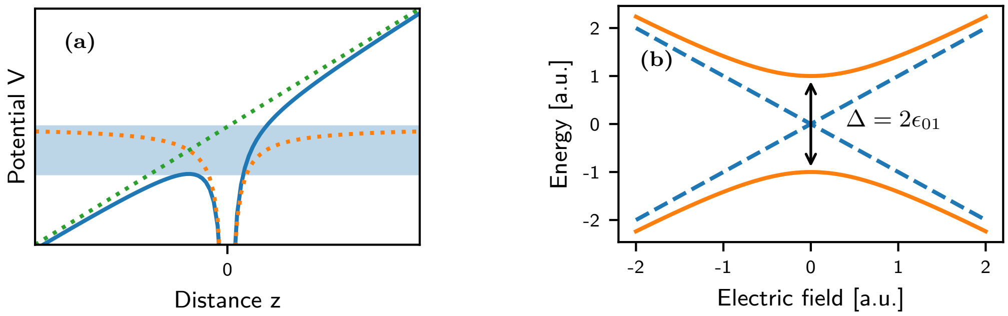

Figure 2: (a) Coulomb potential (dotted orange), electric potential (dotted green) and the total potential (solid blue) as a function of the distance from the atom core. For a pure Coulomb potential, states in the light blue shaded area are bound states, which are no longer bound in the presence of the electric field. **(b)** When two crossing states (blue) are coupled by an interaction, the resulting eigenstates (orange) exhibit an avoided crossing with a splitting governed by the interaction strength $\Delta = 2\epsilon_{01}$. If the parameter along the avoided crossing (Electric field in this example) is varied the crossing can be traversed adiabatically or diabatically along the dashed lines, depending on the speed of the variation.

making it obvious that there is only one state with maximum $m_L = n - 1$ for each n. The number n_1 describes the ellipticity of the wave function, for $n_1 = 0$, the orbit is circular whereas it gets more elliptical with rising n_1. A Stark map (SM) for $n = 46$ for different m_L is shown in Fig. 1a. We can see that the F-state (and also states with lower L) are not degenerate at zero electric field and are not part of the hydrogenic manifold. This is caused by the quantum defect (Eq. (2.3), Tab. 2). Since the quantum defect is negligible for $l > 3$, the states with $l > 3$ can be completely described in a hydrogenic manner. Nonetheless, for the states with $l < 3$, l and s are still approximately good quantum numbers as long as no states with higher l are mixed due to large electric fields. Since the energetic structure is very sensitive to changes in the electric field, we need to be able to control the external electric fields very precisely. With six electric field plates in a nearly cubic configuration and tailored methods to measure the electric field accurately (cf. 3.1,[17]) we reach a sub-$\mathrm{mV} \cdot \mathrm{cm}^{-1}$ accuracy in the experiment.

2.3 Landau-Zener Formula

As can be seen in Fig. 1a, the Stark states are arranged in a rather complicated manner caused by the coupling of a multitude of different states. States which are coupled can not cross, but exhibit so called avoided crossings [21]. When driving a system from one side of the crossing to the other, the state can traverse the avoided crossing in two different manners. If the system can reach an eigenstate during the whole process, the crossing is crossed adiabatically. If the crossing is traversed faster than the system can equilibrate to an eigenstate, the crossing is happens diabatically. For a finite crossing time, the Landau-Zener formula gives an easily accessible approximation to the probability of a diabatic transition [79]

$$p = \exp(-2\pi\Gamma), \tag{2.14}$$

with

$$\Gamma = \frac{\epsilon_{01}^2}{\hbar|\alpha|}. \tag{2.15}$$

The quantity ϵ_{01} is the coupling between the states part of the avoided crossing and

$$\alpha = \frac{\partial}{\partial t}(E_1 - E_0), \tag{2.16}$$

the temporal change of the energy difference of the two eigenstates $|0\rangle$ and $|1\rangle$. It generally applies, that if the crossing velocity $\alpha \gg \epsilon_{01}$ the crossing is traversed diabatically, if $\alpha \ll \epsilon_{01}$ the crossing is crossed adiabatically. The minimal splitting of the avoided crossing is given by the interaction energy $\Delta = 2\epsilon_{01}$.

2.3.1 Field Ionization

Large external electric fields can be used to ionize a Rydberg atom. The positive ion can then be accelerated onto an ion detector, which can be used to detect Rydberg states selectively by their ionization threshold field. The ionization process and the different ionization characteristics of low-angular momentum and high-angular momentum states will be discussed in the following.

By combining the Coulomb potential of the atomic core and the external electric field E to the potential

$$V = -\frac{1}{r} + Ez \tag{2.17}$$

the ionization field can be estimated classically by calculating the position of the maximum of the potential (cf. Fig. 2a). This leads to an ionization threshold field in atomic units of

$$E = \frac{1}{16n^4}. \tag{2.18}$$

States which lie above this maximum are no longer bound and therefore ionize. However, this result is only valid for states with $m = 0$, since states with $m \neq 0$ inhibit an additional centrifugal barrier. Further, neither the structure of the wave function nor the Stark shifts or quantum defects are included in this calculation, which implies that we need a more refined way to reliably calculate the ionization thresholds.

For states not significantly influenced by the quantum defect of rubidium ($m_l > 3$), the approach of Damburg and Kolosov [12] based on exact numerical calculations of H atoms can be used for calculating the ionization rates and threshold fields. The ionization rates are given by

$$\Gamma = \frac{(4R)^{m_l+2n_2+1}\exp\left[-\frac{2}{3}R - \frac{1}{4}En^3\left(7m_l^2 + 34m_l n_2 + 23m_l + 34n_2^2 + 46n_2 + \frac{53}{3}\right)\right]}{n^3 n_2!(m_l+n_2)!}. \tag{2.19}$$

In the equation above $R = {}^{(-2E_{\text{Stark}})^{3/2}}/_{E}$ and

$$\begin{aligned} E_{\text{Stark}} = &-\frac{1}{2n^2} + \frac{3}{2}n(n_1 - n_2)E - \frac{1}{16}n^4(17n^2 - 3(n_1 - n_2)^2 - 9m_l^2 + 19)E^2 \\ &+ \frac{3}{32}n^7(n_1 - n_2)(23n^2 - (n_1 - n_2)^2 + 11m_l^2 + 39)E^3 - \frac{1}{1024}n^{10}(5487n^4 \\ &+ 35182n^2 - 1134m_l^2(n_1 - n_2)^2 + 1806n^2(n_1 - n_2)^2 - 3402n^2m_l^2 \\ &+ 147(n_1 - n_2)^4 - 549m_l^4 + 5754(n_1 - n_2)^2 - 8622m_l^2 + 16211)E^4 \end{aligned} \tag{2.20}$$

is the Stark energy expanded to 4th order. However, this method is not applicable to states affected by the quantum defect. In the case of an finite size ionic core, n_1 and n_2 are no longer

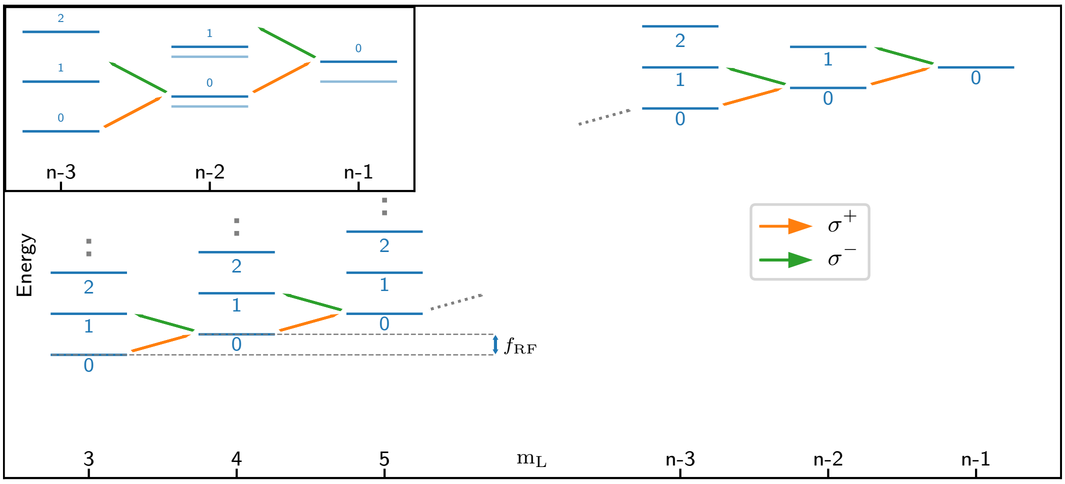

Figure 3: Principle of the RF-dressing of the hydrogenic manifold. The $n_1 = 0$ parabolic states of different m_l are coupled by a σ^+ polarized radio frequency field with frequency f_{RF}. To reduce the coupling to unwanted $n_1 = 1$ states, a magnetic field can be applied to shift the σ^- transitions out of resonance (inset).

good quantum numbers for those states. This lifts the degeneracy from the hydrogenic manifold states. Another important consequence of the quantum defect is that the blue and red states of adjacent Stark manifolds with n and $n-1$ do not cross as for hydrogen, but show avoided crossings. This sets a limit for the dc electric field used in the creation of circular Rydberg states since the states within the Stark manifold are no longer equally spaced in this regime. The manifold crossing can be calculated by the Inglis-Teller limit

$$E_{\mathrm{IT}} = \frac{1}{3n^5}. \tag{2.21}$$

By this change in the energetic landscape of those states at the manifold crossing the ionization behavior is also vastly changed. This will be discussed in depth in Sec. 4.2.2.

Chaudhuri et al. [8] used a WKB approximation approach to include the quantum defect in the calculation of the ionization thresholds. The ionization rates obtained by their calculation is given by

$$\Gamma = \omega \left(\frac{\beta}{E}\right)^{2n^\star - 1} \cdot \exp\left(-\frac{\beta}{E}\right), \tag{2.22}$$

where

$$\beta \equiv \frac{2\hbar^2}{3m_e e(n^\star a_0)^3} \quad \text{and} \quad \omega \equiv \left(\frac{m_e e^4}{4\hbar^3(\pi\epsilon_0)^2}\right)^{1/4} 6^{2n^\star - 1} a_0^3 |C(n^\star)|^2. \tag{2.23}$$

The factor $C(n^\star)$ is a normalization factor given by

$$|C(n^\star)| = \frac{2}{(n^\star a_0)^{3/2}\Gamma^\star(n^\star - 1)}, \tag{2.24}$$

where $\Gamma^\star$ is the gamma function.

2.4 Circular Rydberg States

Circular Rydberg states (CS) are the states with the highest angular momentum $l = n - 1$ and magnetic $m_l = n - 1$ quantum numbers for a given principal quantum number n [23]. They are of high interest due to there long intrinsic lifetime scaling with n^5 [48] and their distinctive interaction characteristics. With tailored trapping techniques, minutes of trapping time could be made possible [48]. Interesting applications for circular states include quantum computing [48] and quantum metrology [14]. A CRS wave function can be seen in Fig. 4a. The torus with a radius of $r = n^2 a_0$ has a width of $w = {}^{n^2 a_0}/_{\sqrt{n}}$ and forms the wave function closest to the classical Bohr orbit. The scaling of the proportion of radius and thickness of the torus of ${}^{r}/_{w} = \sqrt{n}$ makes it desirable to prepare circular states with high principal quantum number to reach large inner diameters. As can be seen in Fig. 1a (green) , the circular state does not have a first order Stark shift since there are no other states with the same m_L in the energetic vicinity [23]. At zero electric field it is degenerate with the remaining states of the hydrogenic manifold, hence it is not a stable state in this situation and a finite electric field is needed to stabilize the CS.

Since the excitation of a circular state involves the transfer of $n-1$ quanta of angular momentum, a simple laser excitation with the selection rule of $\Delta l = \pm 1$ for electric dipole transitions is not feasible. Multiple circularization methods have been successfully employed, which we will discuss briefly in the following.

Adiabatic Rapid Passage (ARP)

The adiabatic rapid passage relies on a radio-frequency (RF) dressing field to reach the circular state. This method was shown first in [32] with lithium for low principal quantum numbers of around $n = 20$ and later by [49] for rubidium at $n \approx 50$ at a high efficiency. The principle of the RF dressing is shown in Fig. 3a. The states of the hydrogenic manifold are split up by applying a static electric field, due to the linear Stark shift. By applying a radio-frequency field with the corresponding frequency f_{RF}, which is in this thesis typically between 150 MHz and 200 MHz, the states with $n_1 = 0$ of the different m_l ladders are coupled. This effectively couples the starting state $\langle m_l = 3, n_1 = 0|$ to the circular state $\langle m_l = n-1, n_1 = 0|$. For this coupling, a σ^+ polarized RF-field is needed. However we can not produce a pure σ^+ field in our experimental chamber, for that reason we need to consider the effects of a σ^- component. Since the states within the m_l ladders are equally spaced, the σ^- transitions are resonant on the same frequency as the σ^+ transitions. This would couple unwanted higher $n_1 \neq 0$ states. To circumvent this problem, a magnetic field is applied. This magnetic field shifts the m_l ladders in relation to each other due to their different Zeeman shift $E_B \propto m_l$ leading to a relative shift of $\Delta E_B = \mu_B B$. The $n_1 = 0$ states are thereby still equally spaced but the σ^- and the σ^+ transitions are shifted by $\Delta_\pm = 2 \cdot \Delta E_B$.

The adiabatic passage from $\langle m_l = 3, n_1 = 0|$ to the circular state $\langle m_l = n-1, n_1 = 0|$ is performed by starting with a slightly off-resonant RF-field. By varying the dc electric field, the transition frequency between adjacent $n_1 = 0$ states is varied and thereby the detuning of the RF-field, crossing the resonance at a given point. At the resonance point, the states form an avoided crossing due to their coupling, transferring the population of the F adiabatically to the CRS. The downside of this is that the need for an adiabatic process limits the speed of the method.

Optimal Control Assisted $\pi/2$ Pulse

By applying a purely σ^+ polarized radio frequency, resonant to the $nF \rightarrow nCRS$ transition, Rabi oscillations can be driven between the two states. By using a ${}^{\pi}/_{2}$ pulse, the population can be transferred to the CS. This gives a significant increase in speed over the method of the ARP. However, quadratic Stark shifts and the generally difficult level structure within the hydrogenic manifold make it difficult to find the right RF-pulse form. Patsch et al. [51] demonstrated an efficiency close to 100 % by using a pulse generated by optimal control methods.

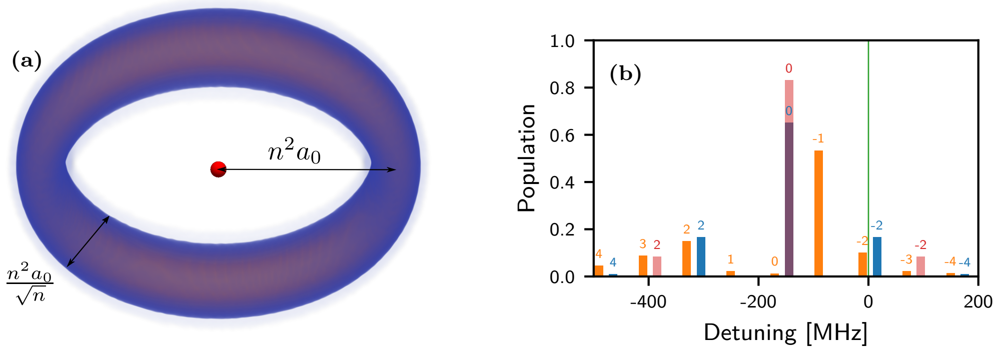

Figure 4: **(a)** Schematic wave function of a circular state with the atomic core (red) and the electronic wave function. The thin torus has a diameter of $n^2 a_0$, making it the state closest to the classical Bohr orbit. **(b)** Calculated position and population of Floquet sidebands for $E_{\mathrm{RF}} = 1\,{}^{\mathrm{V}}\!/_{\mathrm{cm}}$, $\omega = 80\,\mathrm{MHz}$ and $E_{\mathrm{dc}} = 0\,{}^{\mathrm{V}}\!/_{\mathrm{cm}}$ (blue) and $E_{\mathrm{dc}} = 0.3\,{}^{\mathrm{V}}\!/_{\mathrm{cm}}$ (orange) for a $71S$ state. For higher frequencies, the population of the sidebands decreases (red, $\omega = 120\,\mathrm{MHz}$, $E_{\mathrm{dc}} = 0\,{}^{\mathrm{V}}\!/_{\mathrm{cm}}$). The green line denotes to position of the unperturbed Rydberg line.

Other Methods

Circular states can also be produced by using pulsed electric fields [77] or by applying a crossed magnetic field and a time-varying electric field [13, 81, 5]. However the method of pulsed electric fields relies on electric field pulses with a frequency on the order of the Kepler frequency which is not feasible for the desired principal quantum numbers $n < 200$. Theoretical proposals also exist for the circularization by using Laguerre-Gauss beams [58] or by using the ponderomotive potential of a trapping beam [7].

The adiabatic passage is the most robust and easiest to implement, with the tools already present at the experimental setup, method of the lot. Hence, in the course of this thesis this method was investigated in depth, including simulations (Sec. 4.3.2) and preparatory experiments.

2.5 RF-Dressing of Rydberg States

In this thesis, spectroscopy of RF-sidebands is used to characterize the quality of the coupling of an applied radio frequency onto the atoms. The basic theory of these so-called Floquet sidebands will be discussed in this chapter, based on the work of van Dietzhuijzen et al. [15] and Zhang et al. [80].

Since the lower levels of the atom are not relevantly effected by the RF field due to their small polarizability compared to the Rydberg atom, we can treat the system as an effective two level system. The Hamiltonian can be written as

$$H = H_A + H_E \tag{2.25}$$

where H_A is the unperturbed atomic Hamiltonian and H_E the Hamiltonian describing the interaction between the atom and the electric field

$$E = E_{\mathrm{dc}} + E_{\mathrm{RF}} \cos(\omega t). \tag{2.26}$$

The electric field is given by a static term E_{dc} and an RF part, oscillating with frequency ω and amplitude E_{RF}. Both fields are considered colinear to the quantization axis. We separate the problem in a part dependent only on the spatial coordinate r and a part only dependent on the temporal coordinate t

$$\Psi(r,t) = \phi(r)\chi(t). \tag{2.27}$$

This separation is only exact for states with a linear stark shift, as for a quadratic Stark shift, the spatial part will also vary in time since neither l nor n_1 are good quantum numbers. For those states the shift is caused by mixing with several other l states. However, in our case this is not a problem, as the considered $71S$ state is, in electric dc fields up to $0.3\,\mathrm{V/cm}$, of over $95\,\%$ purity making Eq. (2.27) a good approximation. By solving the time dependent Schrödinger equation with this separation we obtain a solution for the temporal part

$$\chi(t) = \sum_{n_s=-\infty}^{\infty} \sum_{m=-\infty}^{\infty} J_{n_s-2m}\left(\frac{\alpha E_{\mathrm{dc}} E_{\mathrm{RF}}}{\hbar\omega}\right) J_m\left(\frac{\alpha E_{\mathrm{RF}}^2}{8\hbar\omega}\right) \exp\left(-\frac{i}{\hbar} W_s t + i n_s \omega t\right). \tag{2.28}$$

In the above equation

$$W_s = W_0 - \frac{1}{2}\alpha\left(E_{\mathrm{dc}}^2 + 2E_{\mathrm{dc}}E_{\mathrm{RF}}\cos(\omega t) + E_{\mathrm{RF}}\cos^2(\omega t)\right) \tag{2.29}$$

is the stark energy and J_n are Bessel functions. Equation (2.28) shows that the wave function has parts which oscillate with a multiple of the RF frequency $n_s\omega$. The amplitude of those sidebands is given by the Bessel functions. This amplitude vanishes for odd sideband numbers n_s if $E_{\mathrm{dc}} = 0$ because the argument of the first Bessel function is zero. This can be understood in terms of angular momentum conservation. For example for the sideband of order $n_s = 1$, the excitation can be understood as a two photon process with one laser photon and one RF photon. Without the coupling to the dc electric field, this transition is forbidden.

In Fig. 4b, the sideband structure of the $71S_{1/2}$ state for $E_{\mathrm{RF}} = 1\,\mathrm{V/cm}$ and $\omega = 80\,\mathrm{MHz}$ is depicted. The green line denotes the unperturbed Rydberg line. The first thing to notice is, that the zeroth order transition (the transition with no RF photon involved) is shifted from the unperturbed resonance by an ac-Stark shift given by

$$W_{\mathrm{RF}} = -\frac{1}{4}\alpha E_{\mathrm{RF}}^2, \tag{2.30}$$

induced by the RF electric field. Further, we can see that in the case of $E_{\mathrm{dc}} = 0$ (blue), not only are the odd sidebands not populated as stated before, but also that the sideband spectrum is symmetric with respect to the zeroth order transition. For a finite dc-electric field (orange in Fig. 4b), this symmetry is lifted. By increasing the amplitude of the RF field, more of the, in principle infinite number, of sidebands contribute to the wave function and the zeroth order population decreases, to a point where it is completely suppressed.

2.6 Dynamics of Open and Closed Quantum Systems

For simulating the adiabatic rapid passage (ARP) circularization method (see Sec. 2.4) we need to calculate the dynamics of the system during this protocol. In this chapter, the basic dynamics and the necessary equations are discussed. We start with the unitary Schrödinger evolution of a closed quantum system and proceed with the non-unitary Lindblad evolution of an open quantum system, which we can use to model the transitions to other, unwanted states during the ARP due to the σ^- polarized part of the RF field. The section is based on [30] if not noted otherwise.

A quantum state in a closed system can be described by a density operator ρ in a fully general alternative formalism to the description by its state vector $|\Psi\rangle$. By choosing a basis, the density matrix describes the classical probability distribution of the basis states $|\Psi_k\rangle$ in a matrix representation

$$\rho(t) = \sum_k p_k(t) \left|\Psi_k\right\rangle \left\langle\Psi_k\right| , \tag{2.31}$$

where $|p_k(t)|^2$ is the classical probability to find the system in state $|\Psi_k\rangle$. In this description, the von Neumann equation

$$i\hbar \frac{\partial \rho}{\partial t} = [H(t), \rho] , \tag{2.32}$$

where $[\cdot, \cdot]$ is the commutator of two operators, governs the dynamics of ρ under a unitary Hamiltonian H. This equation is equivalent to the Schrödinger equation and can be derived from it. In Eq. (2.32) the system Hamiltonian $H(t)$ is generally time dependent. For a time independent Hamiltonian $H(t) = H$ however, it can easily be solved to obtain the integrated form of Eq. (2.32)

$$\rho(t) = \exp\left(-{}^{iHt}\!/\!{}_{\hbar}\right) \rho(0) \exp\left({}^{iHt}\!/\!{}_{\hbar}\right) . \tag{2.33}$$

Certainly the density matrix formalism is useful for the unitary dynamics but it is even more significant for calculating the dynamics of open quantum systems which are of stochastic nature. An open quantum system is a quantum system which is coupled to its environment, which induces stochastic transitions between the states of the system and introduces de-phasing. The complete system, including the environment can again be viewed as a closed system, governed by the von Neumann equation

$$i\hbar \frac{\partial \rho_{\text{tot}}}{\partial t} = [H_{\text{tot}}, \rho_{\text{tot}}] , \tag{2.34}$$

where

$$H_{\text{tot}} = H + H_{\text{env}} + H_{\text{int}}, \tag{2.35}$$

is the total Hamiltonian, including the Hamiltonian of the environment H_{env}, the Hamiltonian of the original system H_s and the interaction between the environment and the system H_{int}. As the environment is typically very large it is often difficult or impossible to find an exact solution to the time evolution of such a system. However, we are only interested in the time evolution of the original system $\rho(t)$. If we assume that the environment and the system are uncorrelated at all times, we can perform a partial trace over the environmental degrees of freedom and obtain a master equation, describing the non-unitary evolution of the system density matrix $\rho(t)$. The most general master equation with Markovian property is the Gorini-Kossakowski-Sudarshan-Lindblad (GKSL) equation

$$\frac{\partial \rho}{\partial t} = -\frac{i}{\hbar} [H(t), \rho] + \sum_n \gamma_n \left(V_n \rho V_n^\dagger - \frac{1}{2} \left(\rho V_n^\dagger V_n + V_n^\dagger V_n \rho \right) \right) , \tag{2.36}$$

where V_n are the operators through which the system couples to the environment and γ_n the corresponding decay rates. The Markovian approximation used to reach master equation in Lindblad form states that the time-scale of the decay of the environment must be much faster than any system dynamics. To ensure the validity of this approximation and the condition that the system and the bath are uncorrelated at all times, the decay rates γ_n must be much smaller than the energy splittings in the system.

Experimental Setup

In this section the experimental setup and its control is briefly described. This overview focuses only on the most important parts for the work in this thesis. For a more complete description on the setup, see [61, 57, 71, 63]. Most of this chapter is based on those theses.

The experimental apparatus is used to excite ^{87}Rb Rydberg atoms in an ultracold thermal gas or in a Bose-Einstein condensate (BEC). To form a BEC, the atoms need to be cooled below the critical temperature T_C which is typically on the order of μK. The first step in order to obtain such low temperatures is the use of a magneto optical trap (MOT) [52]. In the MOT chamber (right in Fig. 1), the atoms are loaded from the background gas into the magneto optical trap. The background pressure of Rubidium atoms of typically 10^{-8} mbar is given by the equilibrium between vacuum pumps and the stream of Rubidium atoms outgassing from the reservoir. After the loading of the MOT, using the $5S_{1/2}, F=2 \rightarrow 5P_{3/2}, F=3$ transition as cooling transition, the atoms have a temperature of a few hundred μK. They are further cooled by compressing and are optically pumped into the low-field seeker $5S_{1/2}, m_F = 2$ state. Atoms in this state are then transported into the science chamber by a magnetic transport. The low-field seeker state (negative Zeeman shift) will always move to a lower, energetically more favorable magnetic field. By shifting the minimum of the magnetic field by twelve pairs of coils in anti-Helmholtz configuration, the atoms can be moved to the science chamber (left in Fig. 1).

In the science chamber, the atoms need to be cooled further since they are heated by the magnetic transport. Therefore an evaporative cooling technique is applied [21]. In this method, the hot atoms in the tail of the Boltzmann distribution get ejected from the trap by a radio frequency field. After re-thermalization, the temperature of the remaining atoms is lower. The evaporative cooling is done in three steps consisting of a linear down-ramp of the RF frequency and a wait time to let the gas re-thermalize. The temperature of the atoms can then be varied by varying the final frequency of the RF ramp.

3.1 Electric Field Compensation Box

The science chamber consists of a compensation box and a mircochannel plate detector (MCP) and the ion optics to focus the ions onto different channels of the MCP (Fig. 2). This box is placed inside a glass tube to allow for good optical access and a compact design. The trapping is achieved by the employment of coils for the magnetic field control and thus the compactness is desirable since placing the coils as close as possible to the atoms keeps the needed current and by extension the cooling to a minimum. The box is designed to control the electric fields with a high precision and shield the atoms from electric stray fields. It is fabricated from an almost non-magnetic but highly conductive stainless steel, making it resistant to oxidation processes [31]. By spanning thin wires across the optical access holes of the chamber, the shielding and the homogeneity of the electric field can be further improved. With a diameter of $25\,\mu$m and spacing of 4.5 mm the wires do not influence the laser beams. However, they act as a polarizer

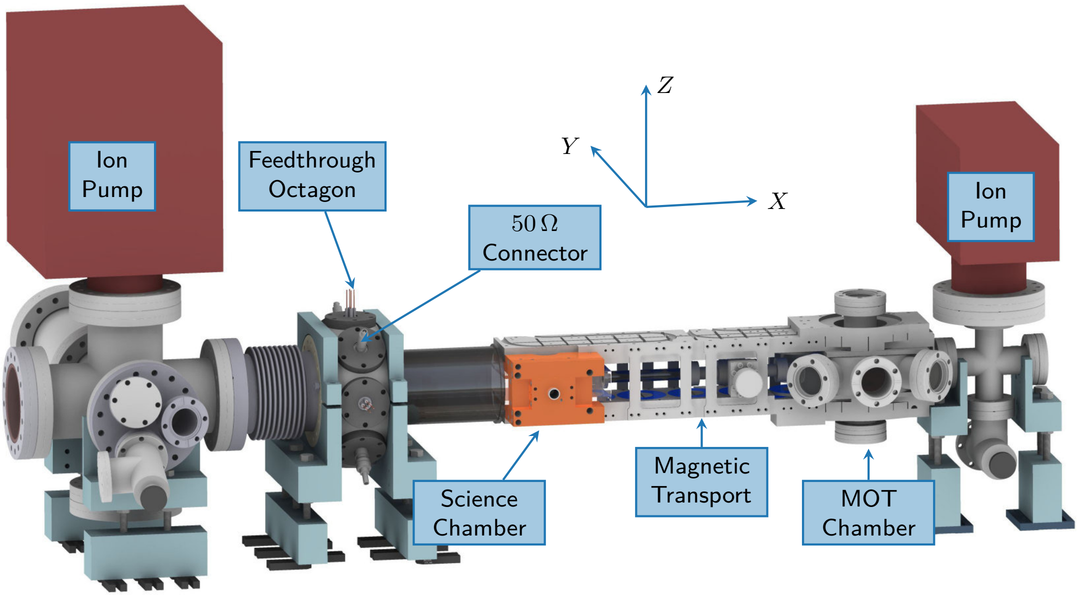

Figure 1: Drawing of the vacuum setup with MOT chamber, atom transport and science chamber. The electric field plates (Fig. 2) and detection electronics are connected through the feedthrough. Some electric field plates can be optionally terminated by $50\,\Omega$ at the feedthrough octagon (from [63] (slightly modified)).

on the much larger wavelength of the used microwave. Nonetheless, it was shown by Marian Rockenhäuser [57] that this is not an issue since the microwave mainly couples to the atoms via an evanescent field. The precise control of the electric fields given by this setup is important for conducting Rydberg experiments due to the high field sensitivity of the Rydberg atoms (cf. Chap. 2.2).

3.1.1 Methods to Compensate Electric Stray Fields

To measure the electric stray fields to a similar high accuracy as our setup allows us to compensate, we make use of the quadratic Stark shift of high-n Rydberg states. The electric field is scanned in each direction and for every voltage step, a spectrum is taken by varying the frequency of the Rydberg laser (cf. Sec. 3.3). From this spectrum the resonance of the transition can be extracted. By fitting a parabola to the resonance position, the position of the smallest Stark shift can be obtained (cf. Fig. 4b). By repeating this process in all three dimensions, an arbitrary stray field can be measured and compensated. Usually, the electric field is applied by applying a symmetric voltage on two opposing field plates of the compensation box. By using a high-n Rydberg state for the measurement, we obtain a sub-$^{\mathrm{mV}}/_{\mathrm{cm}}$ accuracy [17]. However, the electric stray fields are prone to drifting over time with a rate on the order of a few $^{\mathrm{mV}}/_{\mathrm{cm}}$ per day. This effectively limits the measuring time without compensating the electric field in between. To address this issue, an automated routine, which allows the non-supervised measurement of a Stark map and compensation during an arbitrary measurement, was developed during this thesis. An in-depth description of this routine can be found in Appendix A.

3.1.2 Field Ionization and Ion Detection

The creation of a Rydberg atom is detected by state selective field ionization (see Sec. 2.3.1). The so produced ions are then accelerated onto a microchannel plate detector (MCP) [76]. To

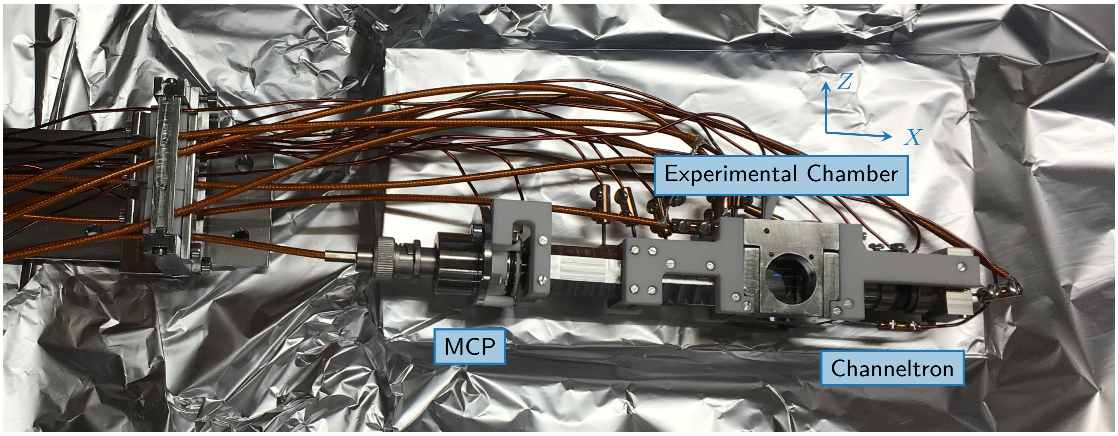

Figure 2: Electric field compensation box, before installation inside the glass chamber (2016). The MCP ion detector and the electric field plates are connected to the outside of the vacuum through a feedthrough octagon (Fig. 1). The channeltron is currently not connected.

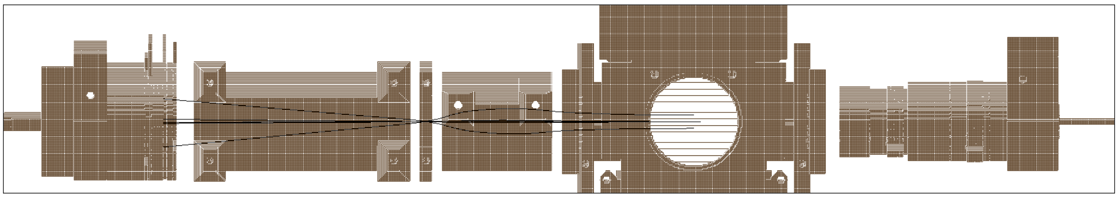

Figure 3: SIMION simulation of the ion trajectories starting in the science chamber (middle). The ions are then focused by an ion lens and spread over multiple channels on the MCP. [31]

spread them across the whole sensor area, an electrostatic three-cylinder einzel lens between the science chamber and the MCP are used (cf. Fig. 3). To reach the necessary ionization field of the Rydberg states used in this thesis (mainly around $n = 50$), two devices are used:

1. The electric field compensation and the electric field control during the Rydberg excitation is done by a computer controlled USB power supply. For the ionization, a high voltage switch (`CGC NIM-AMX500-3`) switches from the low voltage supply to a high voltage supply (`TDK Lambda Z+`). The slew rate of the produced pulse is $\approx 400\,{}^{\mathrm{V}\mu\mathrm{s}}/_{\mathrm{cm}}$.
2. The electric field compensation voltage and the ionization voltage is both produced by an arbitrary waveform generator (AWG) (`Keysight 33522A`). However, because the AWG is limited to 20 V, a low-noise amplifier with an amplification factor of -39.68 is used to reach the necessary voltages.

The advantage of the second setup lies mainly in the flexibility of the AWG. Whereas the first setup can only produce a pulse signal for the field ionization, the AWG can produce arbitrary ramp signals. This is necessary to separate different states during a single ionization sequence. However, the amplification also amplifies noise, generated by the AWG or picked up by the wire between the AWG and the amplifier. Further, the amplitude resolution of the AWG is 0.15 mV, which results in an amplitude resolution after the amplification of 6 mV. This does not only mean, that our electric field compensation accuracy is limited to this value, but also that the electric field ramps used in the experiment consist of voltage steps of 6 mV.

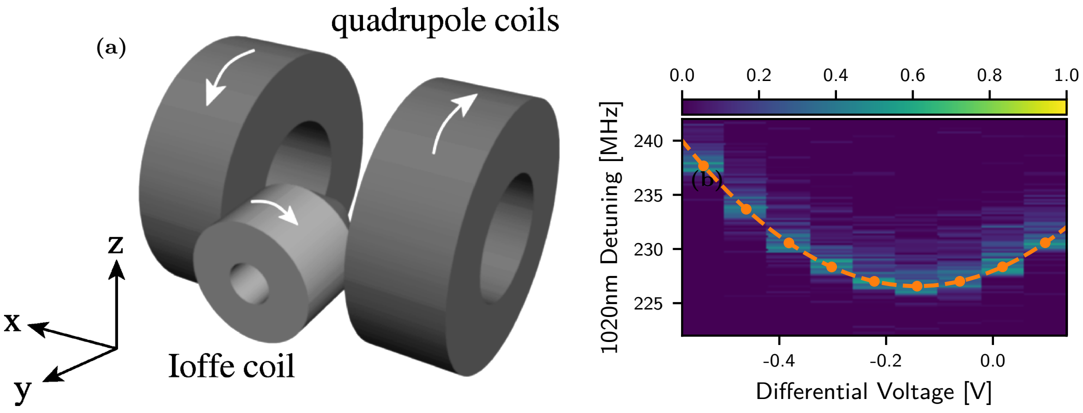

Figure 4: (a) Configuration of the magnetic coils in a quadrupole in Ioffe configuration (QUIC) trap with anti-Helmholtz pair and Ioffe coil. The arrows indicate the direction of the current (taken from [18]). **(b)** A Stark map of the $71S$ state measured by varying the electric field in the z direction. The color represents the mean ion count. By fitting a parabola to the resonance peaks, the compensation field value can be extracted (minimum of parabola).

3.2 Trapping in the Science Chamber

For trapping the atoms inside the science chamber, we have two different traps to our disposal. First, a magnetic quadrupole in Ioffe configuration (QUIC) trap and second an optical dipole trap.

QUIC-Trap

The QUIC trap [18] uses a pair of coils in anti-Helmholtz configuration and an additional, perpendicular Ioffe coil (Fig. 4a). The important advantage of this design compared to a vanilla quadrupole trap is the non-zero magnetic field at the trap center. The zero crossing in a vanilla trap would introduce Majorana spin-flip transitions [44, 6] to non-trappable states, causing atom loss. The trap frequencies of this configuration are

$$\omega_x = 193\,\mathrm{Hz}, \quad \omega_y = 193\,\mathrm{Hz} \quad \text{and} \quad \omega_z = 15.6\,\mathrm{Hz}. \tag{3.1}$$

Optical Dipole Trap

After the evaporative cooling in the QUIC trap, an additional optical dipole trap [24] can be switched on. This trap consists of a narrow lightsheet [27] with a beam waist of $10.1(20)\,\mu\mathrm{m}$ and a second, perpendicular beam with a waist of $75\,\mu\mathrm{m}$, both at a wavelength of 1064 nm. The lightsheet is used to trap the atoms in a quasi-2d confinement in the x-y plane of the science chamber. Combined with the second beam propagating in z-direction, the trap frequencies of this setup are

$$\omega_x = 163\,\mathrm{Hz}, \quad \omega_y = 116\,\mathrm{Hz} \quad \text{and} \quad \omega_z = 709\,\mathrm{Hz}. \tag{3.2}$$

As the atoms are loaded from the magnetic trap to the optical dipole trap with a finite efficiency the atom numbers in the optical dipole trap are typically lower. However, the higher atom number and therefore better statistics come at the price of less flexibility. Due to the finite magnetic field at the trap center of $\approx 1.7\,\mathrm{G}$, the quantization axis is fixed in the y-direction. The optical dipole trap inhabits no such limitations and the quantization axis given by the magnetic field can be chosen in an arbitrary direction, which is important for studying field ionization processes.

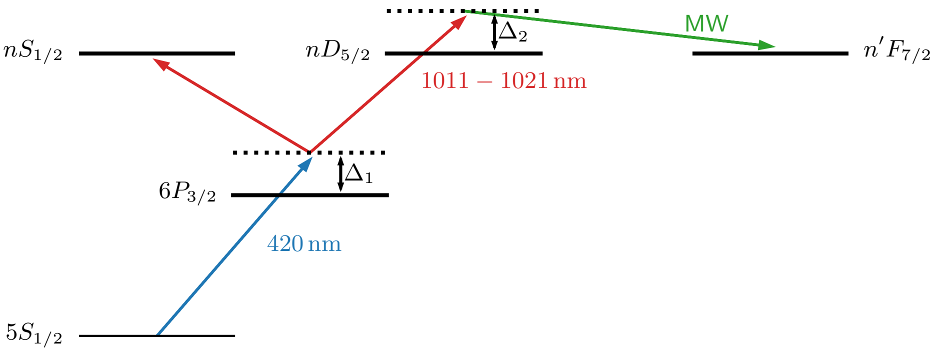

Figure 5: Scheme of the Rydberg excitation used in the experiment. In a two photon process using a 420 nm and a 1020 nm laser, a Rydberg S or D state can be excited in an off-resonant two photon process. By using an additional microwave transition a Rydberg nF state can be excited via an off-resonant three photon process.

3.3 Three Photon Excitation Scheme

After the trapping of the ground state atoms, it is possible to do high resolution spectroscopy of Rydberg states. To excite atoms to a Rydberg state, we make use of an inverted scheme (Fig. 5a). The $5S_{1/2}$ ground state of Rubidium 87 is excited by an off-resonant two photon process involving a 420 nm laser photon and a second photon with a wavelength of 1011-1021 nm. The second laser, called the Rydberg laser, can be tuned in frequency to address different Rydberg levels. The detuning of the 420 nm laser to the intermediate $6P_{3/2}$ state is typically chosen to be $\Delta_1 = 160\,\text{MHz}$. By varying the polarization of the two laser beams, with this two photon process we can excite Rydberg nS and nD states with m_j between $m_j = -3/2$ and $m_j = 5/2$. For the work in this thesis, the stretched state $nD_{5/2}, m_j = 5/2$ reached by two σ^+ polarized photons is of most importance. The 420 nm laser beam propagates along the y-axis of the science chamber and illuminates the whole atomic cloud. The 1020 nm laser is focused by a high-NA aspheric lens, mounted inside the bottom electric field compensation plate. Therefore the beam propagates along the z-direction of the science chamber. This means, that we can not achieve pure σ^+ polarized light for neither of the two laser beams, when conducting experiments with the quantization axis set to the x-axis. The tight focus of $2.1(3)\,\mu$m of the 1020 nm Rydberg laser is typically smaller than the blockade radius r_B [43] of the Rydberg state. With this, we are able to excite a single Rydberg atom in the cloud.

The initial state of the adiabatic rapid passage circularization process (Sec. 2.4) however is the nF state. Since the latter can not be reached by a two photon process, a microwave (MW) setup was recently implemented to the experiment [57]. This enables us to implement an off resonant three photon process with a second detuning Δ_2 from the D state resonance reached by the laser photons to reach the desired nF states. A more detailed investigation of this process is given in [57] and an evaluation which D state to choose is done in Sec. 4.2.1.

3.4 Experiment Control

Almost all parameters of the experiment are controlled by several `National Instruments Compact DAQ` digital and analog I/O cards and a Swabian Instruments pulse generator for high resolution digital outputs. The components are programmed by an in-house developed software package [61], written in `C#`. This main experiment control program also handles the

`MySQL` database in which all the input variables are stored for further use and evaluation, sorted by a running index unique to every cycle of the experiment, called *global counter* in the following.

The sequences of the input parameters are entered via a graphical interface which is shown in Appendix A.1a for the example of an analog card. Those sequences, including the input variables can be saved and loaded as *models*. In the so-called *advanced mode*, multiple of those models can be loaded and, controlled by a python script, processed one after the other. In this thesis this newly implemented mode was tested (cf. Appendix A). The control is capable of doing multidimensional variable scans within one model. Therefore, the user has three types of input variables to his disposal:

- *Static* variables are used to input variables that do not change during the model. Those variables can not be changed by the advanced mode python script or by *iterator* variables. Static variables need to be floats and can not be composed of other static variables.
- *Iterator* variables are used to conduct scans within one model. They have a start value, an end value and a step size. The value of the iterator is incremented by the step size after each cycle of the experiment. Iterator variables can change dynamic variables but not static variables.
- *Dynamic* variables are used for parameters which need to be calculated from other variables. It is possible to use all kinds of variables (static, iterator or dynamic variables) in the calculation. Variables of this type are the only ones accessible by the advanced mode python script.

The experiment control also sends the current global counter to the oscilloscope (`LeCroy Waverunner`) which records the ion detection events on the MCP. Those ion traces are stored on a network-attached storage (NAS), identifiable by the global counter. The evaluation of the traces is done automatically or manually on an additional computer, extracting the times and number of ion detection events.

Towards Circular Rydberg States

The main goal of this thesis was to investigate the creation of circular Rydberg states via the adiabatic rapid passage method (see Sec. 2.4). Applying this method involves a variety of challenges had to be addressed. In the first part of this chapter, the efficiency at which an RF field can be applied to the atoms is investigated by measuring Floquet sidebands (Sec. 4.1), followed by the investigation of the ionization behavior of the starting state for the adiabatic rapid passage, the Rydberg F state. We find that factors concerning the electric field and the magnetic field as well as collisions play a crucial role for successfully reaching the starting state (Sec. 4.2). In the final section, a program was designed to simulate the adiabatic rapid passage protocol. With this, the influence of different parameters onto the success of the procedure is investigated and its limitations are discussed (Sec. 4.3.2).

4.1 Calibration of the Radio Frequency Field

For the adiabatic rapid passage circularization method (see Sec. 2.4) a radio frequency field is used as a dressing field to couple the involved atomic states. Since such a field was not used in previous experiments, we need to investigate the efficiency with which the field can be applied onto the plates of the electric field control box and thereby how well it can be transmitted onto the atoms. For the generation of the RF-frequency we use a `Siglent SDG6022X` 200 MHz arbitrary waveform generator (AWG), directly connected to the field plates. A characterization of this device can be found in Appendix D. The use of an AWG gives us the advantage to generate the RF field and the needed dc fields for stray field compensation with a single device without the need for a bias tee[1] or similar additions as it would be needed for the use of a standard frequency synthesizer. We are able to generate sinus functions of up to $6\,\mathrm{V_{pp}}$ amplitude and up to 200 MHz with this setup. The lower frequency limit compared to conventional frequency synthesizers does not limit us significantly in the passage frequency, as the maximum usable splitting of the stark states is limited by the Inglis-Teller limit anyways.

To investigate the efficiency of the generation of the electric field inside the experimental chamber by the applied RF voltage function we spectroscopically investigate the creation of Floquet sidebands (Sec. 2.5). In this section the results of this calibration measurements are presented and we find that the efficiency is strongly dependent on which electric field plate is used.

The atom is excited to a Rydberg $S_{1/2}, m_j = 1/2$ state by the typical off-resonant two-photon process (see Sec. 3.3) and additionally the radio frequency field is applied during this sequence (Fig. 1a). This allows transitions to the target Rydberg state not only by the two-photon process but also by multi photon processes involving one or multiple RF photons, leading to the creation of sidebands shifted from the Rydberg line by multiples of the RF frequency f_{RF}. An example measurement for three different RF amplitudes at a frequency of $f_{RF} = 50\,\mathrm{MHz}$ is shown in Fig.

---

[1] A three-port device, which allows to set the dc bias point of an electronic component without influencing an RF signal applied to it [45]

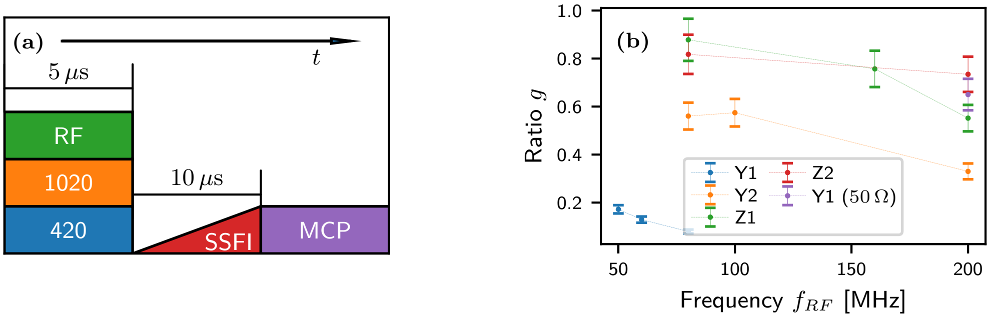

Figure 1: (a) Schematic of the Rydberg creation and detection sequence for measuring Floquet sidebands. The Rydberg state is excited in a multi-photon process and then ionized by state selective field ionization (SSFI) and detected on the MCP. **(b)** Frequency dependent ratio g of applied and measured RF field for the four different electric field plates of the experiment chamber in y and z direction. The lines are guides to the eye. For increasing frequency the efficiency decreases for all plates.

2. The spectrum is measured in the magnetic trap (dots) with the RF field applied in y-direction along the quantization axis given by a magnetic field of 3 G. The excitation duration during which the RF field and the lasers are switched on is 5 μs for all measurements. At zero detuning there is a residual Rydberg peak which implies that the RF field does not influence all Rydberg excitations as they are not subject to the ac-Stark effect as the zeroth order signal. This could be explained by a slight delay in the RF pulse compared to the laser pulses. In this case, a Rydberg atom can be excited just by the two lasers before they are subject to the RF field and due to the Rydberg blockade no further excitation can be observed when the RF pulse kicks in. In the plot, the $-1^{st}, 0^{th}$ and $+1^{st}$ Floquet bands are well visible for all three RF amplitudes. The odd sidebands are visible due to the applied dc electric field of 0.38 V/cm. A broadening of the lines for higher RF-field is noticeable. For higher fields, the field sensitivity of the S state rises due to its quadratic Stark effect, therefore field gradients across the atomic cloud have a larger effect on states in a larger electric field, causing broader lines.

To extract the population and position of the sidebands, a sum of Lorentzians

$$P(\Delta) = \sum \frac{n}{\left[1 + \left(\frac{\Delta - \Delta_0}{\gamma}\right)^2\right]} \tag{4.1}$$

is fitted to the spectrum. Here, Δ denotes the detuning of the Rydberg laser from the resonance of the unshifted resonance, n the height of each peak and 2γ the full width at half maximum (FWHM). By fitting (2.28) to the obtained populations and positions of the sidebands, the RF field amplitude and the dc field can be extracted. Since we are able to measure the dc field by measuring the dc-Stark shift (see Sec. 3.1.1) separately, the theory can be fitted with the RF-field amplitude as the only degree of freedom. It can be seen from the plot, that the applied theory fits well to the measured spectrum, both the populations of the sidebands and the positions. As the RF amplitude is the only fit parameter, it can be extracted from only the position of the zeroth order sideband, which is given by the ac-Stark shift. It is thereby sufficient to measure only the ac-Stark shift and refrain from the time costly sideband measurements. This is especially useful since the population of the sidebands decreases rapidly for increasing frequencies (see Fig. 4b), which would require longer measurements to obtain statistically meaningful data. Further, we do not need to apply a dc-electric field, which decreases the broadening of the Rydberg lines.

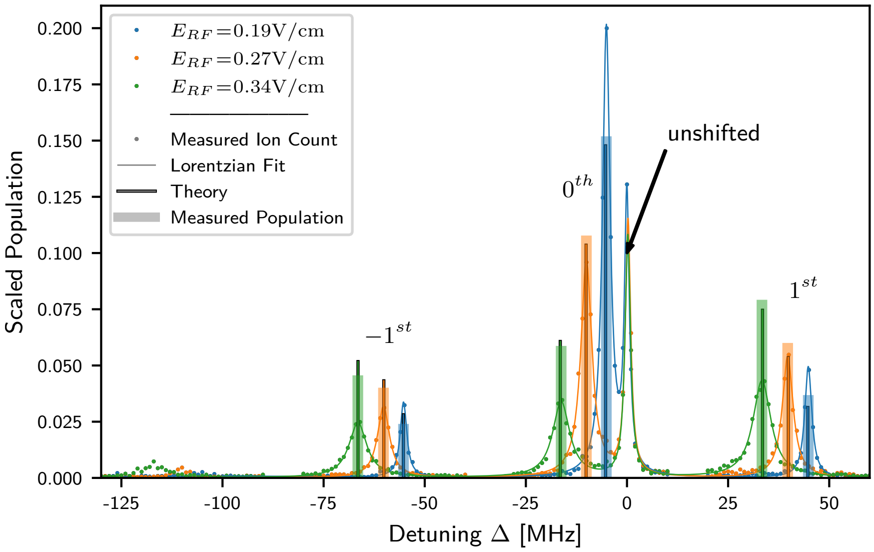

Figure 2: Measurement of Floquet sidebands for a $71S$ state with a 50 MHz radio frequency field applied. The x-axis is given by the detuning of the two-photon process to the Rydberg state. The measured ion count is scaled up for visual clarity. The colors visualize measurements at different applied RF amplitudes whereas the different markers distinguish between fitted and measured data. The thin bars represent the fitted theory whereas the thick bars represent the measured population and peak positions. The measured populations are defined by the area under the respective peak, divided by the total signal of the measurement [1].

[1] The residual bare Rydberg peak is excluded from the total signal, since it is not part of the Floquet excitation scheme.

An exemplary measurement of the ac-Stark shift of the $71S$ state for varying RF amplitudes U_{set} with $f_{RF} = 200\,\text{MHz}$ applied to the $Y2$ plate of the experiment chamber is shown in Fig. 3. By fitting Eq. (2.30) with a known polarizability of $\alpha = 289\,{}^{\text{MHz}}/_{\text{V/cm}^2}$ [50] to the shifted Rydberg line, the electric field E_{RF} can be obtained and compared to the applied electric field

$$E_{set} = \frac{U_{set}}{2\epsilon}. \tag{4.2}$$

In this expression, $\epsilon = 2.8\,\text{cm}$ is the plate distance of the capacitor created by two opposing plates of the experiment chamber. The factor of 2 accounts for the conversion between the voltage U_{set} given in V_{pp} and the electric field given as an amplitude. The ratio

$$g = \frac{E_{RF}}{E_{set}} \tag{4.3}$$

represents a correction factor which needs to be taken into account when applying RF fields to the atoms. The applied electric field is measured with a high accuracy multimeter. It turns out that the AWG has a high discrepancy between the output voltage U_{out} and the voltage set in the user interface of the AWG U_{set} for high frequencies (see Sec. D). This deviation is taken into account for the measurements by Eq. (D.1). For the measurement of Fig. 3 the ratio is for example $g = 0.76$. A ratio of $g < 1$ implies that not the full amplitude of the applied signal reaches the electric field plates but is reflected back. Since such back reflection is strongly dependent on the frequency of the applied signal, the ratio g will also be frequency dependent. To obtain the frequency dependence, measurements for multiple frequencies for the different field compensation plates were conducted. The resulting ratios g are plotted in Fig. 1b for the four electric field plates of the experiment chamber in y and z direction. The plates in x direction were not used in

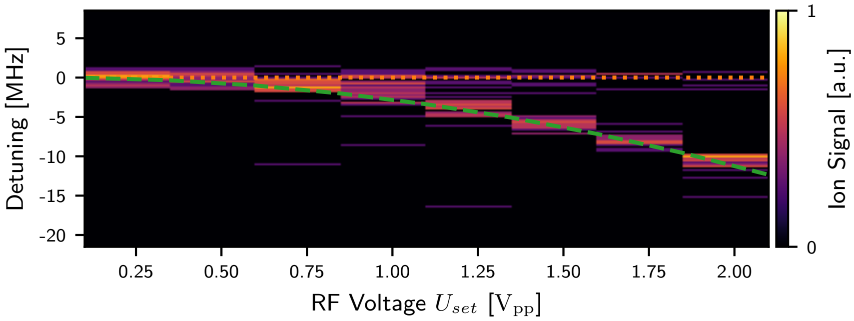

Figure 3: Ac-Stark shift measurement for varying RF voltages U_{set} with $f_{RF} = 200\,\mathrm{MHz}$ of the $71S$ state. From the detuning of the shifted line from the unshifted Rydberg line (dotted orange), the strength of the applied RF field can be extracted by fitting Eq. (2.30) (dashed green).

the measurements as they are used for field ionization. The amplifier used for ramped ionization as well as the high voltage switch used for pulsed ionization (see Sec. 3.1.2) act both as a low pass filter, rendering these two plates unpractical for applying radio frequency fields. From Fig. 1b we can see that the RF field is transmitted satisfactorily by the $Z1, Z2$ and the $Y2$ plates, reaching a efficiency ratio between $g = 0.35$ and $g = 0.75$ at $f_{RF} = 200\,\mathrm{MHz}$. However, the $Y1$ plate is conveying below $20\,\%$ of the applied RF amplitude onto the atoms already at frequencies as low as $f_{RF} = 50\,\mathrm{MHz}$. At $f_{RF} = 200\,\mathrm{MHz}$, no effect of the applied RF field was measurable.

To understand this vast difference, we need to take into account the different styles of electrical connections of the plates. All six field plates of the experiment chamber are open ended. This means there is no impedance matching between the wire running to the plate and the plate itself, leading to reflections and possibly standing waves in the wire, suppressing the applied signal [20]. Since the six plates are approximately of same shape and size and manufactured from the same material, this does not explain a vast difference between different plates. In contrast to the other studied field plates, it is possible to terminate the $Y1$ plate with an $50\,\Omega$ resistor to match the impedance. However, the port for connecting this resistor is at the octagon (see Fig. 1), where all electric connections are led through to the vacuum. This leads to a wire length between the resistor terminal and the field plate itself of $\approx 40\,\mathrm{cm}$. In the wire between the plate and the AWG, the reflections are damped by the input resistance of the AWG making them less relevant. However this is not the case for the connection between the plate and the resistor terminal, leading to reflections and possibly destructive interference at the site of the field plate. By adding a $50\,\Omega$ resistor to the terminal the impedance can be matched and the effect can be decreased. The measured electric RF field ratio can thereby be improved to $g = 0.65$ at $f_{RF} = 200\,\mathrm{MHz}$. This makes the $Y1$ plate comparable to the other plates studied.

A significant connection between the length of the used BNC cable between the AWG and the experiment and the ratio g could not be found, which implies that resonances and standing waves within the connection cable are not the cause for a decrease in the ratio g. Further, there was no evidence found for a dependence of g on the applied voltage.

We can conclude that it is possible to apply the desired frequencies of $200\,\mathrm{MHz}$ used for the adiabatic rapid passage circularization method (see Sec.2.4) to the two field plates in Z direction. Moreover we received an approximate frequency dependent scaling factor of the voltage applied to the plates to generate the desired electric RF field at the atom site. This leads to a maximum RF field amplitude of $\approx 1\,\mathrm{V/cm}$ for a single plate at $f_{RF} = 200\,\mathrm{MHz}$, limited by the voltage output of the AWG and a scaling factor g.

Note, that by this method the total amplitude could be extracted but it does not give any evidence

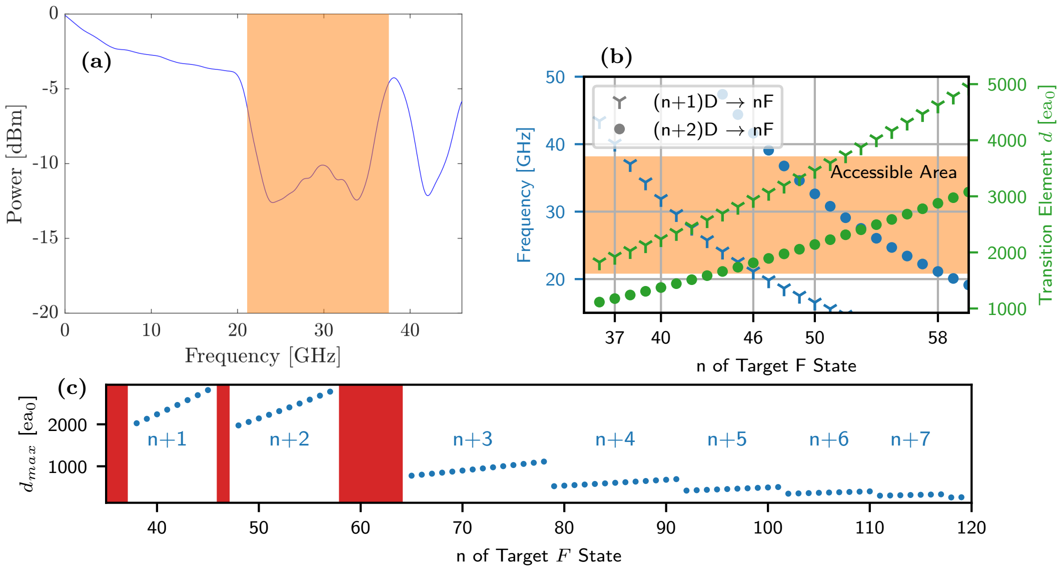

Figure 4: (a) The back reflection of the used microwave horn was studied by Marian Rockenhäuser [57] with the use of a network analyzer. Low reflections mean the power is radiated from the horn and not reflected back, making low reflection rates desirable (Figure from [57]). **(b)** The frequencies and dipole transition elements for transitions between $n'D$ and nF for different n'. The orange area marks transitions which are reachable by the microwave setup. **(c)** Maximum dipole transition moment d_{max} reachable for $n'D \rightarrow nF$ transitions for varying principal quantum number n of the target nF state. The principal quantum numbers in the red areas are not reachable by the used microwave horn. The principal quantum numbers n' of the initial $n'D$ states are given by the blue numbers above the respective areas. The maximum dipole transition moment d_{max} shows jumps to lower values at the principal quantum numbers where the more favorable transition moves outside the microwave spectrum and a transition with a larger difference of the initial n and the target n must be used.

about the polarization of the applied RF field.

4.2 Characterization of the F state

The initial state for the adiabatic rapid passage circularization method (see. Sec. 2.4) is the $F, m_l = 2$ or $F, m_l = 3$ state of the same principal quantum number as the desired circular state. Therefore it is of high interest to understand the influences of electric and magnetic field onto the F state and its behavior under state selective field ionization and Stark switching. In this chapter we will first discuss the methods used to produce an F state of almost arbitrary principal quantum number and later the influences of magnetic fields and electric fields onto the ionization signal and the lifetime of the F state. For that, theoretical and experimental results will be discussed.

4.2.1 Reachability

To excite nF states, an off-resonant three-photon scheme (see Sec. 3.3), involving two laser photons at 420 nm and 1020 nm and a microwave photon is applied. This scheme is depicted in Fig. 5a. With the two laser photons, nD states for a principal quantum number between $n = 20$ and $n = 180$ can be well reached, ultimately limited by the stray electric fields. However, the microwave transition is strongly limited by the bandwidth of the used microwave horn shown in Fig. 4a. In this measurement by Rockenhäuser [57], the back reflection of the used microwave

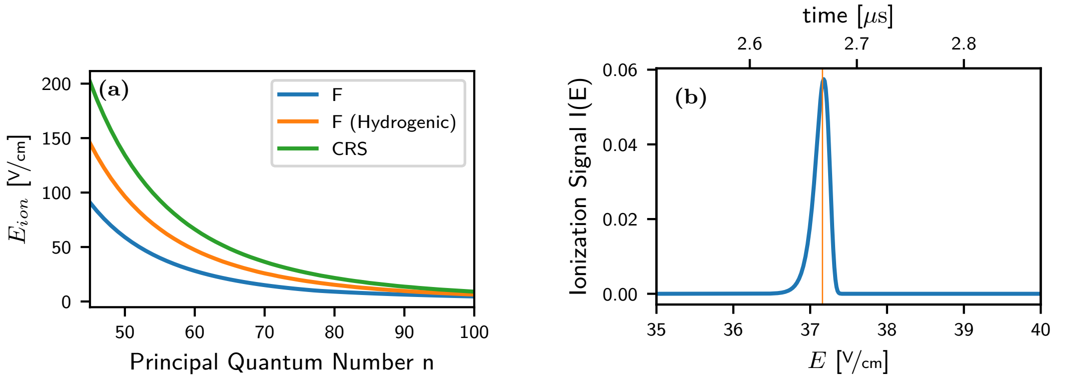

Figure 5: (a) Ionization threshold fields for ramped field ionization of the F state calculated by Eq. (2.22) and F state calculated by Eq. (2.19) for different principal quantum numbers n. The former includes the quantum defect, which leads to a much earlier ionization due to avoided crossings at the Inglis-Teller limit. The latter describes a hydrogenic ionization behavior where the ionization occurs at much higher fields (see also Fig. 7a and Fig. 7b). The cirular Rydberg state ionizes at around twice the field of the diabatic F state ionization field. **(b)** Broadening of the ionization signal due to the finite slew rate of the ionization ramp for the $56F$ state. The orange line indicates the ionization threshold voltage.

horn dependent on the applied signal frequency was measured. The power of the applied signal was 0 dBm. A high back reflection indicates that the power is not radiated from the horn but reflected back to the microwave synthesizer, making a low back reflection rate desirable. This limits the microwave horn to a usable frequency range of 21 GHz to 38 GHz and thereby the principal quantum number of the reachable nF states. Due to the quantum defect the $(n+1)D$ lies energetically lower than the nF state. As a result they are both energetically between the hydrogenic manifolds with principal quantum number $(n-1)$ and n (see Fig. 6a). Caused by the close proximity of these two states, the dipole transition moment of this transition is much larger than for other transitions $n'D \rightarrow nF$ with $n' \neq (n+1)$. Using only this transition, as was done in previous experiments, the possible principal quantum number n for F states is limited by the limited frequency range of the microwave horn to $38 < n < 46$. By using a $(n+2)D \rightarrow nF$ transition we can expand the number of reachable principal quantum numbers. As it is clear from Fig. 4b, this comes with a trade off in the size of the transition dipole transition element. However, as there is no other F state between the $(n+2)D$ state and the nF state this is compensated by the increasing dipole moment with increasing quantum number $d \propto n^2$. Thus it is possible to excite nF states with principal quantum numbers $48 < n < 58$ without a loss in transition strength compared to the previously used $(n+1)D \rightarrow nF$ transition for lower principal quantum numbers as can be seen in Fig. 4c.

Now it is imaginable that this can be carried further to $n'D \rightarrow nF$ transitions with $\Delta n = n' - n > 2$, yet it is obvious from Fig. 4c that this is not the case since the dipole moment decreases drastically for $\Delta n > 2$. This can be understood by taking into account that the nF state is not adjacent to the $n'D$ state anymore but other $n''F$ states lie in between the two. With that, the $n'D$ state couples strongly to these $n''F$ states and not to the desired nF state anymore. For example the $105D \rightarrow 100F$ transition exhibits a transition dipole moment of only 17 % of the $60D \rightarrow 58F$ transition. In principle this decrease in dipole moment could be compensated by a higher power of the microwave, however by increasing the microwave's power the ac-Stark shift is also drastically increased, disrupting states with high principal quantum numbers and inducing mixing with the states of the hydrogenic manifold and other surrounding states. The $100F$ state crosses into the hydrogenic manifold already at an Inglis-Teller limit of 6 mV/cm. At the typically used powers for

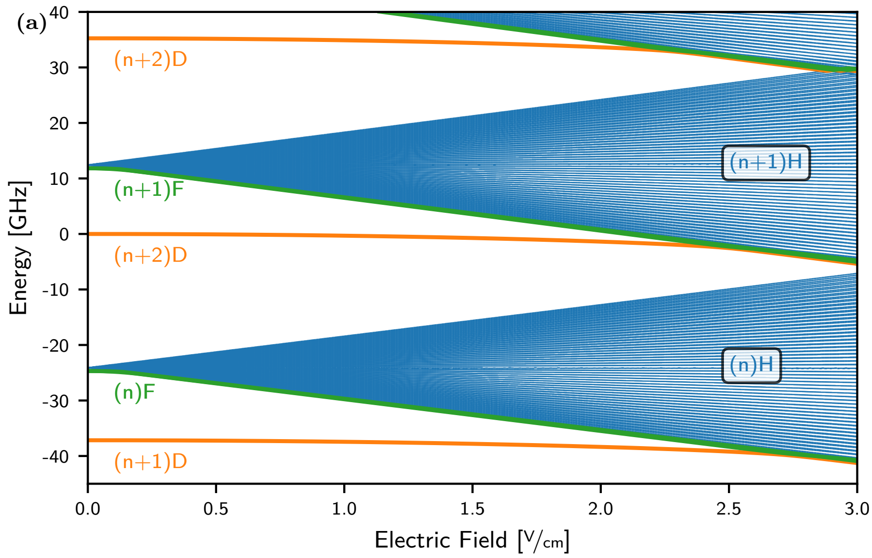

Figure 6: Energetic vicinity of the F state for $n = 56$ in the electric field. The nF state is close to the nH hydrogenic manifold due to its low quantum defect. The $(n+1)D$ is the closest D state. Due to its large quantum defect it is below the nF state. To higher energies, the nF state is adjacent to the $(n+2)D$ state.

the excitation of the $56F$ state, the microwave produces an electric field on the order of $10\,\mathrm{mV/cm}$ [57], leaving no margin for increasing the power when dealing with states with large principal quantum number. Another possible solution is to not use an off-resonant three-photon scheme, but a two photon excitation to the $n'D$ state and a microwave $\pi/2$ pulse to move the population to the nF state. By this method, much less microwave power is needed for the same Rabi frequency.

4.2.2 Field Ionization

In this section, the behavior of the F state under state selective field ionization (SSFI) is investigated. For that, we find that the $F, m_l = 3$ level ionizes differently from the other m_l levels.

The ionization rate $\Gamma(E)$ for the F state can be calculated by the method of Chaudhuri et al. [8] (Eq. 2.22) which takes the finite quantum defect into account. For ionization we typically apply the ionization field for times of the order of $1\,\mu$s, therefore it is save to assume that the atom is surely ionized if the ionization rate reaches a rate of $\Gamma(E_{ion}) = 10^8 s^{-1}$. The electric field leading to this rate is called the threshold field in the following and is shown for different principal quantum numbers n in Fig. 5a.

For a constant ionization field this consideration is enough since we do not extract any information on the exact moment of the states ionization. However, the idea of a ramped field ionization scheme is to resolve the time of ionization and map it onto the electric field at that moment in time. As the ionization rate rises in a finite time, ionization happens over a finite length of the ionization ramp, leading to a broadening of the ion signal. To estimate this broadening we consider a ramp of the electric field starting at $E = 0\,\mathrm{V/cm}$ with a slew rate of η_r

$$E_{ramp}(t) = \eta_r t. \tag{4.4}$$

In a constant electric field, the state ionizes in an exponential decay,

$$P(t) = \exp(-\Gamma(E)t). \tag{4.5}$$

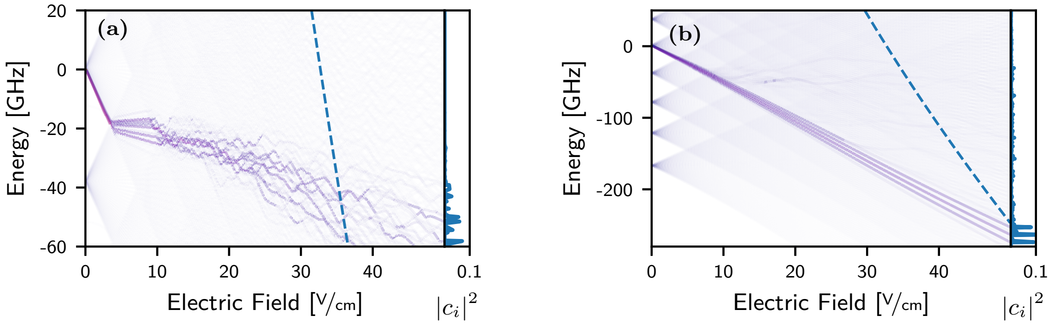

Figure 7: The state distribution dependent on the applied electric field across the Stark map for an electric field ramp with a slew rate of $\eta_r = 1.4 \cdot 10^7\,\mathrm{V/cm{\cdot}s}$. The blue line indicates the classical ionization limit. The degeneracy of the m_l levels is lifted by a magnetic field $B = 15\,\mathrm{G}$ applied in parallel to the electric field. The two different initial states **(a)** $56F, m_l = 2$ and **(b)** $56F, ml = 3$ show significantly different behavior at the Inglis-Teller limit. Due to coupling to states with high quantum defect, the $m_l = 2$ state forms avoided crossings when crossing into the lower hydrogenic manifold, which are partially followed adiabatically. This causes a much lower ionization threshold field for $m_l = 2$ states than for $m_l = 3$ states.

For the time dependent rate $\Gamma(t, E)$ of the ramped electrical field, the exponent of Eq. 4.5 can be expressed by the integral over the ionization rate to obtain

$$P(t) = \exp\left(-\int_0^t \Gamma(t', E)\mathrm{d}t'\right). \tag{4.6}$$

The derivative

$$I(t) = \frac{\mathrm{d}P(t)}{\mathrm{d}t} = \Gamma(t, E)\exp\left(-\int_0^t \Gamma(t', E)\mathrm{d}t'\right) \tag{4.7}$$

gives the time resolved change in population and thereby the ion signal. Eq. (4.7) is plotted in Fig. 5b for the $56F$ state with a ramp to $140\,\mathrm{V/cm}$[2] in $10\,\mu\mathrm{s}$, translating to a slew rate of $\eta_r = 1.39 \cdot 10^7\,\mathrm{V/cm{\cdot}s}$. These are the typical parameters used in the measurements. We find that the broadening is $17\,\mathrm{ns}$ (FWHM), which is negligible compared to the signal broadening we expect from the finite size of the atomic sample which is on the order of $100\,\mathrm{ns}$ if we assume an atomic sample of $10\,\mu\mathrm{m}$ size.

We conclude, that this broadening mechanism does not influence the measurements and that the previously calculated threshold voltage (orange line in Fig. 5b) is also valid for the case of a ramped field ionization scheme.

While the above calculation does give us an electric field value where the ionization process can be expected, it does not take into account any dynamics occurring during the electric field ramp until this ionization threshold is reached. As can be seen for example in Fig. 7a, the dynamics of the initial state across the crossings with the adjacent hydrogenic manifolds is highly non-trivial and strongly dependent on the m_l of the starting state.

To calculate the dynamics, the von Neumann equation (Eq. (2.33)) can be solved numerically for the Hamiltonian

$$H = H_A + H_B + H_E(t), \tag{4.8}$$

where H_A is the bare atomic Hamiltonian, and H_B comprises the interaction with the applied magnetic field. The interaction with the electric field, given by the ionization ramp, is described

---

[2] This translates to a voltage of $390\,\mathrm{V}$ applied to the field plates.

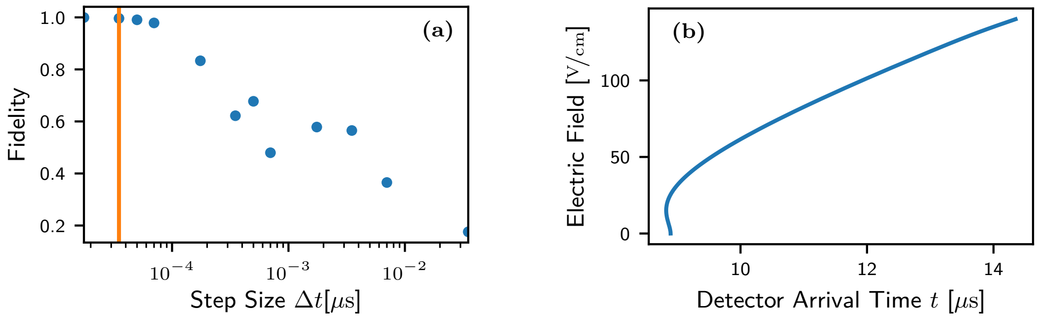

Figure 8: (a) Fidelity of the final state of a dynamical Stark map calculations for different step sizes. The reference state is calculated with a step size of $\Delta t = 3.5 \cdot 10^{-6}\,\mu$s. The orange line marks a step size of $\Delta t = 3.5 \cdot 10^{-5}\,\mu$s which is typically used in the simulation, yielding a typical fidelity of ≈ 0.99. **(b)** Mapping of the arrival time of an ion at the MCP detector onto the ionization field where it was created. The mapping is calculated by a `SIMION` [65] simulation, which takes into account the complete geometry of the science chamber (see Fig. 3) for the typically used ionization ramp to a field of 140 V/cmin $10\,\mu$s. The ramp starts at $t = 0$ at 0 V/cm. Ions created at very low fields < 15 V/cm can be overtaken by ions created at higher fields, arriving at the detector earlier or at the same time. This makes it impossible to resolve the ionization field of ions created at < 30 V/cm.

by

$$H_E(t) = d\eta_r t. \tag{4.9}$$

Generally, the integrated form of the von Neumann equation (Eq. (2.33)) is only valid for a time independent Hamiltonian. To account for the time dependence of the field ramp, the von Neumann equation can be generalized to a time-dependent operator form [38]

$$\rho(t) = U(t) \cdot \rho(0), \tag{4.10}$$

with a unitary operator $U(t)$. The evolution operator $U(t)$ can be expressed by a Magnus expansion [4]

$$U(t) = \exp\left(-i\sum_{n=1}^{\infty}\Omega_n(t,t_0)\right) \quad \text{with} \quad \Omega_1(t,t_0) = \int_{t_0}^{t} H(t')\mathrm{d}t'. \tag{4.11}$$

To solve the time evolution of $\rho(t)$ numerically, the problem must be defined on discrete points in time, at which Eq.(4.10) is evaluated. The discrete time points t_n are chosen to be equally spaced by time steps $\Delta t = t_{n+1} - t_n$. Since the dynamics is fully Markovian, the previous result of the previous time step can be directly used to calculate the next time step

$$\rho(t_{n+1}) = \exp(-i\sum_{n=1}^{\infty}\Omega_n(t_{n+1},t_n)) \cdot \rho(t_n)). \tag{4.12}$$

It can be shown for the special case of the field ramp of Eq. 4.9, that already the second term of the Magnus expansion (Eq. 4.11) $\Omega_2(t_{t+1}, t_n)$ is proportional to Δt^3. Therefore we can neglect the higher order terms if we choose the step size Δt small enough in the numerical calculations. The first order term of the Magnus expansion $\Omega_1(t_{n+1}, t_n)$ can be rewritten in the limit of small step sizes $\Delta t \to 0$ by approximating the integral by the left Riemann sum

$$\Omega_1(t, t_0) \approx H(t_0)(t - t_0). \tag{4.13}$$

By combining this result with Eq. (4.11) and (4.10), the time independent von Neumann equation of (2.33) is recovered. This equation is straightforward and relatively cheap to solve computationally ($\mathcal{O}(n^3)$ [47]). A reasonable time step size Δt is found by calculating the fidelity

$$F(a,b) = |\langle \rho_a | \rho_b \rangle|^2 \tag{4.14}$$

of the final state ρ_b. The reference state ρ_a is calculated by choosing a much smaller step size of $\Delta t = 3.5 \cdot 10^{-6}\,\mu\text{s}$. In Fig. 8a the fidelity is shown for different step sizes. For the step size $\Delta t = 3.5 \cdot 10^{-5}\,\mu\text{s}$ used in all numerical calculations, if not stated otherwise, the fidelity is $F > 0.99$. This step size combines a sufficient accuracy with a reasonable calculation time. For 500 basis states, the simulation takes approximately one hour on a low class main frame machine (`Intel Xeon W-2155`). A large speedup could be achived by porting the simulation from the currently used `MATLAB` program to a compiled language. This would make it possible to calculate the dynamics for a system with non-parallel magnetic and electric field, since for this problem more basis states must be considered. Further, the accuracy of the obtained result could be further increased by considering states of more principal quantum numbers n'. For the current calculations, states with principal quantum numbers $n-5 < n' < n+5$, where n is the principal quantum number of the state of interest, were considered.

In Fig. 7a the state evolution, calculated by the `MATLAB` von Neumann simulation, of the $56F, m_l = 2$ state during an electric field ramp with a slew rate of $1.4\,\mathrm{V/cm{\cdot}s}$ is shown. The different m_l levels are split by a magnetic field of $B = 15\,\mathrm{G}$ in the Paschen-Back regime. The population evolves mostly adiabatically along the $n = 56$ hydrogenic manifold. However, at the Inglis-Teller limit, where the $n = 55$ hydrogenic manifold crosses with the $n = 56$ hydrogenic manifold, avoided crossings due to the quantum defect arise. The strength of the avoided crossings are given by the quantum defect and are on the order of a few MHz for the $n = 56, m_l = 2$ state, which means they are typically crossed not purely adiabatically or diabatically but a mixture of both, spreading the population over multiple states. Most of the population is transferred to the energetically higher lying blue states of the lower hydrogenic manifold. The state then reaches the classical ionization limit (dashed blue line) at around $35\,\mathrm{V/cm}$, which is in good agreement with the predictions of Chaudhuri et al. [8] (Eq. (2.22)) of $37.1\,\mathrm{V/cm}$.

The ionization of the $56F, m_l = 3$ state is qualitatively different from the ionization of the $56F, m_l = 2$ state as can be seen in Fig. 7b. The avoided crossings at the Inglis-Teller limit are not crossed in a partially adiabatic way as for the $m_l = 2$ state. This can be explained by the fact that for the Stark states m_l is a good quantum number but L not anymore. In the finite electric field, the F state starts mixing with states of the same m_l but with different l. This means, that the $F, m_l = 2$ state mixes with the $D, m_l = 2$ state which has a large quantum defect. This is not the case for the $F, m_l = 3$ state, as there is no D state with $m_l = 3$. The quantum defect of the F state is two orders of magnitude smaller than the quantum defect of a D state (see Tab. 2), which causes the avoided crossings at the Inglis-Teller limit to be two orders of magnitude smaller for the $m_l = 3$ crossings. This causes the $F, m_l = 3$ state to populate more red-shifted states with a larger ionization threshold field at around $60\,\mathrm{V/cm}$. In fact, this result is in good agreement with the predictions of Damburg and Kolosov $61.9\,\mathrm{V/cm}$ for the $56F$ state.

In Fig. 9a the measured ion signal of the $56F, m_l = 2$ state, obtained by a SSFI measurement is shown. The electric field is ramped up to $140\,\mathrm{V/cm}$ in $10\,\mu\text{s}$. The arrival time of the created ions at the MCP detector can then be mapped onto the times of their creation and thereby the ionization field. The mapping is obtained from a `SIMION` [65] (see Fig. 8b) simulation of the ion trajectory under the influence of the field ramp to account for the geometry of the experiment chamber. The orange bar shows the ionization threshold calculated by the method off Chaudhuri et al. [8] (Eq. (2.22)). The calculated value fits well to the measured data. Further, the peak

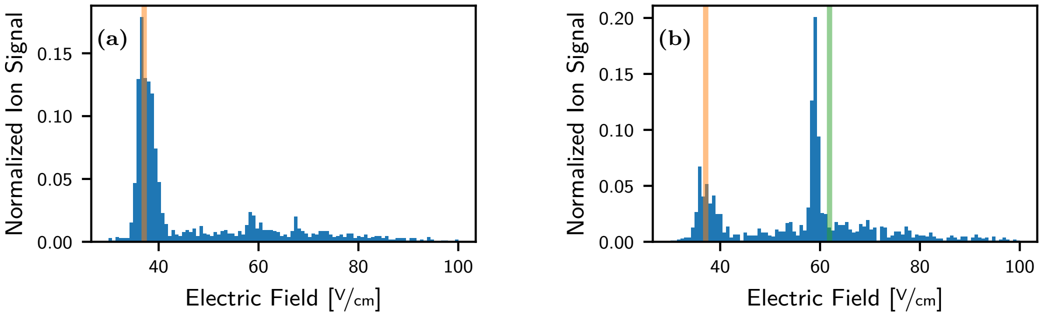

Figure 9: Ionization signal of the $56F, m_l = 2$ **(a)** and the $56F, m_l = 3$ **(b)** state. The orange line is the ionization threshold field calculated by the method of Eq. 2.22, the green line is the ionization threshold field for the $56F, m_l = 3$ state calculated by the method of Damburg and Kolosov (Eq. (2.19)).

shows a FWHM of approximately 5 V/cm which compares well to the spreading observed in the von Neumann simulations at the classical ionization limit (see Fig. 7a).

A similar measurement of the $56F, m_l = 3$ state (Fig. 9b) shows that the theory based on the quantum defect (Eq. (2.22)) does not fit to the ionization of $m_l = 3$ states. As expected from the von Neumann simulations, the $F, m_l = 3$ state ionizes in a hydrogenic way, where it crosses with the classical ionization threshold at a much higher electrical field (see Fig. 7b). However, there is still a residual peak from diabatic ionization at ≈ 37 V/cm which has a much larger contribution to the ion count than expected from the simulation. This is due to the fact that the magnetic field and the electric field is not perfectly parallel in the experiment. This will be discussed further in the next section 4.2.3.

Since the state ionizes in a hydrogenic manner, the theory of Damburg and Kolosov can be applied for calculating the threshold. As can be seen by the green bar at 61.9 V/cm in Fig. 9b, this ansatz fits reasonably well to the measured data. The measured signal is always at sightly lower ionization fields than the theoretical values. This could either be attributed to the small but finite quantum defect of the F-state of $\delta_1 = 0.01654$ [28], altering the ionization behavior or a slight mismatch of the `SIMION` [65] mapping and the experiment.

4.2.3 Lifetime and Ionization Measurements

Previous experiments employing the adiabatic rapid passage circularization method [49, 66] were conducted in a cryogenic environment, this makes the effects of black-body radiation onto the lifetime of the Rydberg states negligible. Since our experiment is not cryogenic we need to take these effects into account. In this section this problem and the influence of other environmental radiation onto the circular state and the starting F state will be addressed.

The theoretical natural lifetime obtained from Numerov calculations of the $58F$ wavefunction is 122 μs which is much longer than the timescale of typically 20 μs used for the adiabatic rapid passage. If the influence of black-body radiation is included, the life time decreases to 84 μs, which is still enough for the ARP. However, the experimental values measured in this thesis show a large deviation from this value and are much lower than expected. To obtain the lifetime information experimentally, we again apply state selective field ionization (SSFI) after the Rydberg F state is created by the off-resonant three-photon scheme (Sec. 3.3). The time in between excitation and ionization τ is then varied (see. Fig. 10a).

In Fig. 11a, the SSFI signal is plotted against the wait time τ for the $56F, m_l = 2$ state. An electric field ramp from 0 V/cm to 140 V/cm in 10 μs is used to ionize the excited Rydberg states.

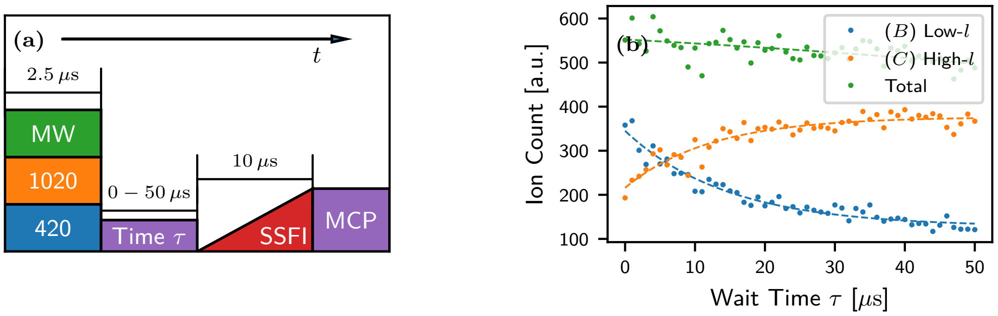

Figure 10: (a) Schematic of the experiment sequence for measuring the life time of the Rydberg F states. The F state is exited in a three-photon process and then measured by a ramped state selective field ionization sequence after a wait time of τ. The Rydberg excitation process is typically $2.5\,\mu$s long. **(b)** Comparison of the different ionization features of the $56F, m_L = 2$ state (cf. Fig. 11a) for different wait times τ. While the total ion signal stays approximately constant, the low-l states (feature B) decay to high-l states (feature C). The lines are exponential fits to the data and serve as guides to the eye.

The most prominent signal is measured for an ionization field between $\approx 32\,\mathrm{V/cm}$ and $\approx 38\,\mathrm{V/cm}$ (feature B). At first glance, this seems to fit well with the theoretical prediction of $37.1\,\mathrm{V/cm}$. However, by looking closer at this peak, a short-time dynamics can be observed (inset). By calculating the mean of the histogram of the ionization peak B (green dots), we find that for very short wait times the peak appears to be indeed close to the theoretical prediction of $37.1\,\mathrm{V/cm}$. However it then quickly shifts to lower ionization voltages of $35\,\mathrm{V/cm}$ for wait times $\tau > 5\,\mu$s, from where it does not shift any further. This implies that in this first period of time, the excited F state rapidly decays to another, more stable state with a lower ionization threshold field. Since this means that the state decays to a higher Rydberg state, it stands to reason that this decay is caused by black-body radiation or other resonant, unintentional radiation. The target state of this decay process has an ionization threshold fitting to the theoretical predictions (blue dashed line) and the measurements of the $58D$ state (see. Fig. 11b). This implies that the $56F$ state is driven back to the $58D$ or another state in its vicinity. In the ionization trace measurement (Fig. 11a), besides the signal B, there is also a signal visible at much lower ionization fields A. This peak can be contributed to prompt ions, created before the ionization and will be discussed in detail in paragraph 4.2.3. Further, a large, widespread signal can be measured for ionization fields between $60\,\mathrm{V/cm}$ and $90\,\mathrm{V/cm}$ (Feature C). By comparing this range to the theory of Damburg and Kolosov, it is obvious that this signal is caused by high-l states of the $n = 56$ hydrogenic manifold which ionize in a hydrogenic way. The state with the lowest ionization voltage which ionizes in a hydrogenic way is the $56F, m_l = 3$ state as observed in Fig. 9b, with a threshold field of $61.9\,\mathrm{V/cm}$ (green dashed line in Fig. 11a). The circular state serves as the upper limit at $86.8\,\mathrm{V/cm}$. The fact that those states are populated either during the excitation or the ionization ramp indicates that an unwanted mixing of the different m_l levels takes place.

To understand the formation of this hump in the ionization signal, the dynamics between the front peaks (A and B) and the hump (C) is investigated. Fig 10b shows the ion signal integrated over the different areas of the ionization trace. It can be seen that the low-l like ionization signal (B) decreases exponentially with increasing wait time, signalling a decay of the low-l states. However, the total ion count does only marginally decrease with the wait time. Thus the state does not decay to much deeper lying states as it would happen through spontaneous decay but to the high-l states. This manifests in an increase of the ion count rate in the high-l feature C of the

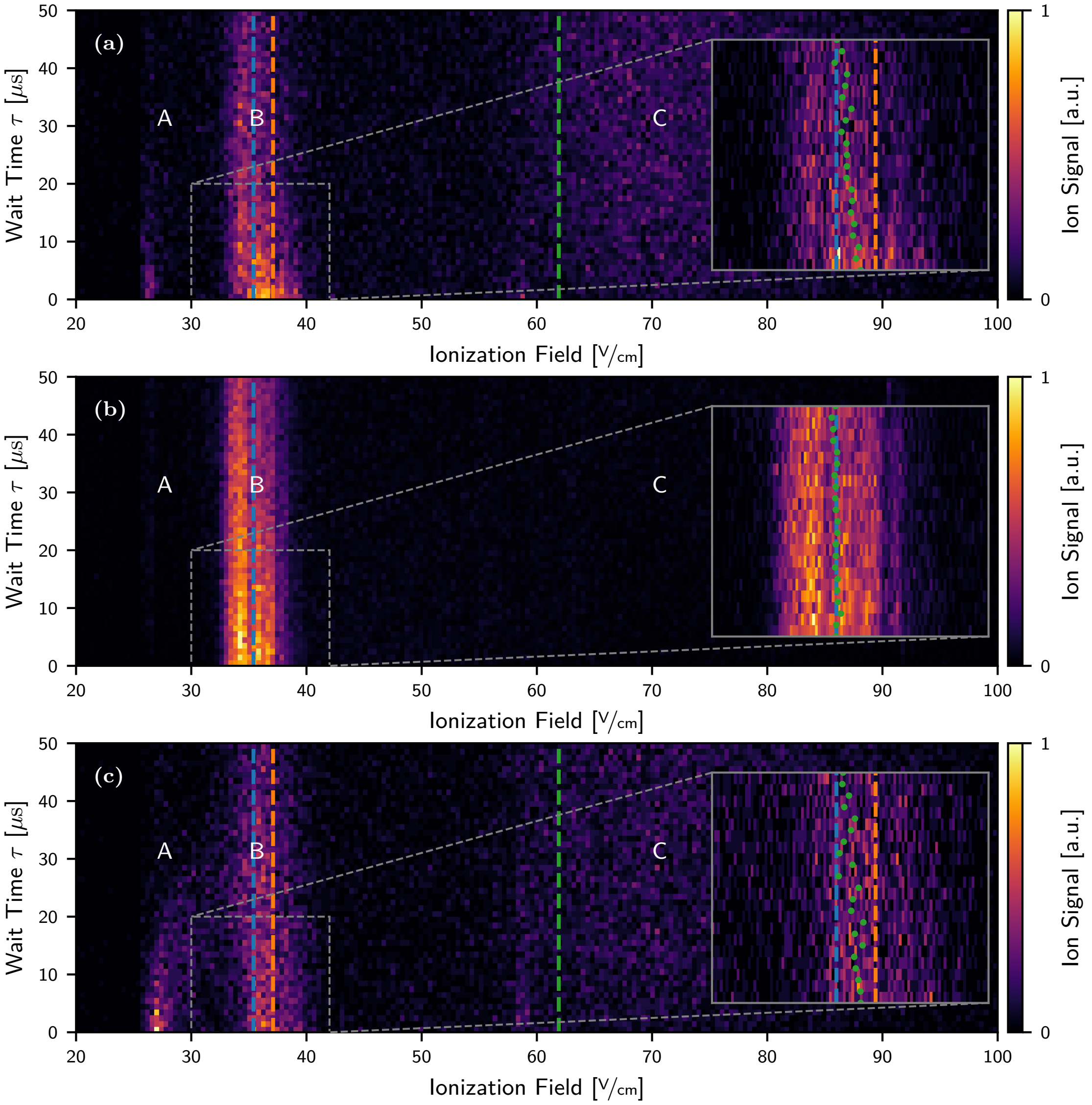

Figure 11: State selective field ionization measurements of the $56F, m_l = 2$ **(a)**/**(c)** and the $58D, m_l = 2$ **(b)** state in a magnetic field of $15\,\mathrm{G}$. The blue dashed line marks the theoretical ionization threshold of the $58D$ state, the orange dashed line the one of the $56F$ state. The green dashed line is the ionization threshold of the $56F$ state calculated by the hydrogenic theory of Damburg and Kolosov (Eq. (2.19)). The zoom-in shows the prominent ionization peak B for short wait times. The center of gravity of the signal in the zoom-in is marked by green dots. For measurement **(c)** the dipole trap is chopped off during the whole sequence for $70\,\mu\mathrm{s}$. The $56F$ state shows three prominent features. The prompt ion peak A, the peak expected from the theoretical ionization calculations B and the broad high-l like ionization feature C. The $58D$ state **(b)** shows almost only the expected peak B.

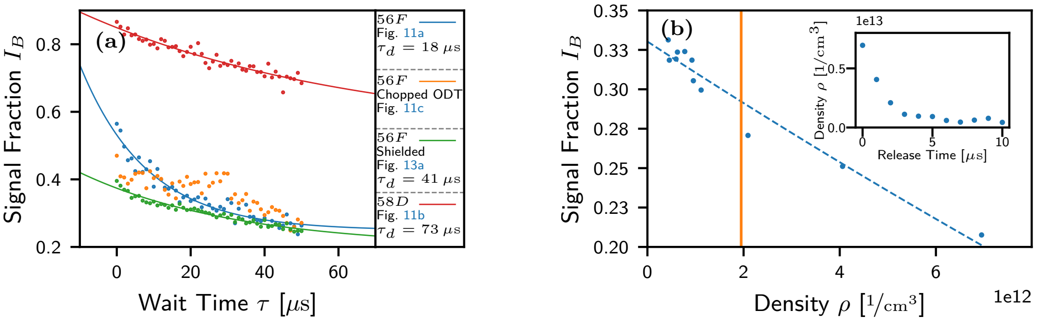

Figure 12: (a) Fraction of the ionization signal I_B in the target peak B for increasing wait times between Rydberg excitation and ionization τ. The F state does not only show a low fraction I_B right after the Rydberg excitation pulse but also exhibits a fast decay of the remaining ions into high-l states (signal feature C). Different attempts to increase the fraction I_B and the lifetime like chopping the dipole trap show negligible results. The right area displays the extracted lifetime and a reference to the figure of the corresponding ion signal of each curve. The measurement with chopped dipole trap could not be fitted reliably as a result of the large spread of the data points. **(b)** The measurement of the $56F$ state (blue in **(a)**) is repeated at $\tau = 20\,\mu$s for different densities of the atomic sample. For lower densities ρ the ion signal improves but not even for an interpolation to zero density does it reach the high values of I_B observed for the $58D$ state. The orange line marks the density of the measurements of **(a)** $1.95 \cdot 10^{12}\ ^1/_{\mathrm{cm}^3}$. The blue line is a fit of Eq. 4.20 with an additional offset parameter to the data. The inset shows the density reached for different trap release times in the release and recapture sequence before the Rydberg excitations.

spectrum. For a qualitative discussion, the ion fraction in the desired peak B

$$I_B = \frac{B}{A + B + C} \tag{4.15}$$

is investigated in the following. In the above definition, A, B and C represent the integrated signal in the corresponding area of Fig. 11a. The fraction I_B is plotted against the wait time τ as blue data in Fig. 12a along with similar measurements with different parameters which will be discussed in the paragraphs 4.2.3 to 4.2.3. By fitting an exponential function to the decay in Fig. 12a the life time of the observed process can be extracted. The obtained value of $15.5\,\mu$s is much smaller than any expected life times for the $56F$ state. It would be imaginable, that the decay happens during the finite time of the Rydberg excitation or the ionization ramp, which is not included in the value of τ. In terms of τ, the Rydberg excitation takes place from $\tau = -3\,\mu$s to $\tau = -0.5\,\mu$s. However, by extrapolating the decay process to the start of the Rydberg excitation, the fraction of the signal I_B does not rise to unity, but merely to $I_B = 0.75$. This means, that the decay is not the only process leading to the high-l portion of the ionization signal. Either a second, even faster decay takes place on time scales not resolvable in the measurements or the mixing with high-l states does happen during the ionization process. When comparing this reduced life time to the analogue measurement of the $58D, m_l = 2$ state (Fig. 11b) it gets clear that both issues are distinctive to the F state. Neither the short time dynamics[3] nor the broad high-l signal is observed for the $58D$ state. At this point it must be assumed that the atom is not in the target F state anymore after the fast decay process. As a result, the adiabatic rapid passage protocol will be of no avail. To understand and eliminate this problem, various disruptive factors are investigated in the following paragraphs 4.2.3 to 4.2.3.

---

[3] The center of gravity of the ion histogram in the inset of Fig. 11b stays constant for longer wait times

Influence of the Optical Dipole Trap

The optical dipole trap which is used to trap the cold atomic cloud (See Sec. 3.2) is made from two crossed beams following a beat frequency of 160 MHz. This approach acts in a similar way as an electric radio frequency field, by dressing the m_l levels. This could mix the F state with high-l states during the ionization ramp, where transitions into the hydrogenic manifold become resonant to the beat frequency. Further, the ponderomotive potential of the trapping lasers is known to have a similar effect on the hydrogenic manifold states. It was even proposed by Cardman et al. [7] that this phenomenon can be used as a method to generate circular Rydberg states. To rule out those phenomena as a cause for the unexpected ionization behavior and decay of the $56F$ state the influence of the dipole trap was investigated. An experimental sequence was designed where the optical dipole trap is switched off at the start of the Rydberg excitation and switched back on not until after the ionization ramp. To obtain comparable results for different wait times τ, the trap switch-off time is chosen equal for all measurements. To allow us to include the whole measurement for the highest measured wait time of $50\,\mu$s, the switch-off time is chosen to be $70\,\mu$s. During this time the atoms are not subject to the influence of the trapping beams, which means that they can freely move and especially drop down due to gravity. When switching back on the trap not all atoms can be recaptured, leading to strong atom loss. The atom loss limits the number of experiments feasible in one atomic cloud. While typically 4000 experiments are conducted per single cloud, the dipole trap chopping limits this value to 300 experiments per cloud. Additionally the density drops rapidly after only a few experiments, making the Rydberg excitation less efficient. Hence, the chopping leads to much longer data taking times to reach the desired statistics and is therefore unfavorable.

The measurement of Fig. 11a was repeated but with the dipole chopping applied in Fig. 11c. When comparing the two measurements no considerable decrease in the high-l ionization signal C can be observed, which means that the ponderomotive force does not couple to high-l states on the timescale of the ionization ramp in a significant way. Nonetheless, there seems to be a slight improvement when looking into the decay dynamics. As can be seen in Fig. 12a, the fraction of the ion signal in the low-l peak I_B starts at lower values but does not drop as fast as without the chopped dipole trap. Due to the heavy spreading of the data points however no qualitative improvement of the life time can be extracted. It is also not clear if this supposed improvement can be attributed to the chopping, since the density varies strongly during the measurement due to the release and recapture effect of the chopping. It is not possible to untangle the two effects easily. Since the density does indeed influence I_B, as will be discussed in paragraph 4.2.3, the density variation is also a probable cause for the spreading of the data points in Fig. 12a. Further, in this measurement the second peak (A) at low ionization voltages at $\approx 27\,\mathrm{V/cm}$ appears to be more prominent compared to the non-chopped measurement. As it turns out, this peak is caused by prompt ions. Possible causes for the creation of the prompt ions will be discussed in paragraph 4.2.3.

We can conclude that the dipole trap may have a small impact onto the rate of the observed decay but is not the main cause for the large high-l character in the ionization signal and also not the main cause for the rapid decay from the low-l to the high-l states. We will therefore abandon the dipole trap chopping for the further measurements since it introduces much longer measuring times.

Influence of External Radio Fields

As discussed earlier, the dynamics of the decay happens on a short timescale and high-l states are populated by the process. One explanation for this occurrence could be radiation, resonant to the $nF \rightarrow nG$ transition. A reduction in lifetime of a Rydberg S state caused by external, resonant radio frequency fields was also observed by Archimi et al. [2]. For $n = 56$ and an

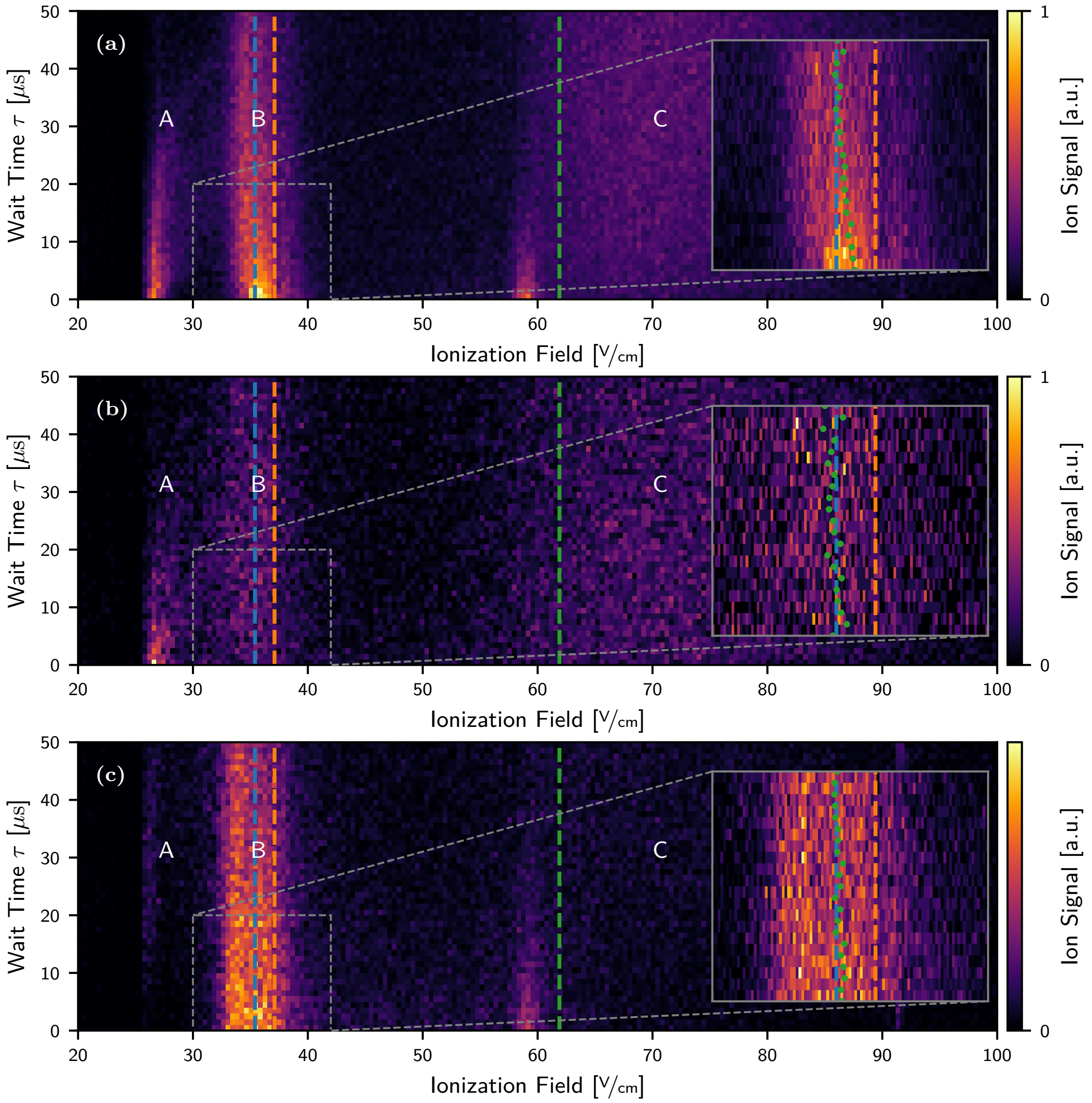

Figure 13: State selective field ionization measurements of the $56F, m_l = 2$ state in a magnetic field of $5\,\mathrm{G}$ similar to the measurement of 11a. Due to the reduced magnetic field compared to Fig. 11a, the angle between magnetic and electric field is larger, causing the signal at $\approx 60\,\mathrm{V/cm}$ to be more prominent. The experiment was shielded by aluminum foil to reduce parasitic radio frequencies which could drive the $56F \rightarrow 56G$ transition. Figure **(a)** includes all ion counts, whereas **(b)** only contains ions from signals where two or more ions where detected for a single Rydberg excitation cycle. In this case, the prompt ion peak A at $27\,\mathrm{V/cm}$ and the high-l hump C completely dominate over the target F-state peak B. For **(c)**, the $56F$ state was reached by a resonant two-photon scheme to the $58D$ state and a resonant microwave pulse in a magnetic field of only $5\,\mathrm{G}$. The ionization trace shows similar features as in the case of the three-photon scheme. However, the high-l part C is significantly lower. The presence of the high-l peak at 60 V/cm, caused by the angle between magnetic and electric field is an indicator that the F-state is populated well by the excitation scheme, since the D state does not exhibit this feature.

external magnetic field $B = 15\,\mathrm{G}$, the transitions from the $56F, m_l = 2$ state to the different m_l levels of the $56G$ state lie between 493 MHz and 535 MHz. It turns out, that in this frequency range multiple signals can be picked up from the environment. By connecting the electric field compensation plates directly to a spectrum analyzer, we can observe multiple frequency bands with intensities varying between $-60\,\mathrm{dBm}$ and $-90\,\mathrm{dBm}$:

- $488 - 496\,\mathrm{MHz}$
- $506 - 515\,\mathrm{MHz}$
- $529 - 537\,\mathrm{MHz}$
- $560 - 568\,\mathrm{MHz}$

We suspect that the bands are terrestrial television broadcasting signals (DVB), since this is the only signal in this range and the width of the bands of 8 MHz matches with the DVB standard [67]. Further, the DVB signal has comparably high broadcasting intensities.

If we assume that the electric RF field at the position of the atoms is comparable to the values measured on the compensation plates, the atoms would sense a field of $\approx 0.2\,\mathrm{mV/cm}$. Since the dipole transition strength between the nF and the nG state is comparably large, this field would result in a Rabi frequency on the order of 100 kHz. This timescale would correspond well to the observed decay. To overcome this problem, we wrapped the setup in aluminum foil with a thickness of $30\,\mu\mathrm{m}$. Since the skin depth of aluminum at 500 MHz is $3\,\mu\mathrm{m}$ [33], the foil shields most of the signal. A re-measurement of the RF signal on the electric field plates using the spectrum analyzer showed that all bands are damped to signal strengths below $-80\,\mathrm{dBm}$. The measurement of Fig. 11a was therefore repeated with the shielded setup and is plotted in Fig. 13a. At first glance, there seems to be no improvement. However, by investigating the decay rate by fitting an exponential function (Fig. 12a) to the fraction of the total ion signal in the target ionization peak B, a slight improvement is found. The lifetime of the process which transfers the F state to the high-l states was improved from previously $18.2\,\mu\mathrm{s}$ to $42.7\,\mu\mathrm{s}$. Still, note that the fraction of ions I_B in the desired ionization peak B for no wait time $\tau = 0$ is even worse than without the shielding. This makes it clear that the parasitic radio frequency is not the main cause for the unexpected ionization behavior. It is not clear if the improvement of the lifetime is attributable to the shielding or a different, unnoticed change in the experimental conditions, since one would expect also an improvement of the ion signal at zero wait time $\tau = 0$.

Influence of Noise

Another possible issue could arise in the ionization itself, if the noise background of the ionization ramp causes crossings to be traversed differently than expected. The high voltage amplifier used to reach the required voltage of 390 V for the ionization ramp is driven by an arbitrary waveform generator (`Keysight 33522B`). The noise background of this AWG is, according to the data sheet, $1\,\% \cdot U_{pp} + 1\,\mathrm{mV}$ [36]. The measured noise for an output of $U = 5\,\mathrm{V}$, which represents the middle of the typically used ionization ramp, is much lower at $1.5\,\mathrm{mV_{rms}}$. However, the high voltage amplifier which is an in-house development and has an amplification factor of $\chi = -39.68$, also amplifies this noise. The noise of the AWG is thereby amplified to $60\,\mathrm{mV_{rms}}$, which agrees with the measurements. It is conceivable that this noise causes some crossings to be traversed differently during the ionization ramp. However, simulating the ramp with added noise by the dynamic Stark map program described earlier does not show a significant difference to the case without noise. The noise does not play a role during the Rydberg excitation, since a switch circuit (Sec. C) is used to apply the offset field by a different source. The noise of the HV amplifier is thereby clamped out, since it would result in a broadened Rydberg line otherwise. This switch is used in all ramped field ionization measurements in this thesis except the measurements of Fig. 9a and Fig. 9b.

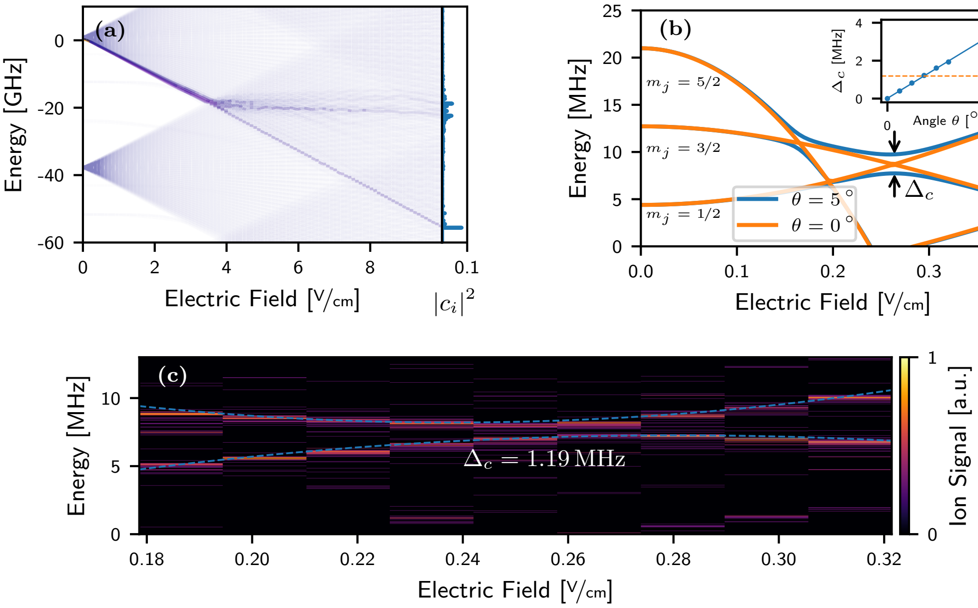

Figure 14: **(a)** Evolution of a $56F, m_l = 2$ state in the electric field of a field ramp with a slew rate of $\eta_r = 1.4 \cdot 10^7\,\mathrm{V/cm{\cdot}s}$. This represents the same situation as the calculation of Fig. 7a except that the electric field and the magnetic field are not parallel but under an angle of $5\,°$. The angle couples the levels with different m_l and creates avoided crossings. A large fraction of the population is transferred to high-l states which ionize in a hydrogenic way. **(b)** Stark map of the $58D$ state. The $m_j = 3/2$ crosses the $m_j = 1/2$ state if the magnetic field is parallel to the electric field $\theta = 0\,°$. Under a finite angle, the states couple and exhibit avoided crossings. This crossing is a good candidate to measure the angle, since it is easy to access and very sensitive as can be seen in the inset. The splitting Δ_c is calculated for discrete angles θ. The blue line is a linear fit. The orange line indicates the splitting Δ_c of the measurement in **(c)**. The measurement of the crossing at a magnetic field of $5\,\mathrm{G}$ applied in x direction **(c)** shows that the magnetic field forms an angle of $\theta = 2.9\,°$. The blue dashed lines are quadratic fits to the crossing to extract the splitting of $\Delta_c = 1.19\,\mathrm{MHz}$.

Influence of the Magnetic Field Angle

If the magnetic field and the electric field are not perfectly parallel, levels with different m_l couple. This coupling causes the formation of avoided crossings between the different m_l fans and changes the energetic structure of the hydrogenic manifold. Without the coupling, the $F, m_l = 2$ state does not couple to other states with $m_l > 2$ during the whole ionization procedure. As can be seen in Fig. 7a, it then ionizes in a low-l characteristic way. However, with a finite angle, the $F, m_l = 2$ state can mix with high-l ($m_l > 2$) states during the ionization ramp. A simulation for the same scenario as in Fig. 7a but with a $5\,°$ angle between the electric and magnetic field can be seen in Fig. 14a. This small angle already causes that a significant fraction of the population crosses into high-l states at the manifold crossing at the Inglis-Teller limit, which ionize at much larger fields. Due to the coupling of the m_j states, it is not sufficient to consider the levels of a single m_j like in the uncoupled case. In the simulation leading to Fig. 14a, states with $-1/2 < m_j < 13/2$ where considered. As no qualitative data is extracted from the simulations and the computation time is on the order of a few days, the convergence of the simulations was checked by eye by comparing the results to a simulation with only $1/2 < m_j < 11/2$ taken into account. Since much more states must be considered for the calculation, it was not carried out to the ionization limit but only to $10\,\mathrm{V/cm}$. However in Fig. 7b and 7a it was found that all of the interesting dynamics happen at the Inglis-Teller limit, which is well included in the chosen electric field range and visible in Fig. 14a.

The measurements of Fig. 13a and 13c show also a narrow peak at the low end of the high-l ionization feature C, which corresponds well to the narrow high-l distribution of the simulations of Fig. 14a. This gives strong evidence, that there is indeed a finite angle between the magnetic and electric field in the experiment. However, this does not explain the broad high-l feature C, since the angle only causes the population of a few high-l states but not the entire span of the hydrogenic manifold. Since this angle can also cause unexpected behavior for the Stark switching and the ARP protocol itself, we will further investigate this in the following.

The magnetic field angle θ can be determined experimentally by measuring the splittings of an avoided crossing between states with different m_j. A good candidate is the splitting between the $58D, m_j = 3/2$ and the $58D, m_j = 1/2$ state. As can be seen in Fig. 14b, this crossing is very sensitive to even small angles. Further, it is easily accessible in the experiment due to its position at a low electric field of 0.265 V/cm and its isolated position far from the hydrogenic manifold. The angle dependent splitting Δ_c is extracted for different angles from numerical Stark map calculations. As it turns out, the splitting grows linear for small angles θ (cf. Fig. 14b, inset). The linear fit gives a relation between the angle θ and the experimentally accessible splitting Δ_c. Fig. 14c shows a measurement of this crossing, with the same magnetic field in x direction of 5 G as in the calculations. By fitting two quadratic functions to the crossing, the splitting can be extracted to be 1.19 MHz. Hence, the angle between the magnetic field and the electric field is $\theta = 2.9\,^{\circ}$.

To compensate this misalignment, an opposing field must be applied. To obtain the needed strength of this field, a magnetic field is applied in the x direction and the magnetic field in the other directions y and z is varied until the splitting vanishes. As it turned out, the compensation point is not reachable with the current experimental setup. As the coils to create the magnetic field are driven by unipolar current supplies, a magnetic field can only be applied in one direction along a given axis. However, the compensation value lies in the other, non-reachable direction in z direction. It is not an option to reverse the field by reversing the unipolar current supply used to drive the coils, since the magnetic offset coils are also needed in the loading sequence of the dipole trap. There, a reversal of the field would lead to a much lower loading efficiency. To circumvent this problem, a switch (see Sec. B) can be used to reverse the field after the loading of the dipole trap. Unfortunately, only one of these switches was available at the time of this thesis, and needed to align the field in x direction. It is also not clear at this point if the angle is caused by a stray field, like the earth magnetic field, or by a misalignment of the coils itself. It is to be assumed however that both play a role, as the theoretical angle caused by the earth magnetic field is much larger than the measured angle. The south-north component is the largest contribution of the earth magnetic field in Stuttgart (48 ° North, 9 ° East), which is however not of interest, since the x-axis of the experiment is aligned along this axis. The disruptive component is the vertical component, along the experiment z axis which is 0.43 G [70]. This would cause an angle of

$$\theta = \arctan\left(\frac{B_z}{B_x}\right) = \arctan\left(\frac{0.43\,\mathrm{G}}{5G}\right) = 4.9\,^{\circ}. \tag{4.16}$$

To distinguish between a misalignment of the fields caused by a misalignment of the coils itself and a misalignment caused by stray fields, the measurement could be repeated at different magnetic field strengths in x direction. The latter causes compensation fields which are independent of the magnetic field in x direction, whereas the former would cause a dependence of the compensation fields on the magnetic field strength in x direction.

Influence of Collisions

In the previous investigations we mainly focused on the creation of the high-l signal C. In this paragraph the creation of the feature A will be investigated. It turns out that this feature is caused by prompt ions, which are created before the ionization sequence. This was confirmed by an ion extraction measurements, where an electric field pulse of $14\,{}^{\mathrm{V}}\!/\!{}_{\mathrm{cm}}$, well below the ionization limit, is used to extract ions from the science chamber and accelerate onto the detector without ionizing the Rydberg states. The creation of prompt ions A in collisions and the connection to the high-l feature C will be discussed in the following.

A possible cause for the large high-l ionization signal C could be the occurrence of l-changing collisions with ground state atoms [62]. The rate [23]

$$\Gamma = \rho \sigma v \tag{4.17}$$

of this two-body collision can be roughly estimated by assuming that every ground state atom within the Rydberg orbit with radius r_B is scattered, by approximating the cross section as

$$\sigma = 4\pi r_R^2 = 16\pi a_0^2 n^4. \tag{4.18}$$

The average relative velocity between the Rydberg and the ground state atom v is given by [23]

$$v = \sqrt{\frac{16 k_B T}{\pi m}}, \tag{4.19}$$

with k_B being the Boltzmann constant and $m = 1.443 \cdot 10^{-25}\,\mathrm{kg}$ [68] the mass of rubidium 87. By applying Eq. (4.17) the collision rate can be calculated for the density used in the measurements of $\rho = 1.95 \cdot 10^{12}\,{}^{1}\!/\!{}_{\mathrm{cm}^3}$. This yields a collision rate of $0.060\,{}^{1}\!/\!{}_{\mu\mathrm{s}}$ and translates to a lifetime of $16.7\,\mu\mathrm{s}$, which agrees well with the measured lifetime of $15.5\,\mu\mathrm{s}$. By studying the influence of the density in the atomic sample onto the measured ion signal experimentally and comparing it to the theoretical fraction

$$I_B = \exp\left(\Gamma t\right) = \exp\left(-\rho\sigma v t\right) \tag{4.20}$$

obtained from Eq. (4.17), it can be investigated if the good agreement persists or if it is only a coincidence. The density in the optical dipole trap is controlled, by starting from a dense sample of $7 \cdot 10^{12}\,{}^{1}\!/\!{}_{\mathrm{cm}^3}$ and shutting off the dipole trap for a short variable time in a release and recapture sequence. During this off time, atoms can move out of the trap volume and thereby decrease the density after the release time. The density [37]

$$\rho = N\omega_x\omega_y\omega_z \left(\frac{m}{2\pi k_B T}\right)^{3/2} \tag{4.21}$$

can be calculated from the temperature T of the atomic cloud and the atom number N, which can both be obtained from absorption imaging. The trap frequencies ω_i of the optical dipole trap are listed in Sec. 3.2. This allows us to calculate a mapping of the density of the sample ρ onto the dipole trap release time, found in the inset of Fig. 12b.

The measurement of the signal fraction in the target state B (Fig. 12b) was carried out after a wait time of $20\,\mu\mathrm{s}$. It can be seen that the signal decreases for increasing densities, confirming that high densities are an considerable influence onto the decay rate of the $56F$ state. However the signal fraction I_B does not reach unity when interpolating to zero density $\rho = 0$. By fitting Eq. (4.20) to the data with σ and an additional offset as free parameters, the value $I_B(\rho = 0) = 0.34$ can be obtained. The cross section obtained from this fit $\sigma = 0.637 \cdot 10^{-12}\,\mathrm{m}^2$ is a factor of 2.17 smaller than the calculated value from Eq. (4.18) $\sigma_{th} = 1.38 \cdot 10^{-12}\,\mathrm{m}^2$. When taking into account that Eq. (4.18) only gives an upper limit, this fits reasonably well and confirms that two body collisions are the reason for the observed decay process. However, the low value of $I_B(\rho = 0)$ can not be explained by these collisions, especially when it is taken into account, that the density is slightly overestimated. This is because it is measured at the beginning of the experiment. During the 4000 consecutive Rydberg excitation and ionization cycles, the density starts to decrease due to atom loss. This means, that also the value of the signal fraction I_B at zero density $\rho = 0$ is slightly overestimated. It would be imaginable that an additional collision process occurs that is saturated across the small measured density range of only one order of magnitude and can therefore not be resolved.

A suspect for such collisions those between the Rydberg atom and ions. Such l-changing collisions where observed by Walz-Flannigan et al. [73] between Rydberg atoms and charges. This mechanism where a passing charge deforms the wave function, introducing high-l character could also be possible for the interaction with positive ions. A hint in this direction can be found by re-evaluating the data of the measurement of Fig. 13a but only taking into account ion detection events where two ions where detected for a single experimental sequence. It can be observed, that the prompt ion peak A and the high-l signal C are much more prominent and the target ionization peak B only barely visible. Also, the peak slightly below 60 V/cm, caused by the angle between magnetic and electric field vanishes completely. Where for all ion signals taken into account (Fig. 13a), the fraction I_B is $I_B(\tau = 0) = 0.60$, it drops to only $I_B(\tau = 0) = 0.36$ for the double count measurement (Fig. 13b). This implies, that in the cases where a prompt ion is created, the F state is disturbed and obtains an high-l character. It is imaginable that a Rydberg atom is created and then ionized by a multi photon process of the Rydberg laser or the trapping laser, after which a second Rydberg F state could be excited, which is then in return disturbed by the first ion passing through its orbit. In the experiment, we find around 3 % double counts, which is much lower than the ion counts in the alleged collision signals A and C. However, it is not clear how good the detection efficiency is for double counts. For single counts, the detection efficiency was measured to be $\eta = 0.4$ [37], but if two ions reach the same channel of the MCP they are affected by the dead time of the channel and the signal of the second ion is not detectable [26]. This could mean, that the detection rate of double counts is much smaller than expected and the features A and C are fully caused by the creation of two ions.

An alternative process to create the prompt ions to the photo ionization is the interaction between multiple Rydberg atoms. This could lead to Penning ionization [56] where one of the Rydberg atoms is ionized in a Rydberg-Rydberg collision process. Normally, only one Rydberg atom is excited due to Rydberg blockade effects [43], however for the F-state it was observed that due to the many accessible magnetic sublevels a second Rydberg excitation is possible even inside the blockade radius [78]. Due to the mixed polarizations of all three photons involved in the Rydberg excitation, seven of the eight magnetic sublevels can be accessed. As the 58D state does not show the features A and C in the ionization trace, it is likely that those effects do not or less likely apply for the D state, also because only three magnetic sublevels are accessible. To gain further insight on the role of the blockade, we studied a scenario, where we first generated a D state in an off-resonant two-photon process and then applied a resonant microwave pulse to the $58D \rightarrow 56F$ transition. By that we are able to exploit that the D-state has less accessible magnetic sublevels than the F-state and thereby a more reliable Rydberg blockade.

A measurement of the ionization signal of the 56F state created with this scheme is depicted in Fig. 13c. The feature B is now composed of the ionization signal of the 56F state and that of an unknown residual population in the 58D state. This can be seen by the fact that the peak is much broader than for the pure 56F state (Fig. 13a). However, the almost identical ionization threshold fields of the two states states does not allow for a clear distinction of the former. A good indicator that the 56F state is indeed well populated gives the peak at 60 V/cm which is caused by the angle between magnetic and electric field and does not appear for the $58D$ state. The high-l feature C and the prompt ion feature A are much less populated for this scheme. In contrast to the direct off-resonant three-photon scheme, where I_B was as low as $I_B(\tau = 0) = 0.60$, with this method I_B is significantly larger at $I_B(\tau = 0) = 0.85$ and thereby comparable to the pure D state measurement with $I_B(\tau = 0) = 0.92$. Note though, that the comparison must be treated with some reservation, since the resonant scheme exhibits an unknown amount of D-state population which is known to ionize without features A and B. This result however reinforces the theory that those signals are caused by the creation of multiple Rydberg atoms. However, the life time of the F state could not be improved by this method. Further investigations of this process could be undertaken by studying its dependence on the principal quantum number n or its dependence on the applied electric field. This will indicate if a resonant Rydberg-Rydberg interaction process (Förster resonance) can occur for the current parameters [56]. Further insight could also be gained by investigating the Rydberg pair potentials of the F states in question numerically.

Conclusion

It was found that the unexpected low life time and ionization signal of the F state can not be contributed to a single malicious process. The unexpected ionization signals A and C can be likely attributed to Rydberg-Rydberg collisions, though the nature of the large collision rate is not clearly understood. The decay rate fits with the coarse presumption that every ground state atom within the F orbit causes a decay. However, it is yet to investigate why this is a good approximation for the F-state but not for the states with lower orbital momentum like the D state.

It was found, that the occurrence of the sharp peak at the low-field end of the high-l hump C is caused by an angle between the magnetic and the electric field. Even if this does not directly influence the F-state itself, we will find that the desired adiabatic rapid passage will not be possible with this angle present (Sec. 4.3.2). Only the low life time of the $56F$-state could not be explained or improved. The best results where obtained by decreasing the density of the atomic sample, making collisions with ground state atoms a possible issue, however the lifetime was still below the expected value. Further investigations in those directions should be undertaken to understand the underlying processes and how they could be avoided.

4.3 Circularization

In this section the creation and detection of circular Rydberg states by the adiabatic rapid passage method (Sec. 2.4) will be discussed.

4.3.1 Ionization of Circular States

To detect if a circular state was produced, state selective field ionization can be applied since the threshold field is by a factor of two larger than for the starting F state. The ionization threshold fields can again be calculated by the equation of Dammburg and Kolosov [12] (Eq. (2.19)) since the circular state is not influenced by the quantum defect. The resulting threshold voltages are shown and compared to the F state ionization fields in Fig. 5a. This method was successfully applied in [49] and [5] and provides a simple way to determine if the passage protocol was successful with equipment readily available in our current experimental setup. However, this method fails in distinguishing the circular Rydberg state from close by states. For example the ionization threshold field of the $56Fn_1 = 0, m_l = n - 2$ and the $56Fn_1 = 0, m_l = n - 1$ (CRS) are apart by only $2\,\mathrm{V/cm}$ which can not be easily detected in the current setup.

An alternative which can improve this shortcoming was applied successfully by Signoles et al. [66]. By probing the transition between the circular Rydberg state nC and a lower lying circular

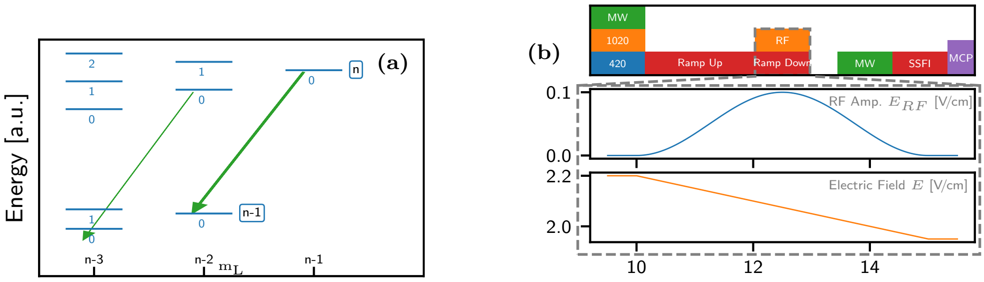

Figure 15: (a) By probing the circular state with principal quantum number n with a microwave transition to the circular state with $n-1$, it can be distinguished from close by states with $m_l = n-2$. Due to the n dependent stark shift, the microwave is out of resonance for other transitions. **(b)** Experimental sequence of the adiabatic rapid passage experiments. During the circularization process the RF amplitude E_{RF} is ramped up and down in an adiabatic way (middle). The dc electric field E is ramped down linearly (bottom). The parameters are the typical parameters for the circularization at $n = 56$ and an applied magnetic field of 15 G.

Rydberg state $(n-1)C$ or $(n-2)C$, the population of the nC state can be transferred to the lower one. This lower state has a much higher ionization threshold and can thereby be easily distinguished from the unwanted states. The microwave is only resonant to the transition between the circular Rydberg states, since the other transitions between lower m_l states are shifted by the n-dependent Stark shift as can be seen in Fig. 15a. Even though this method is clearly superior, it involves the use of a second microwave generator since the transition to the F state has typically another frequency than the $nC \rightarrow (n-1)C$ transition. It is not possible to switch the frequencies on the timescales of the experiment with the currently used microwave synthesizer. Hence, we will rely on state selective field ionization in this thesis.

4.3.2 Simulations

To study the efficiency of the adiabatic rapid passage (ARP) and determine the experimental parameters, a simulation code was developed and tested during the course of this thesis. In this section, we first describe the system and the approximations and methods used in the numerics and then investigate the influence of different parameters onto the quality of the passage. First, the problem is described as a closed quantum system and then extended to an open quantum system to account for unwanted transitions. The program was written in `Python` and makes use of the `QuTiP` module [34] to represent the density matrix and operators and solve the master equation in Lindblad form.

Theory and Implementation

The first step to describe the system in question is to assemble a suitable Hamiltonian H which contains all relevant dynamics but is limited enough to be numerically solvable. Since the different L states mix under the influence of an electric field, it would be necessary to include all states of a given principal quantum number in the Hamiltonian. For $n = 56$ this would yield a Hamiltonian of dimension $2n^2 = 6272$. By transforming the system to a parabolic basis (see Sec. 2.2), this number can be reduced drastically to only $2n - 1 = 111$ states. In this basis, the Stark states are eigenstates $|n, m_l, n_1, n_2\rangle$ with the parabolic quantum numbers n_1 and n_2. Since the adiabatic rapid passage circularization does in theory only address states with $n_1 = 0$ (see Fig. 16a), only these n states need to be included the calculations. However, since we do not have a purely σ^+ polarized RF field, the $n_1 = 0$ states couple to the other $n_1 \neq 0$ states via the σ^- polarized field.

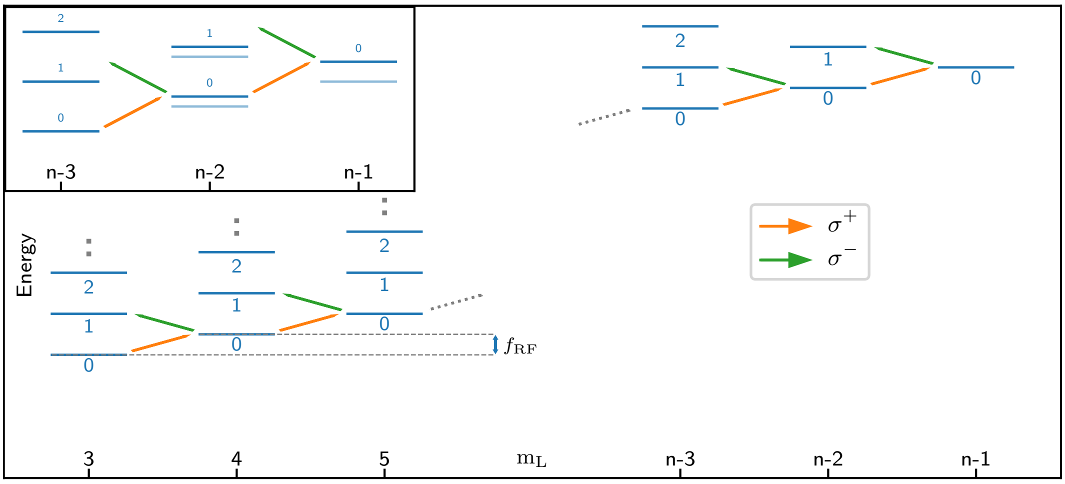

Figure 16: Principle of the RF-dressing of the hydrogenic manifold. The $n_1 = 0$ parabolic states of different m_l are coupled by a σ^+ polarized radio frequency field with frequency f_{RF}. In zero magnetic field $B = 0$, the states within one m_l ladder are all equally split by $2 \cdot f_{\mathrm{RF}}$ according to their n_1 quantum number. To reduce the coupling to unwanted $n_1 = 1$ states, a magnetic field can be applied to shift the σ^- transitions out of resonance (inset).

These parasitic transitions can be reduced by applying a magnetic field to lift the degeneracy of the σ^+ and the σ^- transitions. The passage can then be designed in a way that the σ^- are not resonant during the process. In the simulation, we will include these parasitic transitions to study the needed strength of the magnetic field by including the $n_1 = 1$ states and neglecting the higher $n_1 > 1$ states. Since the $|n, m_l, n_1, n_2\rangle$ basis is strictly speaking not an eigenbasis due to the quantum defect, the eigenstates and transition dipole moments are calculated numerically. Nonetheless, we will use this nomenclature in the following since the quantum defect does not change the general environment of the considered states. The low-l states which are strongly influenced by the quantum defect do not play a role in the calculation due to their splitting from the hydrogenic manifold and the states in the hydrogenic manifold which exhibit low-l character to some minor extent are only slightly shifted.

The numerically calculations for obtaining the relevant states and transition moments where carried out in the $|n, l, m_l\rangle$ basis. The Hamiltonian describing the system in this basis is given by

$$\boldsymbol{H'} = \boldsymbol{H'_A} + \boldsymbol{H'_B} + \boldsymbol{H'_E(t)}, \tag{4.22}$$

where the matrix representation of the bare atomic Hamiltonian $\boldsymbol{H'_A}$ and the magnetic interaction Hamiltonian $\boldsymbol{H'_B}$ are obtained from the numerics. The interaction of the atom with the electric field is described by

$$H'_E(t) = \boldsymbol{d'} \cdot E(t), \tag{4.23}$$

which includes the time dependence of the ramped electric field and the dipole moments d also obtained from the numerics. To obtain the eigenstates in the quasi-parabolic basis, the Hamiltonian (4.22) is diagonalized numerically by using `numpy.linalg.eig(H')`. Due to the time-dependent electric field, this eigenproblem needs to be solved for every time step of the simulation. Therefore, the system should be as small as possible. We restrict the basis to only the states within the same hydrogenic manifold, which includes the hydrogenic manifold nH itself and the nF, $(n+1)D$, $(n+2)P$ and $(n+3)S$ states. This can be interpreted as neglecting the quadratic stark shift onto the states of interest induced by the neighboring manifolds. An additional simplification can be made by splitting the system in multiple sub systems. Since the magnetic field and the dc electric field are assumed to be perfectly parallel during the ARP, the states with different m_l do not couple and can be treated as individual systems. This reduces the eigenproblem with dimension $2n+1$ to n separate problems with a maximum dimension of n.

The calculated eigenvectors $\boldsymbol{a} = \{a_i\}$ and eigenvalues ϵ_i of each subsystem are then sorted by their eigenvalue. This yields the eigenstates

$$|n, n_1, m_l\rangle = \sum_i a_i \, |n_i, n_{1_i}, m_l\rangle \tag{4.24}$$

sorted by their quasi-parabolic quantum number n_1 for each m_l. Since only the states with the lowest parabolic quantum numbers $n_1 = 0, 1$ are of interest to the ARP process, we select only those for the further calculation to reduce the dimension of the problem to $2n-1$.

The next step is to calculate the transition dipole moments between those states. The only allowed transitions are between adjacent m_l states, introduced by the σ^+ and σ^- polarized RF field (see Fig. 16a), due to angular momentum conservation. The σ^+ transitions can be calculated from the transition dipole moments in the $|n, L, m_l\rangle$ basis from the numerical calculations by

$$\begin{aligned} d^+_{m_l \to m_{l+1}} &= \langle n, n_1 = 0, m_l| \, d \, |n, n_1 = 0, m_l + 1\rangle \\ &= \sum_{i,j} a_i a'_j \, \langle n_i, L_i, m_l| \, d' \, |n_j, L_j, m_l + 1\rangle \, , \end{aligned} \tag{4.25}$$

where $\boldsymbol{a} = \{a_i\}$ and $\boldsymbol{a'} = \{a'_i\}$ are the eigenvectors of the initial and the target state in the $|n, L, m_l\rangle$ basis. The σ^- transitions can be calculated analogously

$$\begin{aligned} d^-_{m_l \to m_{l-1}}{}^{4} &= \langle n, n_1 = 0, m_l| \, d \, |n, n_1 = 1, m_l - 1\rangle \\ &= \sum_{i,j} a_i a'_j \, \langle n_i, L_i, m_l| \, d' \, |n_j, L_j, m_l - 1\rangle \, . \end{aligned} \tag{4.26}$$

The Rabi frequencies between the states induced by the RF field are then calculated by

$$\Omega^{\pm}_{m_l \to m_{l+1}} = d^{\pm}_{m_l \to m_{l+1}} \cdot E_{RF}(t). \tag{4.27}$$

By applying the rotating wave approximation [21], the Hamiltonian can be written as [22]

$$H_{i,i} = \Delta_i \tag{4.28}$$

$$H_{i,j} = \frac{\Omega_{i,j}}{2}. \tag{4.29}$$

The diagonal elements are given by the detunings

$$\Delta_i = \begin{cases} (i-s) \cdot f_{RF} - (\epsilon_i - \epsilon_s) & 0 < i \leq n-1 \\ f_{RF} - (\epsilon_{(i-n+1)} - \epsilon_i) + \Delta_{(i-n+1)} & n < i < 2n, \end{cases} \tag{4.30}$$

where the first n elements are the $n_1 = 0$ states and the last n elements the $n_1 = 1$ states. The integer s marks the index of the initial state which is chosen as the energetic zero point. For example for $s = 3$ the ARP starts from the $F, m_l = 3$ state. The off diagonal elements are given by the Rabi frequencies between the different states. As we consider only the σ^+ transitions between

---

[4] Note, that in the code the transition element $d^-_{m_{l-1} \to m_l}$ is calculated to reduce the amount of transition moments needed in the $|n, l, m_l\rangle$ basis, since $d^-_{m_l \to m_{l-1}} = d^-_{m_{l-1} \to m_l}$.

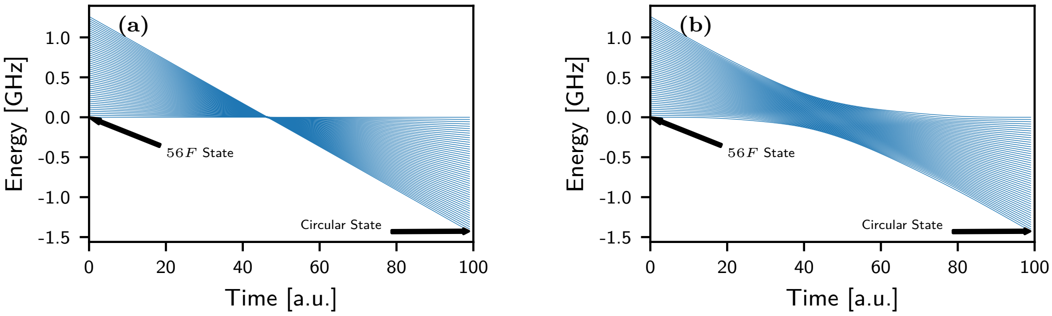

Figure 17: Eigenvalues of H of Eq. (4.29) during a typical ARP protocol. The dc field is ramped linearly from 1.85 V/cm to 1.4 V/cm. The applied RF field is ramped up and down adiabatically with the envelope given by Eq. (4.34). For no RF field applied **(a)**, the states cross at the point where the transitions from F to circular state are resonant with the RF frequency f_{RF}. For a finite RF field (0.1 V/cm in the example), the states form an avoided crossing due to the coupling **(b)**. If this crossing is traversed adiabatically, the population of the F state is transferred to the circular state. The $56F, m_l = 3$ state sets the point of zero energy.

the $n_1 = 0$ and between the $n_1 = 1$ states and the σ^- transitions between the corresponding $n_1 = 0$ and $n_1 = 1$ states, most of the off-diagonal elements are zero and can therefore be treated as sparse matrices in the numerics. Since the Rabi frequency is real and $\Omega_{i,j} = \Omega_{j,i}$, there are $3n$ non-zero off-diagonal values. A visual presentation of an example of the Hamiltonian H of Eq. (4.29) can be found in Appendix F.9. The eigenvalues[5] of this Hamiltonian are shown in Fig. 17a with no RF field $E_{\mathrm{RF}} = 0$ and Fig. 17b with a finite RF field $E_{\mathrm{RF}} \neq 0$. The electric field is ramped linearly from a value where the Stark splitting between adjacent $n_1 = 0$ states is larger than the RF frequency to a value where it is smaller during the time shown. Without the dressing induced by the RF field, the states cross at the point where the transitions are resonant to the σ^+ RF frequency. Due to the interaction arising from a finite RF field $E_{\mathrm{RF}} \neq 0$, the states do not cross anymore but exhibit an avoided crossing. To transfer the occupancy of the initial F state to the CRS, this crossing must be passed adiabatically.

To calculate the evolution of the state occupancy during the traversal of this crossing, the von Neumann equation (2.32) is solved numerically for the system with the initial conditions

$$\rho_i(0) = \begin{cases} 1 & i = s \\ 0 & \text{else.} \end{cases} \tag{4.31}$$

As a solver, the `QuTiP` solver `qutip.mesolve` is used, which evolves the initial state in accordance to the Hamiltonian in time and returns the resulting density matrix at pre-defined points in time. This solver is also capable of solving the Lindblad-Master equation (2.36), which makes it easy to generalize the simulation program to open quantum systems.

An example result for such a closed quantum system simulation is shown in Fig. 18a. For the chosen parameters the passage works with an efficiency close to 100 % efficiency. It turns out, that even for the case of zero magnetic field $B = 0\,\mathrm{G}$ the efficiency does not decrease for correctly chosen RF frequency f_{RF} and RF amplitude E_{RF}[6]. This is highly unexpected, since without the Zeeman shift between the m_l levels, the σ^+ and the parasitic σ^- transitions are degenerate (see Fig. 16a). By taking a closer look, it gets clear that population can coherently oscillate between the $n_1 = 0$ and $n_1 = 1$ states and even the fraction of the population in the $n_1 = 1$ states ends

---

[5] Note, that for the sake of clarity this representation only takes into account the states with $n_1 = 0$

[6] How those parameters need to be chosen is discussed in paragraph 4.3.2.

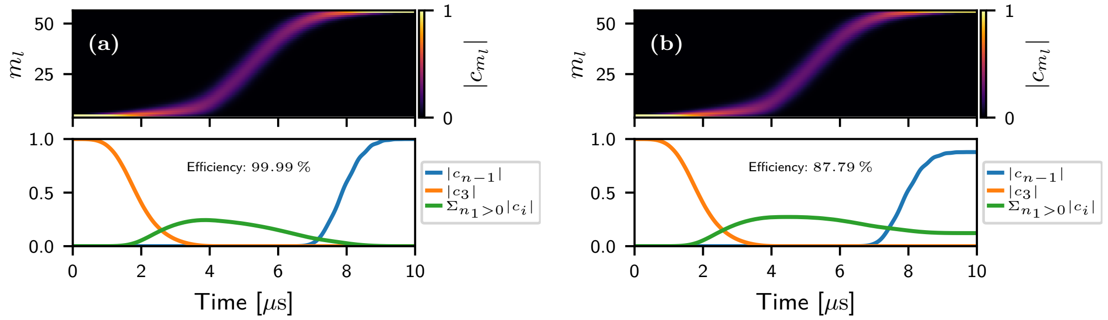

Figure 18: ARP simulation results for $n = 56$, $E_0 = 1.85\,\mathrm{V/cm}$, $E_1 = 1.4\,\mathrm{V/cm}$, $B = 15\,\mathrm{G}$, $f_{RF} = 195\,\mathrm{MHz}$ and $E_{RF} = 0.25\,\mathrm{V/cm}$ for both, the σ^- and σ^+ component. The color plot shows the population c_{m_l} in the $n_1 = 0$ states with different m_l during the passage process. The lower plots show the populations of the initial $56F$ (c_3) and the circular state (c_{n-1}). The occupation of the parasitic $n_1 > 0$ states is shown in green. For the closed quantum system treatment **(a)** the passage works with an efficiency of close to $100\,\%$, even though the $n_1 = 1$ states get populated during the protocol, they are transferred back to the circular Rydberg state. By including the states with $n_1 > 1$ as an environment in an open quantum system treatment **(b)** the efficiency is greatly decreased.

up in the circular state. In the real system, population in the $n_1 = 1$ states can not only oscillate back to the $n_1 = 0$ states but will partly be transferred to higher $n_1 > 1$ states.

This behavior can be included in the system by treating the system as an open quantum system without increasing the dimension of the Hamiltonian significantly. Therefore the von Neumann equation can be generalized to the Gorini–Kossakowski–Sudarshan–Lindblad (GKSL) equation (Eq. (2.36))

$$\frac{\partial \rho}{\partial t} = -\frac{i}{\hbar}\left[H(t), \rho\right] + \sum_i m_l \gamma_{m_l} \left(V_{m_l} \rho V_{m_l}^\dagger - \frac{1}{2}\left(\rho V_{m_l}^\dagger V_{m_l} + V_{m_l}^\dagger V_{m_l} \rho \right) \right), \tag{4.32}$$

which includes the coupling of the system to the environment through the collapse operators V_n. In the discussed system, the environment includes all states with $n_1 > 1$, which are not directly included in the Hamiltonian (4.29). Those are represented by one additional state $|m\rangle$. In the numerical Hamiltonian, this state is added to the end of matrix. The collapse operators are then given by the transition operators between the $n_1 = 1$ states and this $|m\rangle$ state,

$$V_{m_l} = |m\rangle \langle n_1 = 1, m_l| \,. \tag{4.33}$$

The corresponding decay rates are given by the γ_n coefficients. Since the coupling between the $n_1 = 1$ states and the other $n_1 \geq 1$ states is time dependent, the decay rates $\gamma_i(t)$ to model this process are also time dependent. We choose them to be the Rabi frequency of the σ^- transition between the respective $n_l = 1$ and the corresponding $n_l = 0$ state. This gives a good estimate since the population in the $n_1 = 1$ states will be driven to the $n_1 = 2$ states with a similar rate. Further, this approximation yields results well matching with the measurements of Nussenzveig et al. [49].

The simulation program gives a good understanding which parameters to choose in the experiment, however the versatility, accuracy and computation speed could be improved in various ways as the following list will explain:

- The simulation does not include the influence of neighboring hydrogenic manifolds. For $n = 56$ this is not a problem, since the circularization happens well below the crossing with

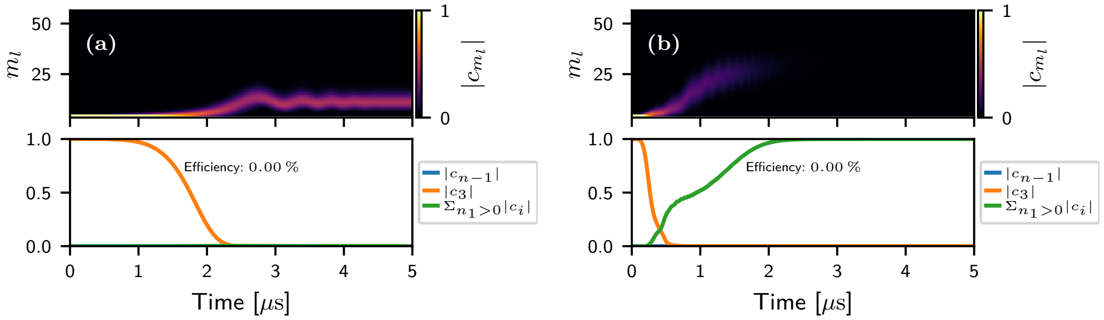

Figure 19: ARP simulation results for $n = 56$, $E_0 = 1.85\,\mathrm{V/cm}$, $E_1 = 1.4\,\mathrm{V/cm}$, $B = 15\,\mathrm{G}$ and $f_{RF} = 195\,\mathrm{MHz}$. The color plot shows the population c_{m_l} in the $n_1 = 0$ states with different m_l during the passage process. The lower plots show the populations of the initial $56F$ (c_3) and the circular state (c_{n-1}). The occupation of the parasitic $n_1 > 0$ states is shown in green. For the calculations, it was assumed that the σ^- and the σ^+ component of the RF field are equally strong. **(a)** If the RF field is chosen to weak ($E_{RF} = 0.01\,\mathrm{V/cm}$), the circular state is not reached. The avoided crossing (see Fig. 17b) is crossed partly diabatic and states with $m_l < n - 1$ are occupied. **(b)** If on the other hand the field is to strong ($E_{RF} = 1\,\mathrm{V/cm}$) the parasitic σ^- transitions gain importance, and the population is lost by scattering it across the hydrogenic manifold states. Note however, that this is only an effect of the σ^- transitions and the strength E_{RF} can be chosen arbitrary large for a pure σ^+ field.

other hydrogenic manifolds and they do not have a considerable influence. However, for larger principal quantum numbers, the electric field must be chosen closer to the crossing and the influence of the other manifolds increases. Taking into account more hydrogenic manifolds would therefore allow more precise statements on the ARP for higher principal quantum numbers. This could be easily implemented, however this would heavily increase the number of basis states in the $|n, L, m_l\rangle$ basis, increasing the computation time of the eigenvalue problem.

- The interaction Hamiltonian of the Stark states with the RF field is given in the rotating wave approximation. This limits the simulation to regimes where the RF frequency f_{RF} is much larger than the differential Stark shift during the electric field ramp. This again limits the principal quantum number since for larger quantum numbers the RF frequency must be chosen lower due to the Inglis-Teller limit. Including the exact Hamiltonian would lift this barrier but would also greatly increase the computational cost since the exact form includes rapidly varying terms and terms with values distributed over multiple orders of magnitude.
- The states which are included in the Hamiltonian are chosen at the beginning of the simulation. This means, that states that do not play a role at a given time of the ARP process due to negligible coupling to the populated states are nonetheless included in the Hamiltonian of this time step. For an adiabatic process, most of the time only a few states are considerably populated. By restricting the state set for every timestep, the dimension of the Hamiltonian could be greatly decreased.
- Currently, the simulation utilizes only a single CPU core. By implementing multicore support, the performance could be greatly improved especially on mainframe machines.
- By including more states with higher $n_1 > 1$ quantum number, the somewhat arbitrary chosen decay constants γ_i to simulate the loss to $n_1 > 1$ states can be obtained in a more rigorous way.

A documentation of the functions and classes of the `Python` program can be found in the Appendix G.

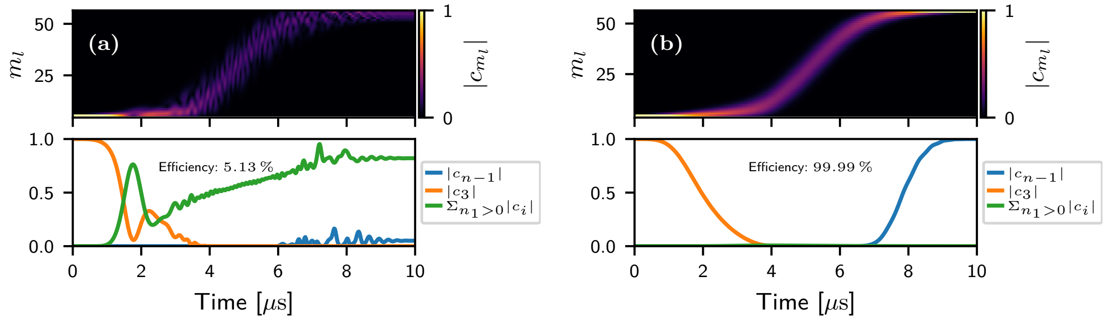

Figure 20: Simulation results for the ARP passage. The color plot shows the population c_{m_l} in the $n_1 = 0$ states with different m_l during the passage process. The lower plots show the populations of the initial $56F$ (c_3) and the circular state (c_{n-1}). The population in the parasitic $n_1 > 0$ states is shown in green. **(a)** Simulation for the same parameters as the simulation from Fig. 18b but in zero magnetic field $B = 0$. In this scenario, the σ^- and the σ^+ transitions are degenerate. The population is distributed over a multitude of states with $n > 0$ and the efficiency of the circularization vanishes. Note, that the simulation result is surely inaccurate for this case since the approximations used to model the Hamiltonian do not yield a good approximation due to the large flux to the $n_1 > 0$ states. **(b)** By decreasing the part of σ^- component to $10\,\%$ compared to the case of Fig. 18b, the efficiency can be increased drastically to $\approx 100\,\%$.

Simulation Results

The electric fields, both the dc field as well as the RF field play an important role in determining the success of the adiabatic passage. While the dc field can be chosen as a linear ramp between an initial field E_0 and an final field E_1 which is experimentally easy to achieve, the experimental realization of a suitable RF field is more difficult. If the RF field would be simply switched on at the beginning of the passage, the system would experience a quench and the population would be scattered into a multitude of states (see Appendix F.10a). It is also not an option to have the RF field activated during the whole sequence since the resonance is also crossed during the Stark switching when ramping up the electric field. Therefore, the amplitude of the RF signal must be ramped up adiabatically, which as it turns out is not easy to achieve in the experiment. The AWG used to generate the RF frequencies does only support frequencies up to 50 MHz in the arbitrary wave mode, where a pulse with arbitrary shape could be generated. To achieve the desired frequencies between 150 MHz and 200 MHz, the sine mode must be used. In principle, the device supports amplitude modulation by an external source. It turned out however, that this functionality is too slow and produces a stepped amplitude instead of the desired continuous, adiabatic rise for a pulse time on the order of a few μs. The solution to this problem is based on the `WaveCombine` functionality [41], which allows the added output of both channels through a single output terminal. Two signals with slightly different frequencies f_1 and f_2 can be added to form a beating signal. If the two signals start with a phase difference of π the signals cancel and then increase to the maximum value when they are in phase. The pulse is then given by a single beat period (Fig. 15b (middle))

$$E_{\mathrm{RF}}(t) = \begin{cases} E_{\mathrm{RF}} \cos\left(\frac{2\pi}{t_P} t\right) & 0 < t < {}^{t_P}\!/_2 = \tau_A \\ 0 & \text{else}, \end{cases} \tag{4.34}$$

where the length is given by the beat frequency

$$t_P = \frac{1}{f_B} = \frac{1}{|f_1 - f_2|}. \tag{4.35}$$

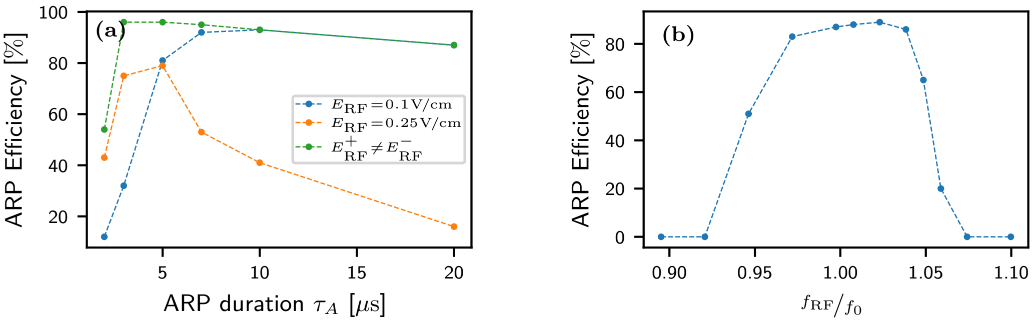

Figure 21: **(a)** Efficiency of the ARP protocol dependent on the duration of the transfer τ_A. For short durations, the crossing is traversed diabatically and the circular state is not reached. Although for large τ_A the crossing is traversed with high adiabaticity, the efficiency drops nonetheless since the parasitic σ^- transitions gain importance due to the longer driving. For higher RF fields E_{RF} the crossing can be traversed faster, increasing the efficiency for low durations τ_A. However the Rabi frequency of the σ^- transitions also increases, which lowers the overall efficiency by populating states with $n_1\!>\!0$. The green data ($E^+_{\mathrm{RF}}\!=\!0.25\,{}^{\mathrm{V}}\!/\!{}_{\mathrm{cm}}$, $E^-_{\mathrm{RF}}\!=\!0.1\,{}^{\mathrm{V}}\!/\!{}_{\mathrm{cm}}$) shows that the loss in efficiency for long durations τ_A is only governed by the σ^- component. **(b)** Efficiency of the ARP protocol dependent on the detuning from the resonance frequency f_0. The CRS is populated well for a frequency f_{RF} within 5% of the resonance frequency. No transfer can be achieved if the frequency is so far detuned, that the crossing is not within the electric field ramp of the protocol. The lines are guides to the eye.

Since for the typical passage length of $\tau_A = 10\,\mu$s the frequency difference is $100\,$KHz and thereby much smaller than the carrier frequency, it does not play a role concerning the coupling between the Stark states in the passage protocol. This gives us the possibility to generate adiabatic RF pulses with a frequency up to $200\,$MHz with an almost arbitrary length. All simulations and experiments, if not otherwise noted, are carried out with this pulse form.

The goal is now to find the optimal parameters to implement the protocol in the experiment and further investigate the influence of the different parameters of the ARP. A good set of parameters can be obtained from the Stark map of the $56F$ states, since the passage will only work if the crossing is traversed during the chosen dc field ramp. Since higher RF frequencies are favorable, $f_{RF} = 195\,$MHz is chosen close to the maximum experimentally available frequency. The electric fields $E_0 = 1.85\,{}^{\mathrm{V}}\!/\!{}_{\mathrm{cm}}$ and $E_1 = 1.4\,{}^{\mathrm{V}}\!/\!{}_{\mathrm{cm}}$ are then chosen in a way that the crossing is traversed in the middle of the passage to ensure that the dressing given by the RF pulse (4.34) is maximal at this point. For the magnetic field it can be assumed that the best results are obtained for larger fields, since the parasitic σ^- transitions are further from resonance. Therefore a field of $B = 15\,$G is chosen, which is easily achievable in the experiment. Only the RF amplitude and the time of the passage do not allow an easy intuitive choice, hence we will start with investigating the effects of the RF amplitude.

It is assumed that the field contains both polarizations σ^+ and σ^- to an equal degree

$$E^+_{\mathrm{RF}} = E^-_{\mathrm{RF}} = E_{\mathrm{RF}}, \tag{4.36}$$

since this resembles the experimental situation, where the field is applied to a single electric field plate. If the RF amplitude is chosen too small, the splitting of the avoided crossing will be too small to be traversed adiabatically. Fig. 19a shows this scenario, where the amplitude is $0.01\,{}^{\mathrm{V}}\!/\!{}_{\mathrm{cm}}$ and the passage time $5\,\mu$s. The population is transferred diabatically into states with low $m_l \ll n-1$. The higher the amplitude is chosen, the higher the m_l of the reached state. However, if the field is chosen too strong, the parasitic σ^- transitions gain importance and a higher fraction is scattered to the $n_1 > 0$ states and therefore lost. This can be seen in Fig. 19b,

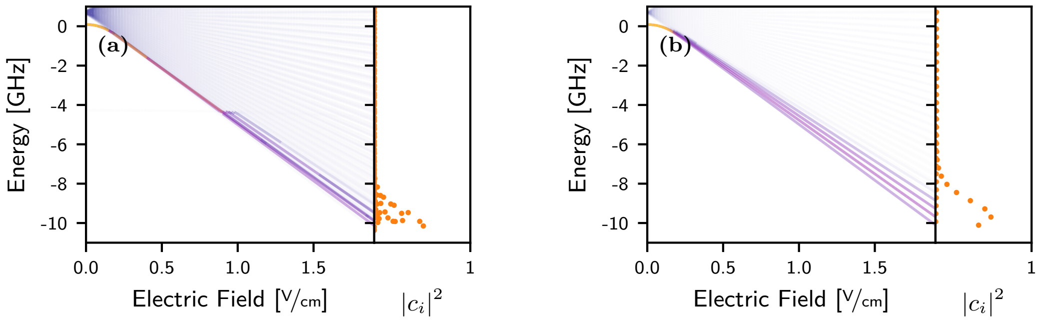

Figure 22: **(a)** Dynamic simulation of Stark switching from $0\,\mathrm{V/cm}$ to $1.85\,\mathrm{V/cm}$ in $10\,\mu\mathrm{s}$. The magnetic field of $15\,\mathrm{G}$ is applied under an angle of $5\,°$ to the electric field. Due to the angle, the different m_l levels mix and avoided crossings arise. The Stark switching is not adiabatic and the population is spread over multiple Stark states (right) after the Stark switching. **(b)** The same scenario for a perfectly aligned magnetic field but a reduced ramp time of $0.05\,\mu\mathrm{s}$. The fast traversing of the crossing into the hydrogenic manifold causes partly diabatic crossings, scattering the population over a multitude of states.

where the amplitude is chosen $1\,\mathrm{V/cm}$ for both σ^+ and σ^-. Note, that this would translate to a voltage of $> 10\,\mathrm{V_{pp}}$ at the AWG when including the spacing of the field plates and the transfer efficiency of the plates (see Sec. 4.1). This is not experimentally achievable. If the field does not contain a σ^- component, this limitation does not arise and the field can be chosen arbitrarily strong (cf. Appendix F.10b). We found that for a ramp time of $5\,\mu\mathrm{s}$ the CRS is reached with an efficiency $> 75\,\%$ for amplitudes between $E_\mathrm{RF} = 0.1\,\mathrm{V/cm}$ and $E_\mathrm{RF} = 0.25\,\mathrm{V/cm}$.

The influence of the ARP duration τ_A onto the efficiency is studied in Fig. 21a. For short τ_A, the protocol is inefficient due to a mostly diabatic traversal of the crossing, similar to the use of a too weak dressing field. However the efficiency does not rise to unity for an infinitely long passage as would be expected from basic Landau-Zener theory. The contrary is observed as the efficiency quickly decreases after reaching an optimal value for increasing passage durations τ_A. This is caused by Rabi oscillations to the parasitic σ^- states. Though an increase in σ^+ field strength increases the adiabaticity of the crossing, it also increases the occupation of the n_1 states. As can be seen clearly, for an RF field of $E_\mathrm{RF} = 0.25\,\mathrm{V/cm}$ the maximum efficiency reached is lower than for $E_\mathrm{RF} = 0.1\,\mathrm{V/cm}$ and the range of τ_A where the efficiency is $> 80\,\%$ is significantly smaller. This sensitivity can again be decreased by reducing the σ^- polarized fraction of the field as can be seen from the green points, where the fields are $E^+_\mathrm{RF} = 0.25\,\mathrm{V/cm}$ and $E^-_\mathrm{RF} = 0.1\,\mathrm{V/cm}$. It is apparent, that the decrease in efficiency for larger passage times τ_A is only governed by the strength of the σ^- component of the field.

Changing the frequency of the RF field and changing the start and end point of the passage will have the same effect since it effectively changes the point of time where the crossing is traversed. If the crossing is reached to early, which corresponds to a higher RF frequency $f_{RF} > f_{RF}^{opt}$, the amplitude at the crossing is effectively smaller, increasing the diabatic crossing fraction (cf. Appendix F.11b). A similar behavior is found when going to lower frequencies $f_{RF} < f_{RF}^{opt}$ (cf. Appendix F.11a). For the typical parameters used in this thesis, the CRS is reached with a high fidelity if the frequency f_RF lies within $5\,\%$ of the optimal frequencies $f_\mathrm{RF}^\mathrm{opt}$ (cf. Fig. 21b).

That the σ^- transitions have a large influence in deciding the success of the passage can also be observed by studying the system without a magnetic field $B = 0$ (Fig. 20a). In this scenario, the σ^- and the σ^+ transitions are almost degenerate. The population is distributed over a multitude of states with $n > 0$ and the efficiency of the circularization vanishes. Note, that the simulation result of Fig. 20a is surely inaccurate for this case since the approximation used to model the

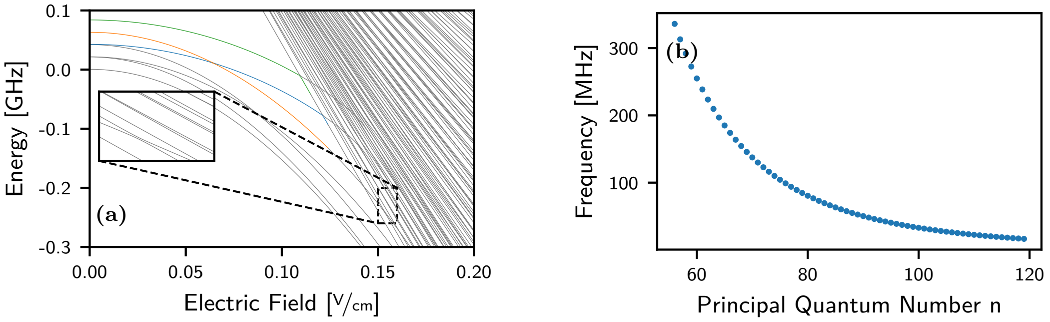

Figure 23: (a) Stark map of the $56F$ state at an angle of $5\,^{\circ}$ between the magnetic and the electric field. The different m_l, m_s level are split up by the applied magnetic field of $B = 15\,\mathrm{G}$ by the Paschen-Back effect. The Zeeman states $m_l = 3, m_s = {}^1/_2$ (green), $m_l = 3, m_s = -{}^1/_2$ (blue) and $m_l = 2, m_s = {}^1/_2$ (orange) are highlighted. The inset shows the crossing of the $m_l = 2, m_s = {}^1/_2$ state into the hydrogenic manifold. If the magnetic field is parallel to the electric field the crossing is a real crossing, but already under an angle of $5\,^{\circ}$ the crossing becomes avoided with a splitting of 5 MHz. **(b)** The Inglis-Teller limit (Eq. (2.21)) where the hydrogenic manifold n crosses with the manifold $n-1$ gives a hard limit for the RF frequency of the ARP protocol. Since the splitting of the adjacent Stark states increases only $\propto n$ and the Inglis Teller limit decreases $\propto {}^1/_{n^5}$, the maximum splitting drops quickly to unpractical frequencies.

states $n_1 > 1$ do not yield a good approximation due to the large flux to the $n_1 > 0$ states. Until now we always assumed that the σ^- field is equally strong as the σ^+ field, as it is in the experiment easily achievable. The advantage is the experimental simplicity, as the RF field is only applied to a single electric field plate in z direction, which produces a field with equal parts of σ^- and σ^+ polarization in the x direction. However, as can be seen in Fig. 20b the reduction of the σ^- component yields large improvements to the efficiency of the passage protocol. The decrease of the σ^- component to $10\,\%$ of the σ^+ component increases the efficiency by $12.2\,\%$ compared to Fig. 18b to almost $100\,\%$. This means that even for not perfectly pure σ^+ polarization, the magnetic field can be omitted, increasing the simplicity of the experiment. A possible way to produce pure σ^+ polarized field in the experiment is to apply an additional RF field with a $90\,^{\circ}$ phase difference in y direction. The challenge here is to determine the correct phase difference and amplitude relation of the two applied signals, since it depends on time differences caused by cable length and feedback of the field plates. Nevertheless, it is a technique which should be pursued further since it increases the efficiency greatly [66].

4.3.3 Electric Field and Stark Switching

The starting point of the ARP circularization method is at finite electric field, where the F state has crossed into the hydrogenic manifold of same principal quantum number to achieve an equal spacing between the initial F state and the remaining $n_1 = 0$ states. As it is not possible to excite the target state selectively in this environment, it is required to transfer the state excited in a zero or small electric field to the target electric field. When crossing into the hydrogenic manifold, many avoided crossings must be traversed adiabatically, limiting the slew rate of the applied electric field ramp. In Fig. 22b, the Stark switching with a slew rate of $3.8 \cdot 10^7\,{}^{\mathrm{Vs}}/_{\mathrm{cm}}$ is simulated. This slew rate corresponds to a ramp time of $0.05\,\mu\mathrm{s}$. The fast switching speed causes some crossings to be partly diabatic which causes the occupation of a multitude of states. We find from the simulation, that a slew rate on the order of $10^5\,{}^{\mathrm{Vs}}/_{\mathrm{cm}}$ suits the needs for an adiabatic transfer with a fidelity over $99\,\%$.

Another problem arises if the magnetic field is not parallel to the electric field used for the adiabatic rapid passage or state selective field ionization. The different m_l levels couple due to the interaction with the magnetic field. This can in fact be used in a controlled way for circularization as part of the crossed fields method used by Brecha et al. [5], however it is undesirable for performing the adiabatic rapid passage method and the therefore needed Stark switching. As already seen in the ionization spectra of the $56F, m_l = 2$ state (Sec. 4.2.2) an angle[7] of 2.9 ° between the fields is present in the experiment and causes problems in creating clean ionization signals. The interaction causes avoided crossing between levels with different m_l and disturbs the structure of the hydrogenic manifold. The crossings of the state relevant to the adiabatic rapid passage ($56F, m_l = 2, m_s = {}^1\!/_2$) with the manifold states becomes avoided by applying the magnetic field under an angle. In Fig. 23a this crossing is shown for an angle of 5 ° between the magnetic and the electric field. Even for this small angle, the splitting at the crossing is already 5 MHz. To reach the starting position for the ARP successfully, this and many other, similar crossings must be traversed diabatically. By simulating the Stark switching process (Fig. 22a) it gets clear that for a slow ramp of 10 μs to a starting field of 1.85 V/cm[8] this is not the case and the population is scattered over a multitude of states. The fidelity of the following ARP process is therefore decreased, since not only the $|m_l = 2, n_1 = 0\rangle$ state but also $|m_l = 2, n_1 > 0\rangle$ states are populated.

Note, that in the experimental realization, the Stark switching field is only applied to one electric field plate (X1), since the other one is driven by an HV amplifier which exhibits high noise. The noise can be clamped out by using a switching circuit (see Sec. C) for applying an offset field. However it is not possible to pass a non-static electric field through the offset channel of this switch as it would open the port of the HV amplifier and allow its noise to pass onto the field plates.

4.3.4 Limitations of the ARP method

The adiabatic rapid passage circularization method can not be easily generalized to principal quantum numbers much larger than 60. The main cause is the limitation given by the Inglis-Teller limit. Above this limit, where the hydrogenic manifolds with different principal quantum numbers cross, the energetic structure of the Stark states gets much more complex. Than, the RF field can not only couple the different m_l states of the same principal quantum number, but also introduces a coupling between the states with different principal quantum number. As a consequence, the target $n_1 = 0$ states are no longer equally spaced and the passage is no longer possible. Therefore the Inglis-Teller limit gives an upper limit onto the applied dc field. This in return limits the maximum splitting between adjacent $n_1 = 0$ states. As the Inglis-Teller limit is proportional to $\propto \frac{1}{n^5}$ [23] and the splitting of the Stark states increases only with $\propto n$, the maximum RF frequency rapidly decreases with increasing principal quantum number n as can be seen in Fig. 23b. For $n = 100$, the maximum frequency is only 33 MHz. Since the variation in the Stark energy must be larger than the Rabi frequency induced by the RF field Ω [49] to avoid Rabi oscillations to unwanted states and the ARP duration must be much greater than $1/\Omega$ to keep the transfer adiabatic, this low Stark splitting would heavily limit the speed of the passage to the point where the passage is longer than the lifetime of the target circular state $\propto n^2$[9] [11]. By improving the simulation to cope with quantum numbers $n > 70$, it can be used to find this limit by determining the passage time needed for an adiabatic transfer with high enough fidelity.

4.3.5 Measurement

For a first experiment it is convenient to choose not the maximum feasible RF frequency of the AWG (200 MHz), as the resonance frequency since this would inhibit any scanning of the frequency

---

[7] For an applied magnetic field of $B = 5$ G.

[8] This is the starting field for the protocol at $n = 56$ and an RF frequency of $f_{RF} = 195$ MHz as was simulated in Fig. 18b.

[9] With black body radiation induced decay included.

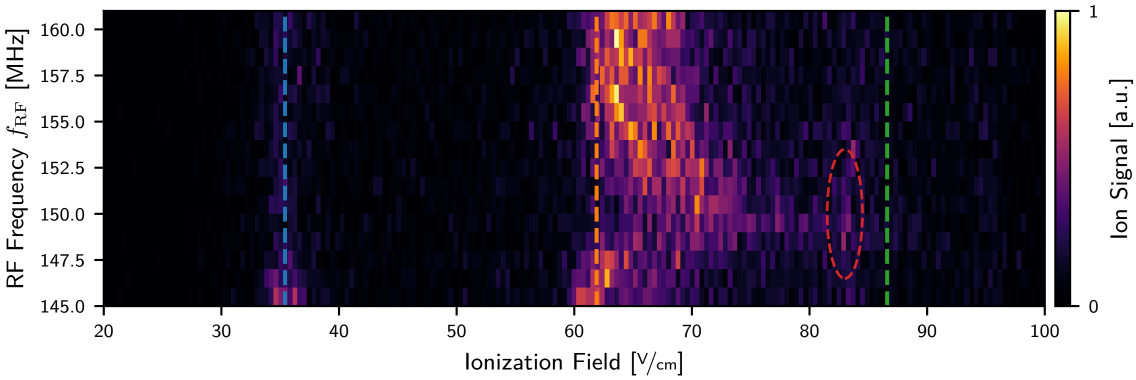

Figure 24: State selective field ionization measurement of the ARP sequence for different RF frequencies f_{RF}. The field is ramped down from $E_1 = 1.4\,\mathrm{V/cm}$ to $E_0 = 1.0\,\mathrm{V/cm}$ while the RF field with an amplitude of $E_{\mathrm{RF}} \approx 0.1\,\mathrm{V/cm}$ is active. The blue line marks the ionization threshold of the $56F$ state obtained from calculations including the quantum defect (see Eq. (2.22)), the orange line the value from calculations without quantum defect for the same state (see Eq. (2.19)). Close to the calculated resonance of $f_0 = 150\,\mathrm{MHz}$, the ion signal shifts visibly to higher ionization fields towards the ionization field of the circular state (green). The broad high-l signal is less visible in this figure compared to for example Fig. 11a because of the different scaling of the color map.

to compensate inaccuracies in the dc field. Further the maximum field strength E_{RF} we can obtain at the position of the atoms drops with increasing frequency (see Sec. 4.1 and Appendix D). Therefore passage parameters where chosen for a resonance frequency of $f_0 = 150\,\mathrm{MHz}$.

The electric dc field is ramped down from $E_1 = 1.4\,\mathrm{V/cm}$ to $E_0 = 1.0\,\mathrm{V/cm}$ in $\tau_A = 10\,\mu\mathrm{s}$ and the amplitude of the RF pulse is $E_{\mathrm{RF}} \approx 0.1\,\mathrm{V/cm}$[10]. For these parameters, the simulation yields an efficiency of 88 %.

The state selective field ionization signals for various RF frequencies f_{RF} around the resonance frequency $f_0 = 150\,\mathrm{MHz}$ is shown in Fig. 24 for an measurement with the stated parameters. The ion signal visibly shifts to higher ionization fields close to the resonance f_0, which is an indication that the ARP is at least partially successful. A weak signal is visible close to the theoretical ionization threshold of the circular state (green), which is highlighted by the red circle. It is not possible to determine with certainty if this signal originates from the circular state or any lower state. Already a slight mismatch of $0.1\,\mu\mathrm{s}$ in the mapping of the ion detection time to the ionization voltage (cf. 8b) causes a shift of the observed difference between the supposed CRS signal and the theoretical ionization value. A way to gain certainty is to implement a microwave detection scheme (cf. [49, 66] and Fig. 15a), so the CRS can be distinguished from the states which have a too similar ionization threshold to be clearly distinguishable with SSFI.

For off-resonant frequencies, the passage is not successful as expected and the ionization signal appears close to the hydrogenic ionization field of the F state (orange). However, the frequency region in which a substantial shift is visible is much smaller than expected from the simulations (cf. Fig. 21b). A possible explanation is that the RF pulse is not transmitted to the atoms in a clean way but is distorted, giving a much smaller time window in which the coupling is strong enough to traverse the crossing adiabatically. Another cause can be found in the σ^- transitions. It was found in Sec. 4.3.2 that for higher powers, the ARP efficiency is more sensitive to non-optimal parameters due to these parasitic transitions. The exact distribution of the polarizations of the

---

[10] This value includes the conversion factors resulting from the plate efficiency of the $Z1$ electric field plate (see Fig. 1b) and the output deviation of the used AWG (see Appendix D) and corresponds to a set voltage of $0.75\,\mathrm{V_{pp}}$.

applied RF field is not known in the experiment. It is imaginable that the σ^- component is underestimated, which would reduce the frequency range for a successful ARP.

In Fig. 24 the broad high-l signal is less visible than in the measurements of the F state in Sec. 4.2.3, due to scaling of the color map to visualize the result of the ARP process. It is however still present in the measurement and prevents a higher fidelity and a systematic optimization of the supposed CRS ionization signal.

This measurement clearly shows that all the ingredients for a successful adiabatic passage are available at the experimental setup and yields a first proof-of-principle on which upon the sequence can be optimized in future experiments after the issues with reaching the initial F state (cf. Sec. 4.2.3) are solved.

Conclusion and Outlook

In the course of this thesis, the creation of circular Rydberg states in an ultracold atomic gas via an adiabatic rapid passage (ARP) method was investigated and preparatory measurements where conducted. First it was shown, that a radio frequency field which is needed for the ARP can be applied efficiently to the atoms by investigating the creation of Floquet sidebands.

Further, it was found that the F state, which is used as the initial state for the ARP, can be reached with the current microwave setup for a wide range of principal quantum numbers where $n > 48$. However, for $n > 58$ a steep decrease in the transition dipole moment was found, which could limit the efficiency of the used off-resonant three photon process to excite the target F state. By employing a ramped state-selective field-ionization (SSFI) scheme, the ionization behavior of the $56F$ state was examined. It was found, that the lifetime is much shorter than expected and therefore shorter than needed for a successful adiabatic passage. Evidence was found that the fast decay can be attributed to two collision processes. On the one hand side, Rydberg-Rydberg collisions caused by the low reliability of the Rydberg blockade of the F state due to many accessible magnetic sub levels, on the other collisions with ground state atoms on the other. The impact of the former process was decreased by applying an excitation scheme based on a resonant excitation of the D state to exploit its more reliable Rydberg blockade. The latter process was found to be well approximated by assuming that every ground state in the F-state orbit leads to a collision event which is surprising and needs to be investigated further by for example studying the scattering potential of the F state. The decay could however be well reduced by reducing the density of the atomic sample.

Further, it was found that the angle between the magnetic field and the electric ionization field has a strong influence on the ionization behavior. Attempts to compensate an angle caused by magnetic stray fields were started in this thesis. Since this angle does not only affect the ionization but also the ARP itself, this endeavor needs to be pursued further.

During this thesis, a simulation program was developed to simulate the ARP process. It was found, that the ARP provides a stable method for circularization, but also that the parasitic σ^- transitions to unwanted states play a larger role than expected. A large improvement could be made by not applying a π-polarized field, but a purely σ^+-polarized field. This is achievable in the current experimental setup by applying the RF-field to two perpendicular electric field plates with a phase difference of $90\,^\circ$. It would be useful for future studies to extend and improve the simulation code to be able to simulate the ARP for higher principal quantum numbers. With this, one should be able to investigate if the adiabatic method is still feasible with a high enough fidelity for $n \approx 100$. In the case that another adiabatic circularization scheme should be used, the code could be easily expanded to for example the crossed fields method, by replacing the interaction induced by the RF-field with the state mixing induced by the magnetic angle.

Experimental evidence was found, that the ARP protocol can be applied successfully in our setup to excite CRS with $n = 56$. The measured signal provides a starting point for further optimization of the ARP parameters after the mentioned difficulties with preparing the initial F state are solved. Since the D state does not exhibit these problems, it would be appealing to use a D state as an initial state of the ARP. If this is possible without loosing efficiency is currently investigated with the help of the simulation program written in this thesis. An additional advantage of this scheme would be that the microwave previously used to excite the F-state can be used to probe the circular Rydberg state with a higher efficiency than the currently used SSFI scheme.

Appendix

A Automated Field Compensation Routine

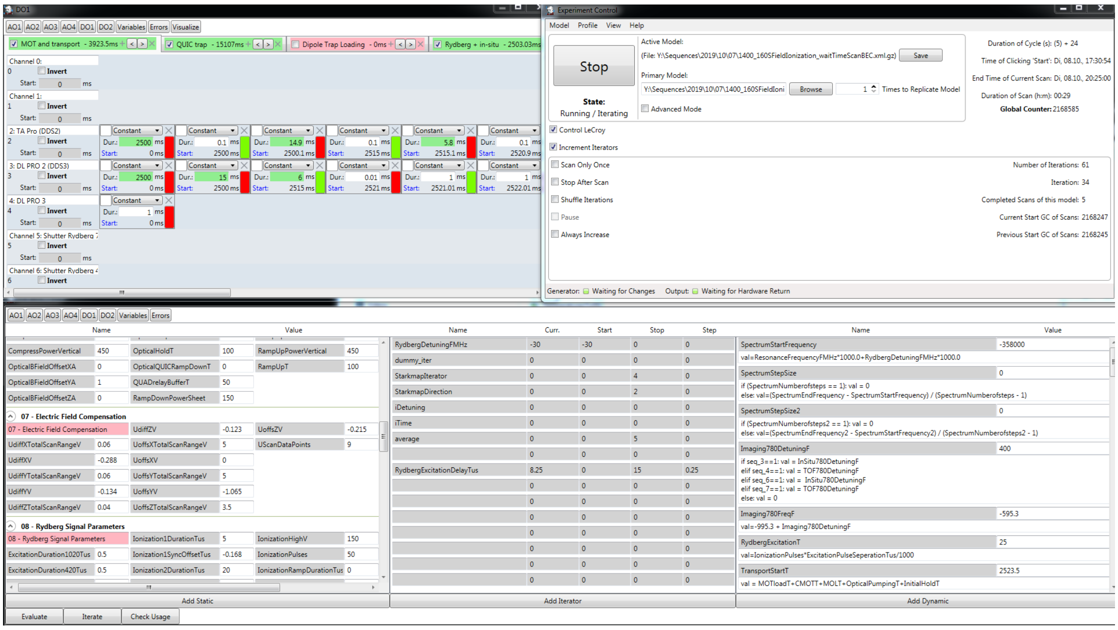

☑ MOT and transport - 3923.5ms
☑ QUIC trap - 15107ms
☐ Dipole Trap Loading - 0ms
☑ Rydberg + in-situ - 2503.03ms

Channel						
Channel 0: 0 ☐ Invert Start: 0 ms						
Channel 1: 1 ☐ Invert Start: 0 ms						
2: TA Pro (DDS2) 2 ☐ Invert Start: 0 ms	Constant Dur.: 2500 ms Start: 0 ms	Constant Dur.: 0.1 ms Start: 2500 ms	Constant Dur.: 14.9 ms Start: 2500.1 ms	Constant Dur.: 0.1 ms Start: 2515 ms	Constant Dur.: 5.8 ms Start: 2515.1 ms	Constant Dur.: 0.1 ms Start: 2520.9 ms
3: DL PRO 2 (DDS3) 3 ☐ Invert Start: 0 ms	Constant Dur.: 2500 ms Start: 0 ms	Constant Dur.: 15 ms Start: 2500 ms	Constant Dur.: 6 ms Start: 2515 ms	Constant Dur.: 0.01 ms Start: 2521 ms	Constant Dur.: 1 ms Start: 2521.01 ms	Constant Dur.: 1 ms Start: 2522.01 ms
4: DL PRO 3 4 ☐ Invert Start: 0 ms	Constant Dur.: 1 ms Start: 0 ms					
Channel 5: Shutter Rydberg 7 5 ☐ Invert Start: 0 ms						
Channel 6: Shutter Rydberg 4 6 ☐ Invert						

Active Model:
(File: Y:\Sequences\2019\10\07\1400_160SFieldIonization_waitTimeScanBEC.xml.gz)
Primary Model:
Y:\Sequences\2019\10\07\1400_160SFieldIoni
1 Times to Replicate Model
☐ Advanced Mode
State:
Running / Iterating

Duration of Cycle (s): (5) + 24
Time of Clicking 'Start': Di, 08.10., 17:30:54
End Time of Current Scan: Di, 08.10., 20:25:00
Duration of Scan (h:m): 00:29
Global Counter: 2168585

☑ Control LeCroy
☑ Increment Iterators

☐ Scan Only Once
☐ Stop After Scan
☐ Shuffle Iterations
☐ Pause
☐ Always Increase

Number of Iterations: 61
Iteration: 34
Completed Scans of this model: 5
Current Start GC of Scans: 2168247
Previous Start GC of Scans: 2168245

Generator: 🟩 Waiting for Changes Output: 🟩 Waiting for Hardware Return

Name	Value	Name	Value	Name	Value
CompressPowerVertical	450	OpticalHoldT	100	RampUpPowerVertical	450
OpticalBFieldOffsetXA	0	OpticalQUICRampDownT	0	RampUpT	100
OpticalBFieldOffsetYA	1	QUADrelayBufferT	50		
OpticalBFieldOffsetZA	0	RampDownPowerSheet	150		
07 - Electric Field Compensation					
07 - Electric Field Compensation		UdiffZV	-0.123	UoffsZV	-0.215
UdiffXTotalScanRangeV	0.06	UoffsXTotalScanRangeV	5	UScanDataPoints	9
UdiffXV	-0.288	UoffsXV	0		
UdiffYTotalScanRangeV	0.06	UoffsYTotalScanRangeV	5		
UdiffYV	-0.134	UoffsYV	-1.065		
UdiffZTotalScanRangeV	0.04	UoffsZTotalScanRangeV	3.5		
08 - Rydberg Signal Parameters					
08 - Rydberg Signal Parameters		Ionization1DurationTus	5	IonizationHighV	150
ExcitationDuration1020Tus	0.5	Ionization1SyncOffsetTus	-0.168	IonizationPulses	50
ExcitationDuration420Tus	0.5	Ionization2DurationTus	20	IonizationRampDurationTus	0

Name	Curr.	Start	Stop	Step
RydbergDetuningFMHz	-30	-30	0	0
dummy_iter	0	0	0	0
StarkmapIterator	0	0	4	0
StarkmapDirection	0	0	2	0
iDetuning	0	0	0	0
iTime	0	0	0	0
average	0	0	5	0
	0	0	0	0
RydbergExcitationDelayTus	8.25	0	15	0.25
	0	0	0	0
	0	0	0	0
	0	0	0	0
	0	0	0	0
	0	0	0	0
	0	0	0	0
	0	0	0	0

Name	Value
SpectrumStartFrequency	-358000

```
val=ResonanceFrequencyFMHz*1000.0+RydbergDetuningFMHz*1000.0
```

Name	Value
SpectrumStepSize	0

```
if (SpectrumNumberofsteps == 1): val = 0
else: val=(SpectrumEndFrequency - SpectrumStartFrequency) / (SpectrumNumberofsteps - 1)
```

Name	Value
SpectrumStepSize2	0

```
if (SpectrumNumberofsteps2 == 1): val = 0
else: val=(SpectrumEndFrequency2 - SpectrumStartFrequency2) / (SpectrumNumberofsteps2 - 1)
```

Name	Value
Imaging780DetuningF	400

```
if seq_3==1: val = InSitu780DetuningF
elif seq_4==1: val = TOF780DetuningF
elif seq_6==1: val =  InSitu780DetuningF
elif seq_7==1: val = TOF780DetuningF
else: val = 0
```

Name	Value
Imaging780FreqF	-595.3

```
val=-995.3 + Imaging780DetuningF
```

Name	Value
RydbergExcitationT	25

```
val=IonizationPulses*ExcitationPulseSeperationTus/1000
```

Name	Value
TransportStartT	2523.5

```
val = MOTloadT+CMOTT+MOLT+OpticalPumpingT+InitialHoldT
```

Figure A.1: Screenshot of the main experiment control program. The top left shows the programming interface of the `National Instruments` digital and analog `I/O` cards. The top right shows the control window which allows to start the experiment and simultaneously displays current status information. The lower part shows the variable screen where different types of input parameters can be set.

In this thesis, a feedback routine was developed to automatically compensate electrical stray fields using the *advanced mode* of the experiment control program (cf. Sec. 3.4). This enables longer non-supervised, electric field sensitive Rydberg measurements on the order of a few days.

The software is split into two main parts, a Python script which handles the coordination of the models in the main experiment control and a `MATLAB` program on a second machine which handles the evaluation of the measured data. A typical evaluation procedure is schematically shown in Fig. A.2. In the following a short outline of this procedure is given. A more thorough description and documentation can be acquired from the author on request. The Python script of the main experiment control is executed before every cycle of the experiment by the experiment control software itself. Based on the parameters chosen by the user (which exemplarily can be a time-dependence) the measurement model is changed to the Stark map model and simultaneously a signal and the current *global counter* as well as the number of voltage steps of the Stark map (`vsteps`) is sent to the evaluation program via a socket connection. When the evaluation program receives the signal that a Stark map will be measured, a background process is started which listens for new measurement data. If new data is found the spectrum is evaluated and the position of the Rydberg line is determined. After the Stark map measurement is completed in all three spatial directions, the experiment control Python script sends a signal to the evaluation program and switches to a third, “dummy” model. This model is used to accustom the experiment to the different parameters of the main model compared to the stark map model and to bridge the time which is needed for evaluation. This evaluation time is typically 30 s, hence the dummy cycle is repeated two or three times.

When the signal is received by the evaluation program that the measurement is completed, the background process is stopped and a parabola is fitted to the determined Rydberg line positions (see Sec. 3.1.1), yielding the new compensation values. The extracted values are then sent to the experiment control and the evaluation software listens for further signals from the experiment control again. When the evaluation is completed, the new compensation values are sent back to the experiment control and the main routine is loaded and started. However, if the evaluation fails, the experiment control repeats the Stark map measurement up to a maximum number of retries, set by the user. Failure can occur if for example no values could be extracted from the measurement, the connection fails or the measured data is corrupted.

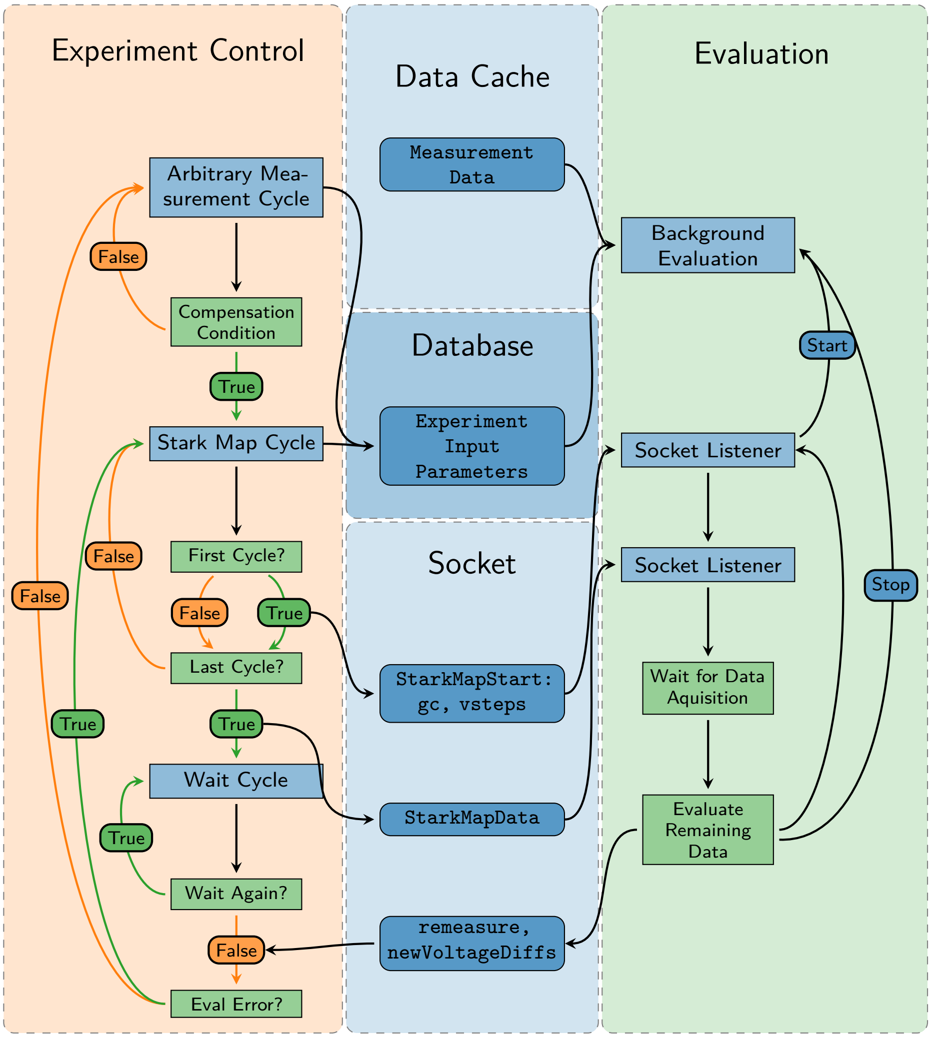

Figure A.2: Flow diagram of the automated Stark map setup. The experiment control software communicates with the evaluation computer directly over a network socket. All measurement parameters are stored in a MySQL database where they can be accessed from the evaluation routine. The measured data is stored in the data cache network drive. The background evaluation functions listens for changes in this data cache and evaluates new found data.

The evaluation program can be used with a `MATLAB` graphical user interface (GUI) that can also be used for manual evaluation of Stark maps, shown in Fig. A.3. The components are briefly described in the following list

1 The status bar shows the status of the automated routine.

2 In this area, information like the compensation values of the currently selected Stark map is shown.

3 In this panel, the already evaluated Stark maps are listed, sorted by their *global counter*. They can be selected by the user to show the corresponding plots in 5 and information in 2. Further, by clicking the "+" button, a Stark map can be manually evaluated. If a start

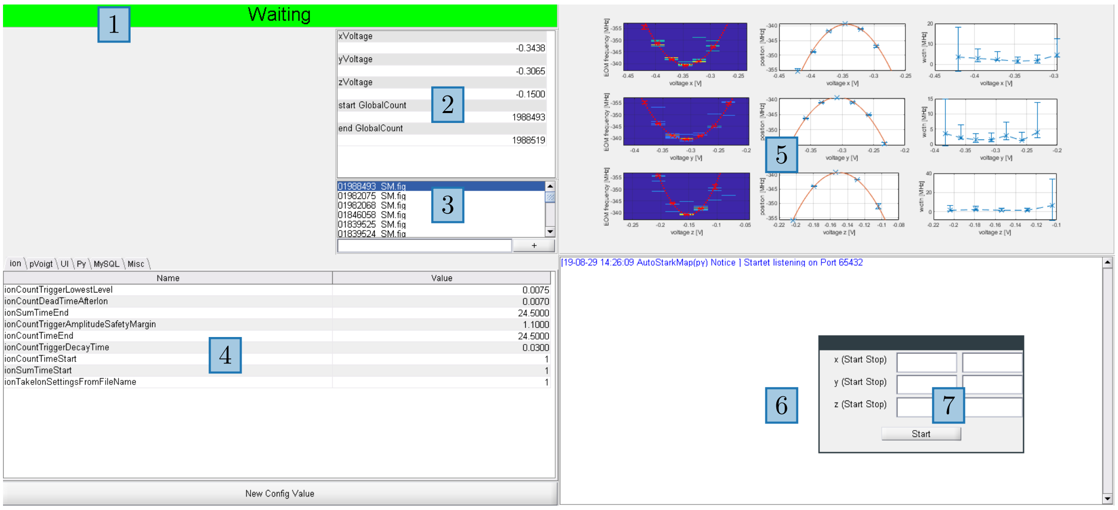

xVoltage -0.3438
yVoltage -0.3065
zVoltage -0.1500
start GlobalCount 1988493
end GlobalCount 1988519

01988493 SM.fig
01982075 SM.fig
01982068 SM.fig
01846058 SM.fig
01839525 SM.fig
01839524 SM.fig

Name	Value
ionCountTriggerLowestLevel	0.0075
ionCountDeadTimeAfterIon	0.0070
ionSumTimeEnd	24.5000
ionCountTriggerAmplitudeSafetyMargin	1.1000
ionCountTimeEnd	24.5000
ionCountTriggerDecayTime	0.0300
ionCountTimeStart	1
ionSumTimeStart	1
ionTakeIonSettingsFromFileName	1

```
[19-08-29 14:26:09 AutoStarkMap(py) Notice ] Startet listening on Port 65432
```

x (Start Stop)
y (Start Stop)
z (Start Stop)

Figure A.3: Screenshot of the `MATLAB` graphical user interface of the automatic Stark map evaluation software. The different numbered areas are described in the text.

global counter is given in the input box next to the "+" button, the program determines if a Stark map measurement is found at the given global counter and evaluates it. If no global counter is given, overlay 7 opens and the user can manually input the start and end global counters of the three spatial directions individually.

4 The software can be configured via this panel. The clearly structured index tabs and the ability to easily add configuration variables by using the button on the bottom of the panel gives the program a high flexibility. By clicking on the name of a configuration variable, a note on the usage of the variable can be displayed.

5 This panel shows the measured spectra, the fitted parabola and the line width of the individual Rydberg lines of the currently selected (3) Stark map measurement.

6 In this panel, debug notifications and errors are displayed.

The method used to compensate the electric fields has some limits, mostly given by limited automation of other experimental components. Those limits and how to overcome them are summarized in the following list.

- The target Rydberg state must be the same for the Stark map model as for the main model, since the change of state involves a change in laser frequency. This is not automated in the experiment and needs manual intervention.
- If the Stark shift caused by the stray field drifts is larger than the scan range, the transition line will be out of the measured area. However, this is extremely unlikely as this would require field drifts on the order of $10\,{}^{\mathrm{mV}}/_{\mathrm{cm}}$ which was not observed during regular operation. This weakness can be fixed by implementing a scan routine which would scan the frequency limits of the measured spectrum in the case of this event. However, this requires the use of more dynamic variables since only dynamic variables can be changed by the Python script. This adds to the complexity of the system and was therefore decided against.
- The routine needs a specifically designed experiment control model for both the main model and the Stark map model, which involves longer manual preparation time when creating measurement sequences.

- The evaluation program can at this point only be used for states with a purely quadratic Stark shift. By adding other fit functions, tailored to the occurring Stark shift, this can be easily extended.

B Field Reversing Box

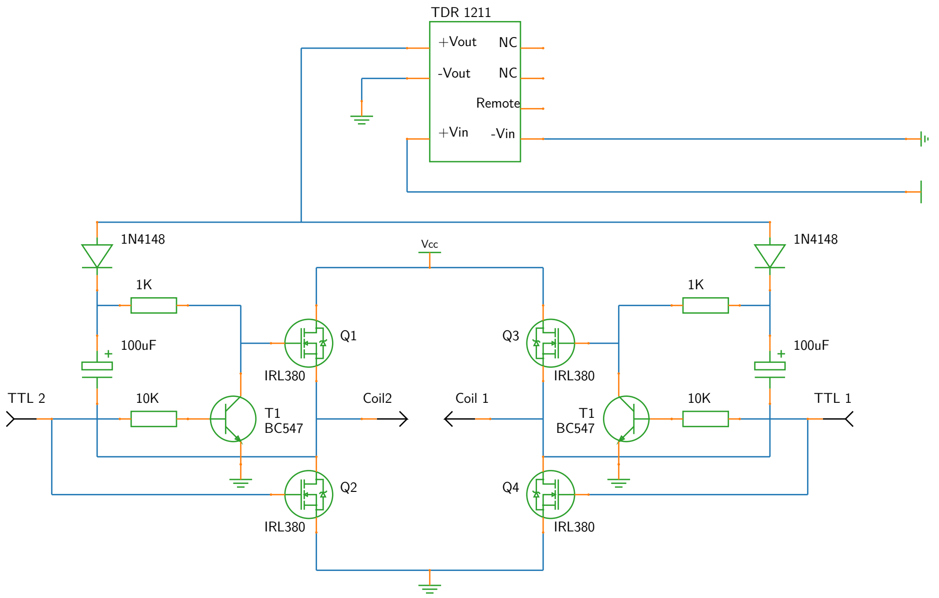

Figure B.4: Circuit diagram of the magnetic field direction switch circuit. A full bridge with `IRL 380` logic-level MOSFETs switched by two TTL signals governs the direction of the current through the coils. The high side MOSFETs are switched by a bootstrapping circuit. The supply voltage (5 V) for the bootstrapping is generated by a `TDR 1211` DC-DC converter.

In our setup, the magnetic field used in the optical dipole trap experiments is generated by offset coils which are supplied by a `EA-PS 3016-10B` unipolar constant current supply, controlled by an analog signal from the experiment control cards. The unipolarity of this supply inhibits that a magnetic field can be applied in both directions. This prevents the compensation of magnetic stray fields and a configuration with parallel magnetic and electric ionization field for state selective field ionization pointing in the same direction. Changing the polarity of the power supply is not an option since the offset field is used in the transfer sequence when loading atoms from the magnetic trap into the optical dipole trap. To circumvent this, a switching circuit was designed and implemented. The circuit consists of a full H-bridge with `IRL380` logic level MOSFETs. If transistor Q1 and Q4 are switched, the current flows through the coil in positive direction from connector `Coil 1` to `Coil 2`. In the opposite configuration, the current runs from `Coil 2` to `Coil 1`, reversing the applied magnetic field.

To switch the MOSFETs, a voltage of 3.3 V needs to be applied between the `source` and the `gate` of the MOSFET, since the voltage drops across the coils between the high-side MOSFETs (Q1, Q3) and the low-side MOSFETs (Q2,Q4). This causes the voltage between `source` and `gate` on the high-side MOSFETs to be smaller than 3.3 V when applying a TTL signal, which carries 3.3 V to ground. To address this problem a bootstrapping [72] configuration is used, which needs an external power supply. We use the same power supply which is used for the remaining coil control circuits [61]. To make sure that the ground of this supply is not connected to the ground of the coils and therefore with the other coil control circuits, a `TDR 1211` push-pull dc-dc converter is used. Note that the use of a bootstrapping circuit needs a regular cycling of the switching signal, since the capacitor looses charge over time due to leak currents and is only recharged during switching. The use of the high capacity of 100 μF makes it possible to switch them once per experiment cycle (ca. 30 s). A negative effect from the thereby introduced slower switching speed could not be observed in the experiment.

An advanced version of the apparatus with three channels for all three magnetic field coil pairs and minor improvements is currently under development.

C Clamp Switch

When using the ramped state selective field ionization scheme (Sec. 3.1.2), a voltage of up to 400 V needs to be applied to the field plates. However, before the ionization, during the Rydberg excitation and the circularization, a precise voltage for stray field compensation is needed. Of course, the amplifier used for the high voltage does also amplify the noise on the input signal of the amplifier generated by a `Keysight 33522B` AWG. This noise is incompatible with the requirements of the compensation field and therefore needs to be clamped out. This can be done by a clamp switch [53] circuit as can be seen in Fig. C.5. The output of the HV amplifier is connected to the output through diodes $D1$ to $D4$. If the voltage difference between the HV terminal and the output terminal is smaller than the forward voltage of the diodes, the diodes do not conduct and the output is isolated from the HV input terminal. The voltage at the output terminal is controlled by the voltage applied at the offset terminal. This means, that at the output terminal the offset voltage is applied and only if the difference between offset voltage and HV voltage rises above the forward voltage of the diodes, the HV voltage is switched to the output terminal. To allow a positive and negative HV input voltage, two pairs of diodes in opposite direction are used. The output voltage curve can be seen in Fig. C.6a for different offset voltages. The HV input voltage is ramped down and when it is close to the offset voltage, the switch closes and blocks the HV input. A plateau forms at the offset voltage.

The improvement of the noise on the offset signal can be seen in Fig. C.6b. The signal with the offset applied through the clamp switch shows noise which is a factor of ten smaller[1] compared to the signal with the offset directly applied to the signal before the amplification. It is not possible to use the clamp switch for low-noise ramping of the offset field for Stark switching, since the plateau around the offset is only a few hundred mV in HV input voltage (700 mV per diode). This means the HV input must be ramped in the same manner as the offset voltage to keep the switch

---

[1] 5 $\mathrm{mV_{rms}}$ compared to 60 $\mathrm{mV_{rms}}$ without the clamp switch.

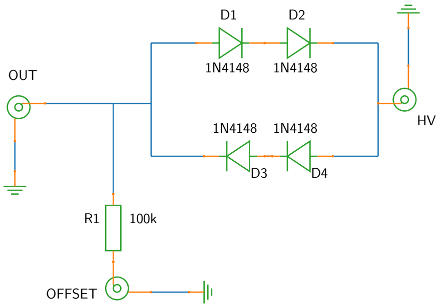

Figure C.5: Circuit diagram of the switch used to clamp out the noise of the HV-amplifier. If the voltage difference between the `HV` side and the `offset` side of the diodes is smaller than the forward voltage of the serial diodes, the `HV` side (and thereby its noise) is clamped out.

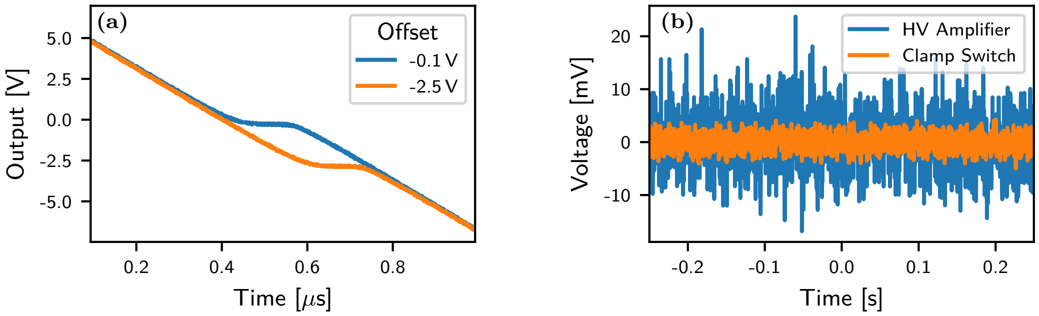

Figure C.6: **(a)** Output of the clamp switch for different offset voltages. The HV input voltage is ramped through. If the HV input voltage is close to the offset voltage, the switch closes and a plateau forms. **(b)** Output noise of the HV amplifier and the clamp switch in closed configuration. Both figures are measured with an DC offset voltage of $150\,\mathrm{V}$, applied directly at the amplifier and at the clamp switch offset terminal respectively.

closed. It is hard to synchronize these ramps due to delays and the finite voltage resolution of the HV signal of $12\,\mathrm{mV}$, caused by the voltage resolution of the AWG of $0.3\,\mathrm{mV}$ [36]. It would be possible to add more diodes in series to increase the plateau voltage, but this would also increase the non-linear areas close to the plateau.

D Characterization and Comment on the `Siglent SDG6022X` AWG

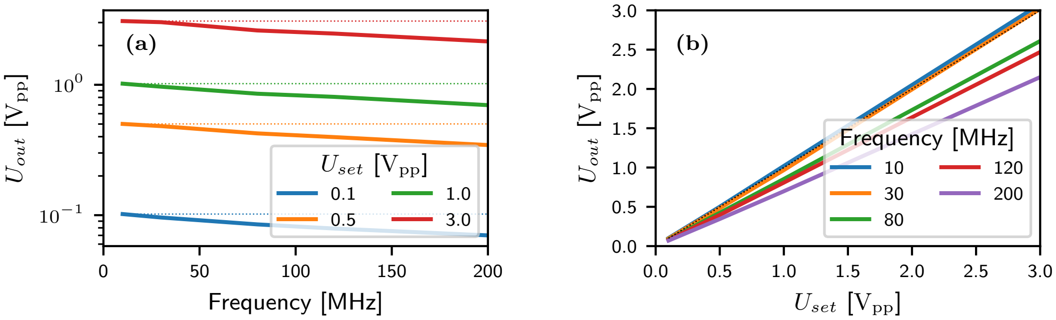

Figure D.7: **(a)** Frequency dependent voltage output of the `Siglent SDG6022X` AWG used for generating an RF field. For higher frequencies the output voltage deviates from the set voltage (dotted lines). **(b)** The relationship between set voltage U_{set} and the measured voltage U_{out} of the same AWG for different frequencies. Again the deviation between the two voltages is well visible for higher voltages. The dotted black line indicates $U_{out} = U_{set}$.

Voltage Output

As can be seen in Fig. D.7b and Fig. D.7a, the output peak-to-peak voltage of the AWG used for generating the RF field in the experiment differs strongly from the voltage set at the AWGs user interface for higher frequencies. The output voltage was measured with a `Agilent 34410A` multimeter. By fitting the obtained data, an approximation for the output peak-to-peak voltage is obtained

$$U_{out}(U_{set}, f) = \frac{U_{set}}{0.942774 + 0.00225678 f}. \tag{D.1}$$

Note that this formula is not universal to all `Siglent SDG6022X`, but specific to a certain device.

Issues with Programming

The `Siglent SDG6022X` offers a cheap device which can compete with much more expensive rival products in regard of features and specifications. However, the firmware of the device exhibits many flaws and bugs, which must be payed attention to specifically if the device is programmed by a remote interface. When sending arbitrary waveform binary data to the AWG, the AWG does not comply with the SCPI [10] standard. It does not account for the number of bytes specified by `#<length_of_byte_size><num_of_bytes>`. In a binary string, the code for "newline" (`0x0a`) can occur which is the command terminator in the SCPI standard. Since the AWG does not treat the data correctly, those newline characters are not escaped correctly and the command is terminated, leaving the rest of the binary data in the buffer of the AWG. Not only does this produce a wrong output but can also crash the device. In some cases, the device will not start up again but hangs in the boot screen. A firmware file to reset the device via an USB stick can be requested from the manufacturer. Note that the USB stick containing the file must be smaller than 4 GB.

Other issues come up when programming the device over a socket connection. The AWG does not close opened socket connections properly. The device crashes after opening connections to it 92 times. A solution is to program the device over a telnet connection where this problem is not present. However, it is not possible to send binary arbitrary wave form data via telnet. If arbitrary waveform data is required, a solution is to never close the existing socket connection, however, this would require an additional background process in our experiment.

E Magnetic Field Calibration

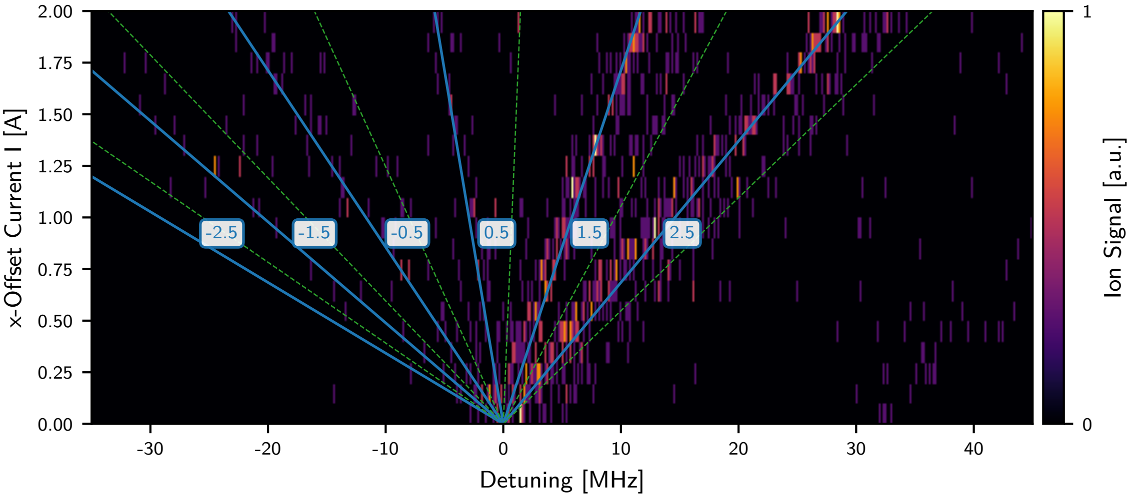

Figure E.8: From the Zeeman splitting of the magnetic sublevels of the $58D$ state, the conversion factor between the current applied to the x-offset coils I and the generated magnetic field B can be obtained. The blue lines are fits of Eq. (E.1) to the different m_j levels marked by the blue numbers. The green lines mark the transitions form the $5S_{1/2}, m_F = 1$ states.

The magnetic field B in x direction is controlled by applying a current I to the corresponding coil pair. To obtain a conversion factor between the current I and the generated magnetic field B, the Zeeman shift of the magnetic sublevels of the $58D$ state was measured (Fig. E.8). The Zeeman shift of this level can not be measured directly, since the initial state $5S_{1/2}$ of the Rydberg excitation also exhibits a finite Zeeman shift. Instead, the differential Zeeman shift of the initial and the target state

$$\Delta E_{\mathrm{Ze}} = (g_j m_j - g_F m_F)\mu_B B = (g_j m_j - g_F m_F)\mu_B \eta_B I \tag{E.1}$$

is measured. Where $g_F = 0.5$ is the Landé factor and $m_F = 2$ the magnetic moment of the initial $5S_{1/2}$ state. The Landé factor of the target $56D$ state is $g_j = 1.2$. By fitting Eq. E.1 to the measured magnetic sublevels m_j of Fig. E.8, the conversion factor $\eta_B = 5.306\,\mathrm{G/A}$ is obtained, giving the magnetic field

$$B = 5.306\mathrm{G/A}\, I. \tag{E.2}$$

F ARP Simulation Material

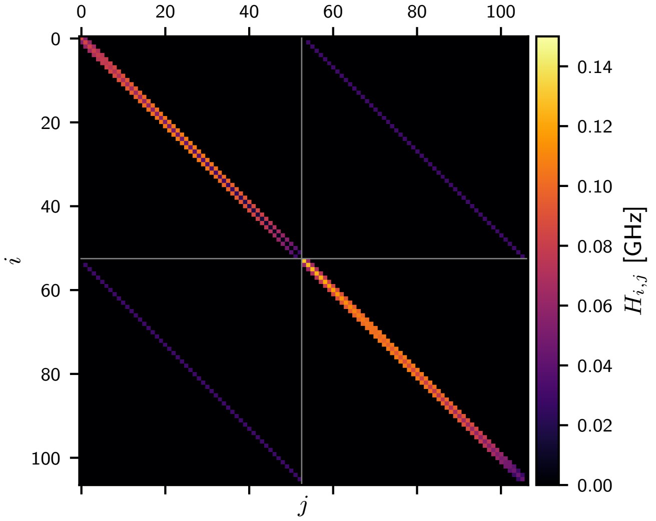

Figure F.9: Adiabatic rapid passage Hamiltonian (Eq. (4.29)) for $n = 56, f_{RF} = 200\,\mathrm{MHz}$ at an dc electric field of $E = 1.65\,\mathrm{V/cm}$ where the σ^+ transitions are almost on resonance. The upper left quadrant describes the $n_1 = 0$ states and their coupling by the σ^+ polarized RF field. The lower right quadrant describes the $n_1 = 1$ states and the σ^+ coupling between them. The σ^- coupling between the $n_1 = 0$ and the $n_1 = 1$ states is described by the upper right and the lower left quadrant. The state on the last element of the diagonal is the state which represents the states with $n_1 > 1$ in the open quantum system representation (cf. 4.3.2). The σ^+ and σ^- RF-field components are chosen to be equally strong at $E_{RF} = 0.1\,\mathrm{V/cm}$ to represent a typical experimental situation.

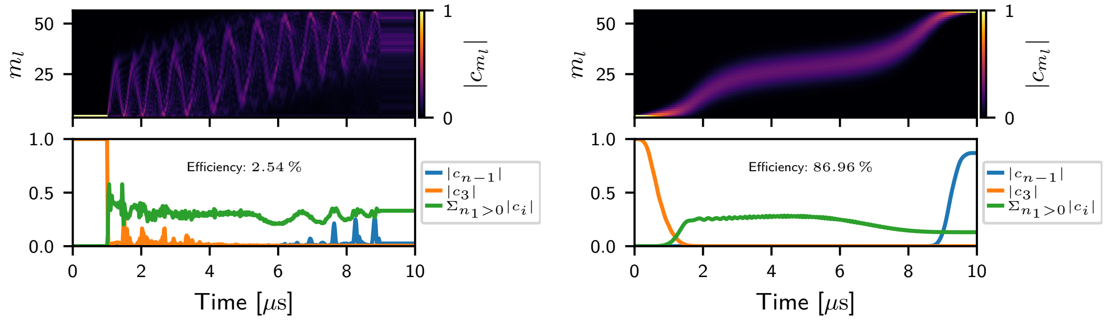

Figure F.10: **(a)** ARP simulation results for the same parameters as Fig. 18b but with a quenched RF field. If the RF field is not ramped up adiabatically, but switched on instantaneously at $t = 1\,\mu\text{s}$, the population is quenched to a multitude of states including the $n_1 = 1$ states and possibly states with $n_1 > 1$ if they were included in the simulation. The limited basis set in the model makes this simulation quantitatively unpredictive. **(b)** Simulation for the same parameters as Fig. 19b, but with $90\,\%$ reduced σ^- component $E_{\text{RF}} = 0.1\,\text{V/cm}$. The $n_1 > 0$ states are much less populated and the passage is still efficient. This shows that the decrease of efficiency when increasing the RF field strength E_{RF} is only governed by the σ^- component of the field. The efficiency shown in the plots represents the fraction of the occupation in the circular state c_{n-1} after the procedure.

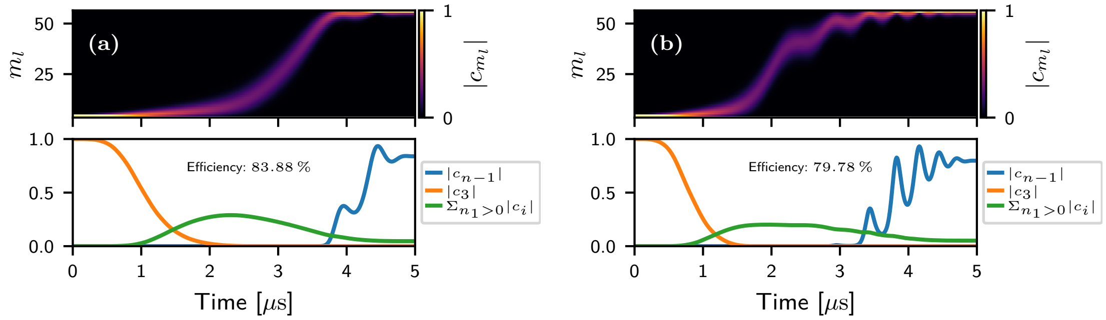

Figure F.11: ARP simulation results for $n = 56$, $E_0 = 1.85\,\text{V/cm}$, $E_1 = 1.4\,\text{V/cm}$, $B = 15\,\text{G}$ and $E_{RF} = 0.25\,\text{V/cm}$. For the calculations, it was assumed that the σ^- and the σ^+ component of the RF field are equally strong. By choosing the frequency smaller ($f_{RF} = 190\,\text{MHz}$) **(a)** or larger ($f_{RF} = 200\,\text{MHz}$) **(b)** than the optimum ($f_{RF}^{opt} = 195\,\text{MHz}$), the efficiency drops since the dressing field is effectively smaller at the crossing. The oscillations in the circular state occupation c_{n-1} are an indication that the crossing is not crossed fully adiabatically anymore.

G ARP `Python` Documentation

G.1 PythonSim.fields module

`fields.`**`DCRamp`**`(`*lengthTns*, *startVcm*, *endVcm*`)`

Function for generating the time dependent DC field

Generates an linear ramp with the length of *lengthTns*.

Parameters

- **`lengthTns`** (*`float`*) – Length of the ramp in ns
- **`startVcm`** (*`float`*) – Start electric field of the ramp in V/cm
- **`endVcm`** (*`float`*) – Final electric field of the ramp in V/cm

Returns Function which takes one argument (Time t in ns) and returns the DC at that moment of time.

Return type function

`fields.`**`RFPulse`**`(`*lengthTns*, *amplitudeVcm*`)`

Function for generating the time dependent RF field

Generates an RF pulse with a length of *lengthTns*, shaped like a cosine. This is the pulse used in the Experiment.

Parameters

- **`lengthTns`** (*`float`*) – Length of the pulse in ns
- **`amplitudeVcm`** (*`float`*) – Amplitude of the pulse (Value in the middle of the pulse) in V/cm.

Returns Function which takes one argument (Time t in ns) and returns the RF field amplitude at that moment of time.

Return type function

`fields.`**`RFQuench`**`(`*lengthTns*, *amplitudeVcm*`)`

Function for generating the time dependent RF field

Generates an RF pulse with the length of *lengthTns*. The field is instantly turned on at *0.1*lengthTns* and turned of at *0.9*lengthTns*.

Parameters

- **`lengthTns`** (*`float`*) – Length of the pulse in ns
- **`amplitudeVcm`** (*`float`*) – Amplitude of the pulse in V/cm.

Returns Function which takes one argument (Time t in ns) and returns the RF field amplitude at that moment of time.

Return type function

G.2 PythonSim.main module

`class main.`**`Simulation`**`(`*atomicHamiltonian*, *dipoleMoments*, *transitions*, *n*, *maxN1*, *startState*, *rfField*, *rfFreqGHz*, *dcField*, *zeroEnergy*, *lossFactor*`)`

Bases: `object`

Main class for the simulation.

`size`

int – size of the Hamiltonian after removing far away states.

`lastHamiltonian`

numpy Array – contains the Hamiltonian calculated by the last call of the *calcHamiltonian()* method.

`lastT`

float – Time for which the Hamiltonian stored in *lastHamiltonian* was calculated

`calcHamiltonian`(*t*)

Calculates the Hamiltonian

Stores the result in *lastHamiltonian.* If called for the first time, the collapse operators are calculated and stored in *collapse.*

Note: If the function is called consecutive times for the same time step, the Hamiltonian is not calculated anew, but the result stored in *lastHamiltonian* is returned.

Parameters `t` (*`float`*) – timestep at which to calculate the Hamiltonian

Returns Hamiltonian matrix

Return type numpy Array

`calculate`(*t*, **args*)

Wrapper function for *calcHamiltonian* for the use with *Qutip.mesolve()* that returns the Hamiltonian as a *qutip.Qobj* instead of a numpy array.

`collapsCoeffs`(*t*, **args*)

Returns the time dependent collapse coefficients for the Lindbad Master equation.

Calculates the collapse coefficient as the product of the current RF field and the specified *lossFactor*

Parameters `t` (*`float`*) – Time at which the coefficient should be calculated

Returns collapse coefficient

Return type float

`plotDetunings`(*rampTime*)

Plots the detunings during the simulation time for visualization purposes

Parameters **`rampTime`** (*`float`*) – Length of the ARP process.

`plotEigenvalues`(*rampTime*, *timesteps=100*)

Plots the eigenvalues of the system Hamiltonian during the simulation time

Parameters

- **`rampTime`** (*`float`*) – Length of the ARP process.
- **`timesteps`** (*`int`*) – Number of time steps at which to calculate the eigenvalues

Returns Array of the eigenvalues at the specified times

Return type numpy array

`plotHamiltonian`(*t*)

Plots the system Hamiltonian as a matrix plot.

Parameters `t` (*`float`*) – Moment of time at which to calculate the Hamiltonian.

Returns Hamiltonian at the specified moment of time.

Return type numpy array

`main.`**`readInputData`**`(`*foldername*, *fileprefix*`)`

Helper function for reading input data csv files.

The input files for the simulations are supplied as csv files. For each m_l a csv file needs to be supplied for the Hamiltonian ('Hamiltonian_##.csv'), a csv file containing the transition elements ('Trans_##.csv') and a csv file containing the dipole moments of the states ('Dipole_##.csv'). Also, the energy where to set the zero energy point is supplied as a single value in a csv file 'EnergyZero.csv'. This function reads all numbered files with the given 'fileprefix' in the folder 'foldername' and returns their content as a list of numpy arrays.

Parameters

- **`foldername`** (*str*) – Name of the folder to read .csv files from
- **`fileprefix`** (*str*) – Fileprefix of the csv. files to import

Returns list of numpy arrays, containing the imported data.

Return type list

Bibliography

[1] D. A. Anderson et al. “Production and trapping of cold circular Rydberg atoms”. In: *Phys. Rev. A* 88 (3 Sept. 2013), p. 031401. DOI: 10.1103/PhysRevA.88.031401. URL: https://link.aps.org/doi/10.1103/PhysRevA.88.031401.

[2] M. Archimi et al. “Measurements of single-state and state-ensemble lifetimes of high-lying Rb Rydberg levels”. In: *Physical Review A* 100.3 (Sept. 2019). DOI: 10.1103/physreva.100.030501.

[3] D. Barredo et al. “Synthetic three-dimensional atomic structures assembled atom by atom”. In: *Nature* 561.7721 (Sept. 2018), pp. 79–82. DOI: 10.1038/s41586-018-0450-2.

[4] S. Blanes et al. “The Magnus expansion and some of its applications”. In: *Physics Reports* 470.5-6 (Jan. 2009), pp. 151–238. DOI: 10.1016/j.physrep.2008.11.001.

[5] R. Brecha et al. “Circular Rydberg states with very large n”. In: *Optics Communications* 102.3-4 (Oct. 1993), pp. 257–264. DOI: 10.1016/0030-4018(93)90392-i.

[6] D. M. Brink and C. V. Sukumar. “Majorana spin-flip transitions in a magnetic trap”. In: *Physical Review A* 74.3 (Sept. 2006). DOI: 10.1103/physreva.74.035401.

[7] R. Cardman and G. Raithel. “Circularizing Rydberg atoms with time-dependent optical traps”. In: (Sept. 14, 2019). arXiv: 1909.06612v1 [physics.atom-ph].

[8] S. Chaudhuri et al. “Rate of field ionization fromSstates with a quantum defect”. In: *Physical Review A* 23.4 (Apr. 1981), pp. 1657–1661. DOI: 10.1103/physreva.23.1657.

[9] C. H. Cheng, C. Y. Lee, and T. F. Gallagher. “Production of Circular Rydberg States with Circularly Polarized Microwave Fields”. In: *Physical Review Letters* 73.23 (Dec. 1994), pp. 3078–3081. DOI: 10.1103/physrevlett.73.3078.

[10] S. Consortium. *Standard Commands for Programmable Instruments*. 1999.

[11] W. E. Cooke and T. F. Gallagher. “Effects of blackbody radiation on highly excited atoms”. In: *Physical Review A* 21.2 (Feb. 1980), pp. 588–593. DOI: 10.1103/physreva.21.588.

[12] R. J. Damburg and V. V. Kolosov. “A hydrogen atom in a uniform electric field. III”. In: *Journal of Physics B: Atomic and Molecular Physics* 12.16 (Aug. 1979), pp. 2637–2643. DOI: 10.1088/0022-3700/12/16/011.

[13] D. Delande and J. C. Gay. “A New Method for Producing Circular Rydberg States”. In: *Europhysics Letters (EPL)* 5.4 (Feb. 1988), pp. 303–308. DOI: 10.1209/0295-5075/5/4/004.

[14] E. K. Dietsche et al. “High-sensitivity magnetometry with a single atom in a superposition of two circular Rydberg states”. In: *Nature Physics* 15.4 (Jan. 2019), pp. 326–329. DOI: 10.1038/s41567-018-0405-4.

[15] C. S. E. van Ditzhuijzen, A. Tauschinsky, and H. B. van Linden van den Heuvell. “Observation of Stückelberg oscillations in dipole-dipole interactions”. In: *Physical Review A* 80.6 (Dec. 2009). DOI: `10.1103/physreva.80.063407`.

[16] F. B. Dunning et al. “Engineering atomic Rydberg states with pulsed electric fields”. In: *Journal of Physics B: Atomic, Molecular and Optical Physics* 42.2 (Jan. 2009), p. 022001. DOI: `10.1088/0953-4075/42/2/022001`.

[17] F. Engel et al. “Observation of Rydberg Blockade Induced by a Single Ion”. In: *Physical Review Letters* 121.19 (Nov. 2018). DOI: `10.1103/physrevlett.121.193401`.

[18] T. Esslinger, I. Bloch, and T. W. Hänsch. “Bose-Einstein condensation in a quadrupole-Ioffe-configuration trap”. In: *Physical Review A* 58.4 (Oct. 1998), R2664–R2667. DOI: `10.1103/physreva.58.r2664`.

[19] A. Facon et al. “A sensitive electrometer based on a Rydberg atom in a Schrödinger-cat state”. In: *Nature* 535.7611 (July 2016), pp. 262–265. DOI: `10.1038/nature18327`.

[20] T. L. Floyd. *Principles of Electric Circuits*. Prentice Hall College Div, 1996. ISBN: 0-13-232224-2. URL: `https://www.amazon.com/Principles-Electric-Circuits-Thomas-Floyd/dp/0132322242?SubscriptionId=AKIAIOBINVZYXZQZ2U3A&tag=chimbori05-20&linkCode=xm2&camp=2025&creative=165953&creativeASIN=0132322242`.

[21] C. J. Foot. *Atomic Physics*. Oxford University Press, Nov. 25, 2004. 344 pp. ISBN: 0198506961. URL: `https://www.ebook.de/de/product/3611193/c_j_department_of_physics_university_of_oxford_foot_atomic_physics.html`.

[22] K. Fujii et al. “N Level System with RWA and Analytical Solutions Revisited”. In: (July 9, 2003). arXiv: `http://arxiv.org/abs/quant-ph/0307066v2 [quant-ph]`.

[23] T. F. Gallagher. *Rydberg Atoms*. Cambridge University Press, Aug. 25, 2005. 512 pp. ISBN: 0521021669. URL: `https://www.ebook.de/de/product/5136455/thomas_f_gallagher_rydberg_atoms.html`.

[24] R. Grimm, M. Weidemüller, and Y. B. Ovchinnikov. “Optical dipole traps for neutral atoms”. In: *Advances in Atomic, Molecular and Optical Physics Vol. 42, 95-170 (2000)* (Feb. 24, 1999). arXiv: `http://arxiv.org/abs/physics/9902072v1 [physics.atom-ph]`.

[25] M. Gross et al. “Precision RF Spectroscopy of Circular Rydberg Atoms”. In: *The Hydrogen Atom*. Springer Berlin Heidelberg, 1989, pp. 134–142. DOI: `10.1007/978-3-642-88421-4_13`.

[26] Hamamatsu. *PHOTOMULTIPLIER TUBES Basics and Applications*. 2019.

[27] S. Hammer. “Setting up a lightsheet for realizing quasi two-dimensional quantum gases”. BSC. 5. Physikalisches Institut, Universität Stuttgart, 2017.

[28] J. Han et al. “Rbnfquantum defects from millimeter-wave spectroscopy of coldRb85Rydberg atoms”. In: *Physical Review A* 74.5 (Nov. 2006). DOI: `10.1103/physreva.74.054502`.

[29] J. Hare, M. Gross, and P. Goy. “Circular Atoms Prepared by a New Method of Crossed Electric and Magnetic Fields”. In: *Physical Review Letters* 61.17 (Oct. 1988), pp. 1938–1941. DOI: `10.1103/physrevlett.61.1938`.

[30] F. P. Heinz-Peter Breuer. *The Theory of Open Quantum Systems*. Oxford University Press, Feb. 1, 2007. ISBN: 0199213909. URL: `https://www.ebook.de/de/product/6212122/heinz_peter_breuer_francesco_petruccione_the_theory_of_open_quantum_systems.html`.

[31] U. Hermann. “Analysing and improving high resolution Rydberg field ionization statistics”. MSc. 2015.

[32] R. G. Hulet and D. Kleppner. “Rydberg Atoms in "Circular" States”. In: *Physical Review Letters* 51.16 (Oct. 1983), pp. 1430–1433. DOI: `10.1103/physrevlett.51.1430`.

[33] M. D. J. James R. Baker-Jarvis and B. F. Riddle. *Measuring the Permittivity and Permeability of Lossy Materials: Solids, Liquids, Metals, and negative-Index Materials*. Tech. rep. Technical Note (NIST TN) - 1536, 2005.

[34] J. Johansson, P. Nation, and F. Nori. “QuTiP 2: A Python framework for the dynamics of open quantum systems”. In: *Computer Physics Communications* 184.4 (Apr. 2013), pp. 1234–1240. DOI: `10.1016/j.cpc.2012.11.019`.

[35] P. Jurcevic et al. “Quasiparticle engineering and entanglement propagation in a quantum many-body system”. In: *Nature* 511.7508 (July 2014), pp. 202–205. DOI: `10.1038/nature13461`.

[36] KeysightTechnologies. *Trueform Series Waveform/Function Generators 33500B*. 2019.

[37] K. S. Kleinbach. “Ions and electrons interacting with ultracold atoms : novel approaches based on Rydberg excitations”. en. PhD thesis. 2018. DOI: `10.18419/opus-10042`.

[38] M. Kuna and J. Naudts. “Solving the von Neumann equation with time-dependent Hamiltonian. Part I: Method”. In: (May 29, 2008). arXiv: `http://arxiv.org/abs/0805.4487v1 [math-ph]`.

[39] W. Li et al. “Millimeter-wave spectroscopy of cold Rb Rydberg atoms in a magneto-optical trap: Quantum defects of thens,np, andndseries”. In: *Physical Review A* 67.5 (May 2003). DOI: `10.1103/physreva.67.052502`.

[40] J. Liang et al. “Circular Rydberg-state spectroscopy”. In: *Physical Review A* 33.6 (June 1986), pp. 4437–4439. DOI: `10.1103/physreva.33.4437`.

[41] S. T. C. LTD. *SDG6000X Series Pulse/Arbitrary Waveform Generator*. 2019.

[42] R. Lutwak et al. “Circular states of atomic hydrogen”. In: *Physical Review A* 56.2 (Aug. 1997), pp. 1443–1452. DOI: `10.1103/physreva.56.1443`.

[43] M. F. M. D. Lukin and P. Zoller. “Dipole Blockade and Quantum Information Processing in Mesoscopic Atomic Ensembles”. In: *Physical Review Letters* 87.3 (June 2001). DOI: `10.1103/physrevlett.87.037901`.

[44] E. Majorana. “Atomi orientati in campo magnetico variabile”. In: *Il Nuovo Cimento* 9.2 (Feb. 1932), pp. 43–50. DOI: `10.1007/bf02960953`.

[45] B. Minnis. “Decade Bandwidth Bias T’s for MIC Applications up to 50 GHz (Short Paper)”. In: *IEEE Transactions on Microwave Theory and Techniques* 35.6 (June 1987), pp. 597–600. DOI: `10.1109/tmtt.1987.1133711`.

[46] W. A. Molander, C. R. Stroud, and J. A. Yeazell. “Excitation of high angular momentum Rydberg states”. In: *Journal of Physics B: Atomic and Molecular Physics* 19.12 (June 1986), pp. L461–L465. DOI: `10.1088/0022-3700/19/12/003`.

[47] C. Moler and C. V. Loan. “Nineteen Dubious Ways to Compute the Exponential of a Matrix, Twenty-Five Years Later”. In: *SIAM Review* 45.1 (Jan. 2003), pp. 3–49. DOI: `10.1137/s00361445024180`.

[48] T. Nguyen et al. “Towards Quantum Simulation with Circular Rydberg Atoms”. In: *Physical Review X* 8.1 (Feb. 2018). DOI: `10.1103/physrevx.8.011032`.

[49] P. Nussenzveig et al. “Preparation of high-principal-quantum-number “circular” states of rubidium”. In: *Physical Review A* 48.5 (Nov. 1993), pp. 3991–3994. DOI: `10.1103/physreva.48.3991`.

[50] M. S. O'Sullivan and B. P. Stoicheff. "Scalar polarizabilities and avoided crossings of high Rydberg states in Rb". In: *Physical Review A* 31.4 (Apr. 1985), pp. 2718–2720. DOI: 10.1103/physreva.31.2718.

[51] S. Patsch et al. "Fast and accurate circularization of a Rydberg atom". In: *Physical Review A* 97.5 (May 2018). DOI: 10.1103/physreva.97.053418.

[52] E. L. Raab et al. "Trapping of Neutral Sodium Atoms with Radiation Pressure". In: *Physical Review Letters* 59.23 (Dec. 1987), pp. 2631–2634. DOI: 10.1103/physrevlett.59.2631.

[53] G. Raithel. *private communication*. private communication.

[54] A. Ramos, K. Moore, and G. Raithel. "Measuring the Rydberg constant using circular Rydberg atoms in an intensity-modulated optical lattice". In: *Physical Review A* 96.3 (Sept. 2017). DOI: 10.1103/physreva.96.032513.

[55] D. J. Reilly. "Engineering the quantum-classical interface of solid-state qubits". In: *npj Quantum Information* 1.1 (Oct. 2015). DOI: 10.1038/npjqi.2015.11.

[56] A. Reinhard et al. "Rydberg-Rydberg Collisions: Resonant Enhancement of State Mixing and Penning Ionization". In: *Physical Review Letters* 100.12 (Mar. 2008). DOI: 10.1103/physrevlett.100.123007.

[57] M. Rockenhäuser. "Microwave setup for spectroscopy of ultracold Rydberg atoms". MSC. 5. Physikalisches Institut, Universität Stuttgart, 2019.

[58] J. D. Rodrigues, L. G. Marcassa, and J. T. Mendonça. "Excitation of high orbital angular momentum Rydberg states with Laguerre–Gauss beams". In: *Journal of Physics B: Atomic, Molecular and Optical Physics* 49.7 (Mar. 2016), p. 074007. DOI: 10.1088/0953-4075/49/7/074007.

[59] J. Rydberg. *Recherches sur la constitution des spectres d'émission des éléments chimiques*. franska. Vol. Band 23 No 11. Kungliga vetenskapsakademiens handlingar 11. Kungliga Vetenskapsakademien, 1890.

[60] M. Saffman, T. G. Walker, and K. Mølmer. "Quantum information with Rydberg atoms". In: *Reviews of Modern Physics* 82.3 (Aug. 2010), pp. 2313–2363. DOI: 10.1103/revmodphys.82.2313.

[61] M. Schlagmüller. "A single Rydberg Atom interacting with a Dense and Ultracold Gas". PhD thesis. 2016. ISBN: 978-3-8439-2783-3.

[62] M. Schlagmüller et al. "Ultracold chemical reactions of a single Rydberg atom in a dense gas". In: *Phys. Rev. X 6, 031020 (2016)* (May 16, 2016). DOI: 10.1103/PhysRevX.6.031020. arXiv: 1605.04883v3 [physics.atom-ph].

[63] T. Schmid. "High precision excitation manipulation and detection of Rydberg atoms". MSC. 5. Physikalisches Institut, Universität Stuttgart, 2013.

[64] D. Schönleber et al. "Quantum Simulation of Energy Transport with Embedded Rydberg Aggregates". In: *Physical Review Letters* 114.12 (Mar. 2015). DOI: 10.1103/physrevlett.114.123005.

[65] I. (Scientific Instrument Services. *SIMION 3D Ion and Electron Optics Simulation Suite*. 2003.

[66] A. Signoles et al. "Coherent Transfer between Low-Angular-Momentum and Circular Rydberg States". In: *Physical Review Letters* 118.25 (June 2017). DOI: 10.1103/physrevlett.118.253603.

[67] E. Standard. "EN 300 744 V1.5.1, Digital Video Broadcasting (DVB)".

[68] D. Steck. “Rubidium 87 D Line Data”. In: (Jan. 2003).

[69] S. Svanberg. *Atomic and Molecular Spectroscopy: Basic Aspects and Practical Applications (Advanced Texts in Physics)*. Springer, 2012. ISBN: 978-3-642-18520-5. URL: `https://www.amazon.com/Atomic-Molecular-Spectroscopy-Practical-Applications-ebook/dp/B000VYLM48?SubscriptionId=AKIAIOBINVZYXZQZ2U3A&tag=chimbori05-20&linkCode=xm2&camp=2025&creative=165953&creativeASIN=B000VYLM48`.

[70] E. Thébault et al. “International Geomagnetic Reference Field: the 12th generation”. In: *Earth, Planets and Space* 67.1 (May 2015). DOI: `10.1186/s40623-015-0228-9`.

[71] C. Tresp. “A Setup for Highly Precise Excitation and Detection of Rydberg Atoms”. MSC. 5. Physikalisches Institut, Universität Stuttgart, 2012.

[72] J. P. Uyemura. *CMOS Logic Circuit Design*. Springer US, Feb. 28, 1999. 552 pp. ISBN: 0792384520. URL: `https://www.ebook.de/de/product/3805391/john_p_uyemura_cmos_logic_circuit_design.html`.

[73] A. Walz-Flannigan. “l-changing collisions in cold Rydberg gases”. In: (Jan. 2002).

[74] H. Weimer et al. “Digital quantum simulation with Rydberg atoms”. In: *Quantum Information Processing* 10.6 (Sept. 2011), pp. 885–906. DOI: `10.1007/s11128-011-0303-5`.

[75] T. Wilk et al. “Entanglement of Two Individual Neutral Atoms Using Rydberg Blockade”. In: *Physical Review Letters* 104.1 (Jan. 2010). DOI: `10.1103/physrevlett.104.010502`.

[76] J. L. Wiza. “Microchannel plate detectors”. In: *Nuclear Instruments and Methods* 162.1-3 (June 1979), pp. 587–601. DOI: `10.1016/0029-554x(79)90734-1`.

[77] S. Yoshida et al. “Analysis of circular wave packets generated by pulsed electric fields”. In: *Nuclear Instruments and Methods in Physics Research Section B: Beam Interactions with Materials and Atoms* 279 (May 2012), pp. 4–7. DOI: `10.1016/j.nimb.2011.10.054`.

[78] S. Yoshida et al. “Rydberg blockade in a hot atomic beam”. In: *Physical Review A* 95.4 (Apr. 2017). DOI: `10.1103/physreva.95.042705`.

[79] C. Zener. “Non-Adiabatic Crossing of Energy Levels”. In: *Proceedings of the Royal Society A: Mathematical, Physical and Engineering Sciences* 137.833 (Sept. 1932), pp. 696–702. DOI: `10.1098/rspa.1932.0165`.

[80] Y. Zhang et al. “Measurement of atomic polarizabilities using Floquet spectroscopy”. In: *Physical Review A* 50.2 (Aug. 1994), pp. 1101–1106. DOI: `10.1103/physreva.50.1101`.

[81] V. Zhelyazkova and S. D. Hogan. “Preparation of circular Rydberg states in helium using the crossed fields method”. In: *Phys. Rev. A 94, 023415 (2016)* (Nov. 4, 2016). DOI: `10.1103/PhysRevA.94.023415`. arXiv: `http://arxiv.org/abs/1611.01308v1 [physics.atom-ph]`.